University of Stavanger

Faculty of Science and Technology

MASTER'S THESIS

Study program/Specialization:	Spring semester, 2021
Petroleum Geosciences Engineering	Open

Writer: Marte Aksland	.………………………………………… (Writer's signature)

Faculty supervisor: Nestor Cardozo, University of Stavanger External supervisor: Lothar Schulte, Schlumberger SIS

Thesis title: Geometrical and kinematical analysis of an extensional fault-propagation fold in the Wisting Field, Norwegian Barents Sea

Credits (ECTS): 30

Key words: Hoop Fault Complex Bjarmeland Platform Wisting Field Fault-Propagation Fold Monocline Curvature Analysis Trishear Modelling	Pages: 80 Stavanger, June 15th 2021

GEOMETRICAL AND KINEMATICAL ANALYSIS OF AN EXTENSIONAL FAULT-PROPAGATION FOLD IN THE WISTING FIELD, NORWEGIAN BARENTS SEA

By Marte Aksland

MCs Thesis

Faculty of Science and Technology

The University of Stavanger

THE UNIVERSITY OF STAVANGER

JUNE 2021

Acknowledgements

Geometrical and kinematical analysis of an extensional fault-propagation fold in the Wisting Field, Norwegian Barents Sea

Marte Aksland

The University of Stavanger, 2021

Supervisors: Nestor Cardozo, Lothar Schulte

Abstract

The Wisting field is located on the Bjarmeland Platform northeast of the Maud Basin and adjacent to the Hoop Fault Complex. It is Norway's northernmost oilfield to be developed. 3D high resolution P-Cable seismic data from the field display shallow (< 200 m below the seabed) monoclines in Upper Jurassic – Lower Cretaceous strata above normal faults, while the Upper Triassic – Middle Jurassic strata are faulted. These monoclines are extensional fault-propagation folds. This thesis analyzes one of these monoclines along a NNE-SSW fault. The purpose of the study is to characterize geometrically the monocline. In addition, trishear modelling is performed on four sections across the monocline, to reconstruct fold growth, strain, and potential minor structures. The interpreted Upper Triassic to Lower Cretaceous horizons (intra-Fruholmen to top Kolje formations) are pre-tectonic successions. The main tectonic event in this area was in the Early Cretaceous (Aptian–Albian), during the deposition of the Kolmule Formation. Fault throw is greatest towards the NE (~60 m) where the fault breaches the monocline. Towards the SW, the throw decreases and it is transferred to another fault in a relay structure. Bedding data and curvature analysis show that the monocline approaches a cylindrical shape. Trishear modeling indicates that the fault propagated from the Upper Triassic to the Upper Jurassic successions along most of its length. However, in the northernmost section, the fault propagated from the Middle Jurassic to the Lower Cretaceous successions. The predicted fault slip is consistent with the interpretation, but the predicted fault propagation to slip (P/S) decreases from south (P/S = 2.8) to north (P/S = 2.2). Areas on the forelimb of the monocline subject to higher strain magnitudes and potential high-angle fractures could be prone to fluids migrating to the surface. The evolution of the monocline is related to the mechanical stratigraphy; the folded upper strata mainly consist of shale and are ductile, while the lower faulted strata mainly consist of sandstones and are brittle.

Contents

List of tables

Lis of figures

1   Introduction

The western Barents Sea has experienced a complex geological evolution, which today is represented by several sedimentary basins, structural highs, fault complexes and widespread platform areas (Doré, 1995; Henriksen et al., 2011b). The Wisting field is in the Norwegian Barents Sea on the Bjarmeland Platform northeast of the Maud Basin and adjacent to the Hoop Fault Complex (Figure 1A, B & C). The area has experienced Neogene uplift and erosion of ~1.3-1.7 km (depending on the estimation methods used) of Cretaceous and Cenozoic sediments (Gabrielsen et al., 1990; Granli et al., 2017; Lasabuda et al., 2021). The Wisting field is an oil discovery, and the main reservoirs are in Upper Triassic to Middle Jurassic sandstones of the Realgrunnen Subgroup (Stueland, 2016). These reservoirs are today at very shallow depth, less than 500 m below the seabed, and they are highly compartmentalized by faults (Paulsen et al., 2019).
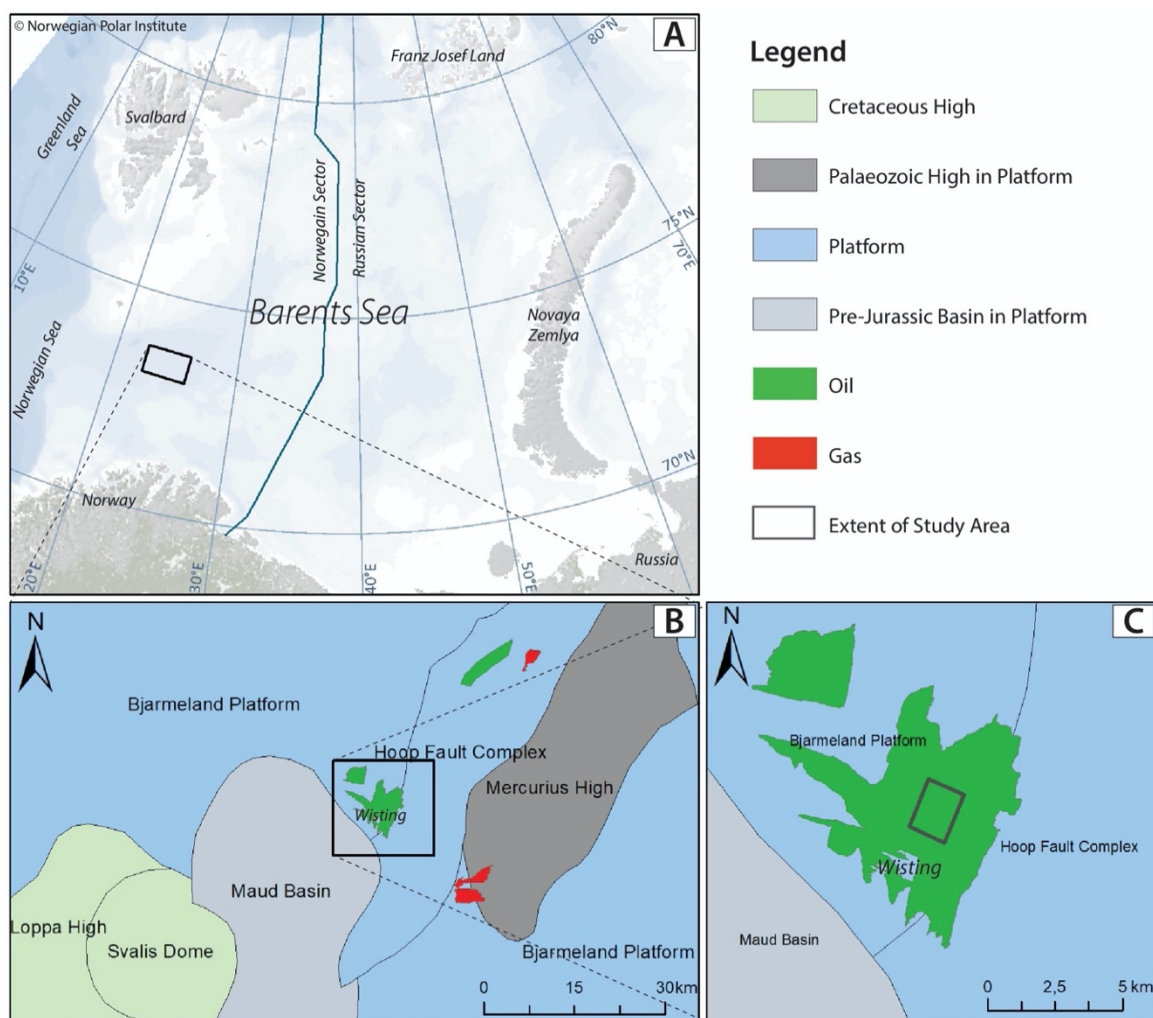
Figure 1: *Location map of (A) the Barents Sea, (B) the Wisting Field, and (C) the study area. (A) WMS from Norwegian Polar Institute (2020), (B) and (C) from NPD Factmaps (NPD, 2021)*

The Wisting field is affected by an orthorhombic fault system consisting of NNE–SSW and WNW–ESE trending faults (Figure 2; Kjølhamar, 2015; Collanega et al., 2017). These faults offset the Triassic-Jurassic succession and terminate upwards in the overlying Cretaceous succession, which is folded and form "flexures" or monoclines (Figure 3). The subject of study in this thesis is one of these monoclines above a NNE-SSW trending normal fault (Figure 2 and 3).
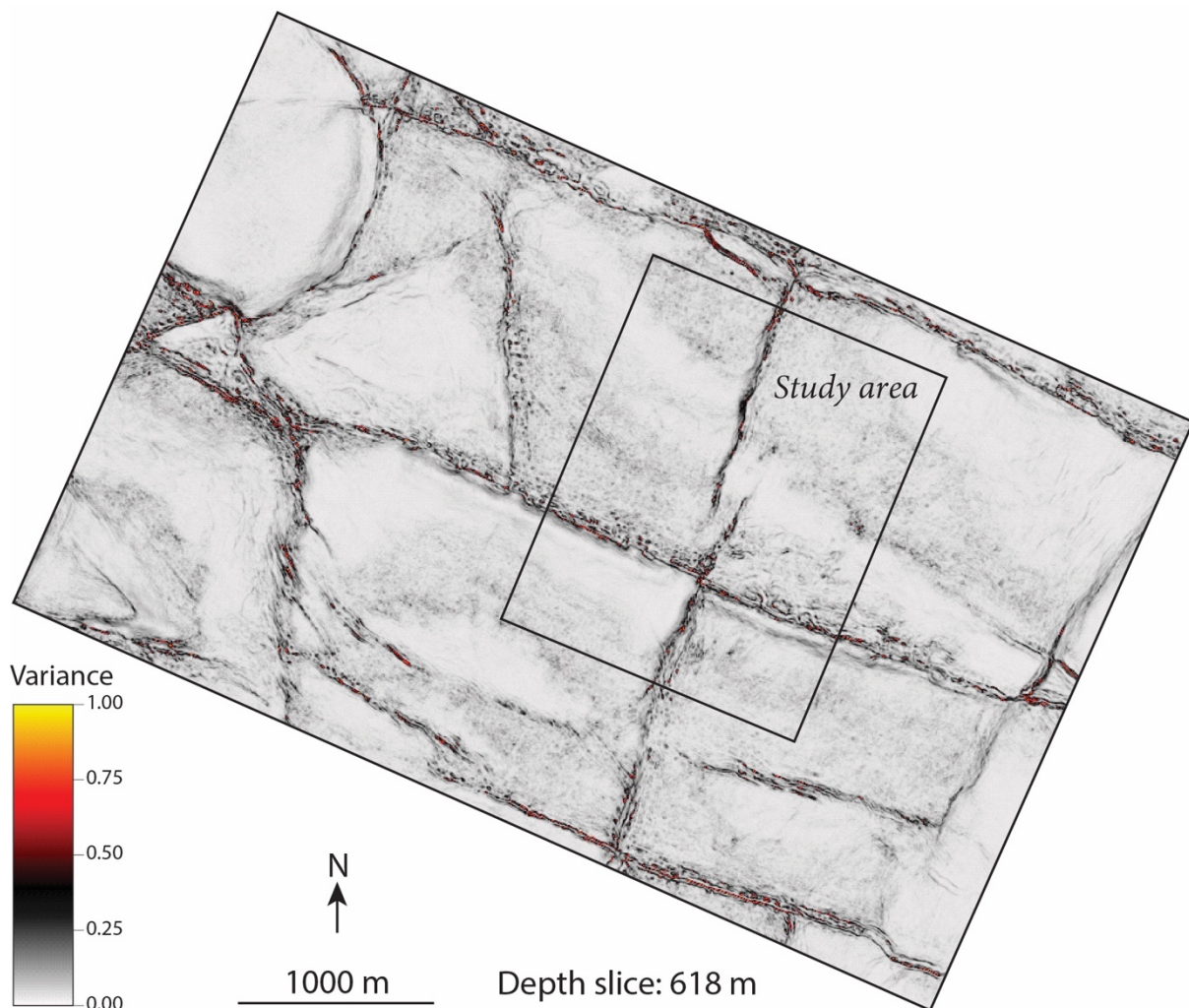
Figure 2: Variance depth slice displaying the orthorhombic fault system in the Wisting field

The monoclines in the Wisting area are extensional fault-propagation folds, where normal displacement along the underlying fault transitions upwards into a fold in the overlying sediments (Coleman et al., 2019). These folds are often developed in thick shale deposits overlying the propagating fault (Lewis et al., 2015). The incompetent rocks inhibit fault propagation and accommodate fault displacement by folding (Ferrill et al., 2012).
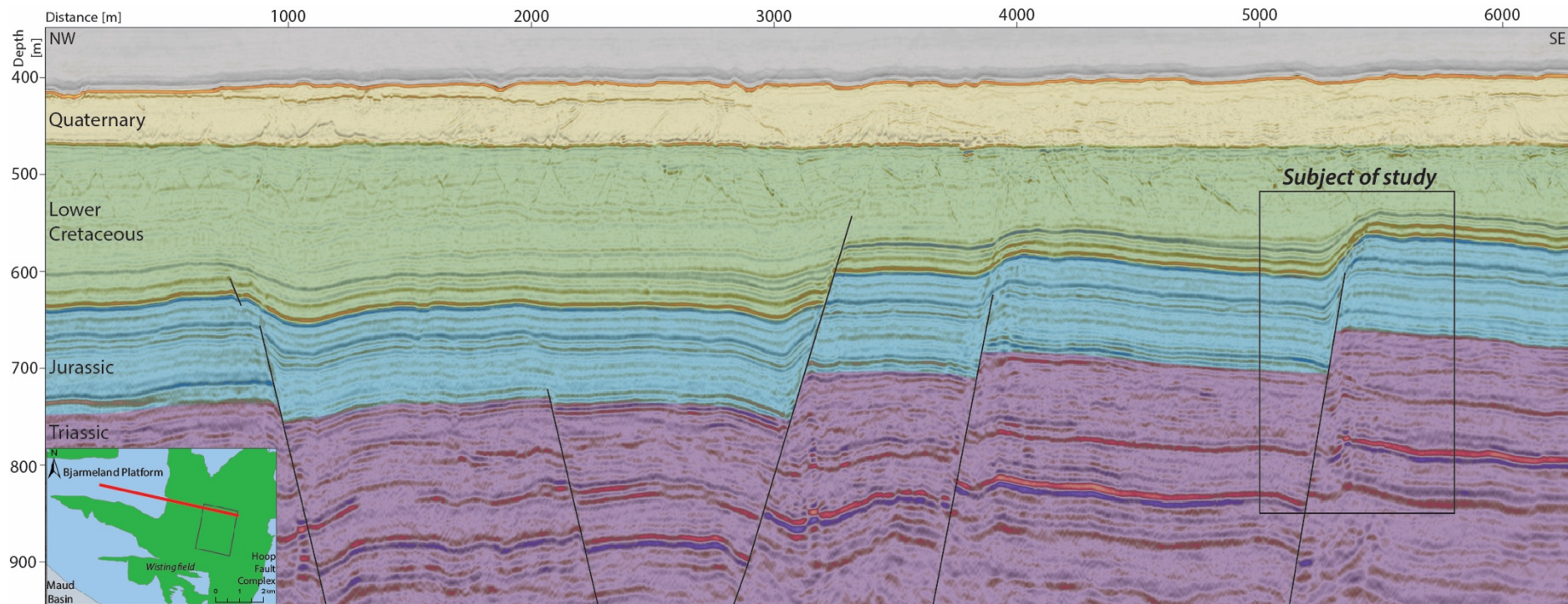
Figure 3: *Faults offset the Triassic, Lower- and Middle Jurassic successions and terminate upwards into folds in the overlying Upper Jurassic and Lower Cretaceous successions. The rectangle marks the monocline studied in this thesis. Vertical exaggeration (VE) = 4.0.*

The trishear kinematic model (Erslev, 1991; Allmendinger, 1998) has been applied to both compressional and extensional fault-propagation folds, and it has been found that this model replicates well the geometry and strain of these structures (Allmendinger, 1998; Cardozo et al., 2011; Hardy & Allmendinger, 2011; among others). Trishear is a relatively simple, incremental kinematic model for fault propagation folding. One issue with trishear, however, is that the model parameters cannot be determined directly from the geometry of the fold (Allmendinger, 1998). However, by performing trishear inverse modelling, we can find the model parameters that best fit and restore the structure (Allmendinger, 1998; Cardozo & Aanonsen, 2009; Cardozo et al., 2011). In addition, the uncertainty of the model parameters describing the fold geometry can be characterized (Cardozo & Aanonsen, 2009; Oakley & Fisher, 2015; Cardozo & Oakley, 2019).

1.1 Objectives

This study has two main objectives. First, to complete a careful geometrical description and characterization of an extensional fault-propagation fold in the Wisting field, Norwegian Barents Sea. For this objective, a 3D geological model consistent with the interpretation of the seismic horizons was constructed to describe:

- The interpreted horizons and their geometries
- Faults and their geometries
- Horizon-fault intersections or cutoffs
- Fault displacement distribution (e.g. throw)

The second objective is to perform kinematic modelling of the fault-propagation fold using the trishear model. Four depth-converted seismic sections perpendicular to the monocline were selected and used for the modelling. Fault slip, fault propagation to fault slip ratio (P/S), and the initial and final depth of the fault tip can be determined from the modelling. These results are integrated to propose an evolutionary model of the monocline. Additionally, as this fold is in a heavily compartmentalized and shallow oil field, these results can be used to evaluate the risk for upward fluid flow along faults and related monoclines in this area.

2   Geological Setting

The Barents Sea covers a shallow shelf area extending from the deeper Norwegian-Greenland Sea in the west to Novaya Zemlya in the east, and from the Norwegian and Russian coast in the south to Svalbard and the Arctic Ocean in the north (Figure 4). The major sedimentary basins are found just west of Novaya Zemlya, in the eastern part of the Barents Sea, while the western part has a different structural style consisting of smaller basins, structural highs and more widespread platform areas (Figure 4; Doré, 1995; Smelror et al., 2009; Henriksen et al., 2011b). The Bjarmeland Platform and the Hoop Fault Complex (with bold letters on Figure 4) are two of many structural elements of the western Barents Shelf which developed because of the tectonic history of the area. Within these tectonic provinces, or structural elements, different formations are found (Dallmann, 1999). In the study area, the Fruholmen and Stø formations of the Realgrunnen Subgroup (Kapp Toscana Group), and the Fuglen, Hekkingen, Klippfisk, Kolje and Kolmule formations of the Adventdalen Group are present (Figure 5).
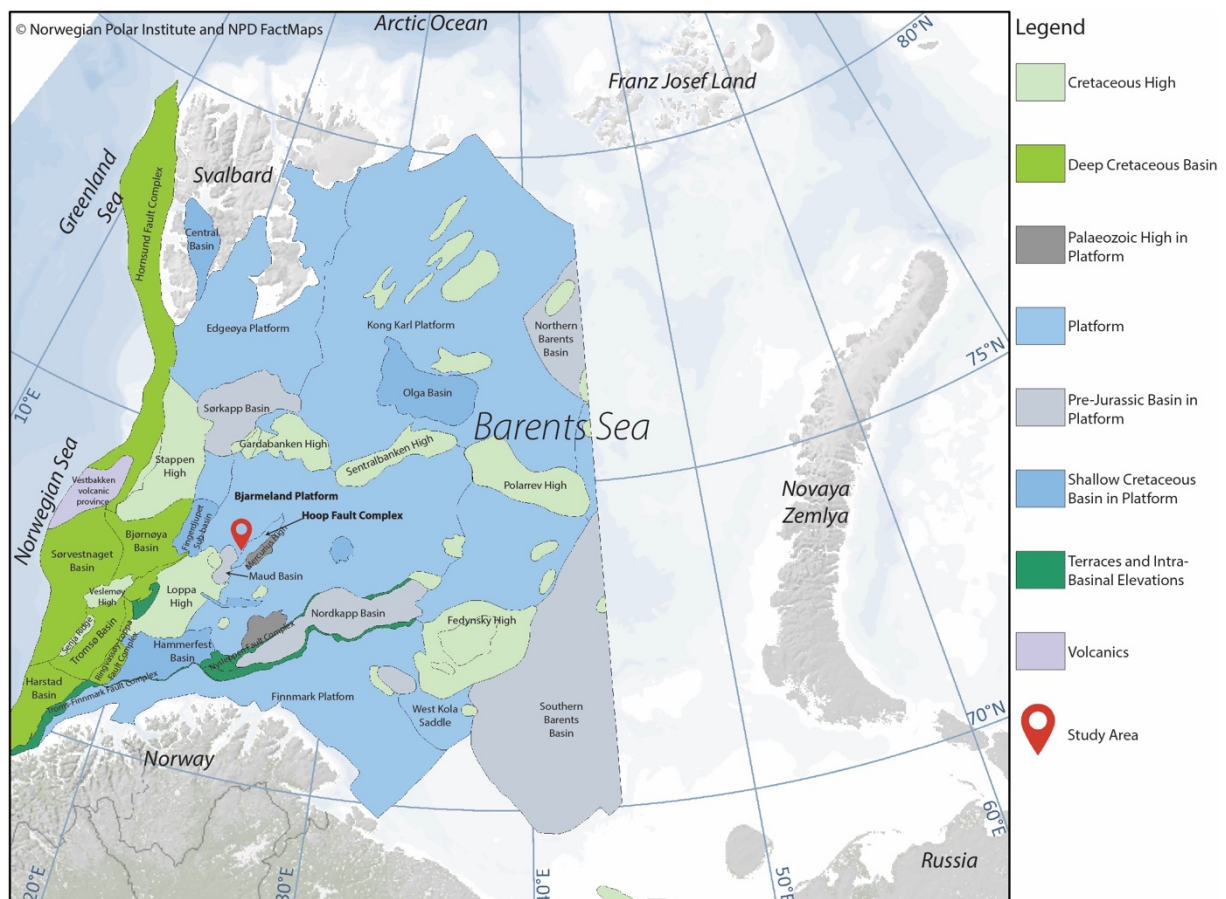
Figure 4: Location map of the western Barents Sea and the main tectonic provinces in this area. The Bjarmeland platform and Hoop Fault Complex are in bold letters. The study area is marked with a red pin. Base map from Norwegian Polar Institute (2020) and structural elements from NPD Factmaps (NPD, 2021).

The main geological setting of the Barents Shelf can be explained by two major continental collision events, three extensional episodes, and several uplift events (Figure 5; Faleide et al., 1993; Henriksen et al., 2011b). However, several minor tectonic phases have also contributed on a more local scale (Smelror et al., 2009). The main tectonic events and stratigraphic formations from the Middle/Upper Paleozoic to Cenozoic are shown on Figure 5.

2.1 Tectonic framework

The first major continental collision event in the Barents Sea was the Caledonian Orogeny between Laurentia and Baltica, which led to the closure of the Iapetus Ocean (Doré, 1995). This orogeny initiated in the Middle Ordovician, but the main tectonism was in the Silurian (Henriksen et al., 2011b). In general, the NE-SW structural orientation observed in the southwestern Barents Shelf, follows the principal Caledonian trend (Doré, 1995). The Permian – Triassic Uralian Orogeny also affected the Barents Shelf (Gudlaugsson et al., 1998; Petrov et al., 2008). The Caledonian Orogeny created positive topography to the west and a sediment distribution drainage system to the east. This pattern was reversed during the Uralian Orogeny where uplift affected the eastern Barents Shelf, causing sediment input to the west (Henriksen et al., 2011b).

Three dominant extensional episodes can be identified on the Barents Shelf: (1) post-Caledonian extension in the Late Paleozoic; (2) Middle Jurassic – Early Cretaceous extension associated with the Atlantic rifting; and (3) Tertiary extension particularly in the western Barents Sea related to the opening of the Norwegian-Greenland Sea during the Early Eocene, approximately 55-54 Ma (Faleide et al., 1993; Doré, 1995; Worsley, 2008; Smelror et al., 2009; Henriksen et al., 2011b). These extensional events resulted in the development of several major rift basins and widespread platform areas throughout the Barents Shelf.

The initiation of several sedimentary basins in the western Barents Sea (e.g., Nordkapp Basin and possibly also the Hammerfest Basin) may have started during the Late Paleozoic rifting (Gudlaugsson et al., 1998; Henriksen et al., 2011b). In the Triassic, the western Barents Sea experienced quiescence and thermal subsidence, but some tectonic movements are identified on the Bjarmeland Platform (Smelror et al., 2009) and Nordkapp Basin (Rojo et al., 2019). Uplift and erosion affected the shelf in the Late Triassic – Early Jurassic, eroding sediments from this stratigraphic interval (Smelror et al., 2009). The major basins and structural highs we recognize today in the western Barents Sea are believed to have been formed by the extension in Middle Jurassic – Early Cretaceous (Gabrielsen et al., 1990; Henriksen et al., 2011b).

Figure 5 stratigraphic chart — western Barents Sea

Sub-Era	Period	Epoch	Stage	Group	Formations	Lithostratigraphy	Megasequences
Cenozoic	Quaternary		Gelasian/Piacenzian/Pleistocene	Nordland			Shelf uplift
	Neogene	Pliocene	Zanclean/Messinian	Nordland			
		Miocene	Tortonian				
			Serravallian				
			Langhian				
			Burdigalian				
			Aquitanian				
	Paleogene	Oligocene	Chattian	Sotbakken			Sheared margin
			Rupelian				Rifting
		Eocene	Priabonian		Torsk		
			Bartonian				
			Lutetian				
			Ypresian				
		Paleocene	Thanetian				
			Selandian				
			Danian				
Mesozoic	Cretaceous	Late	Maastrichtian	Nygrunnen	Kveite / Kvit-ing		Platform uplift
			Campanian				
			Santonian				
			Coniacian				
			Turonian				
			Cenomanian				
		Early	Albian	Adventdalen	Kolmule		Rifting
			Aptian				
			Barremian		Kolje		
			Hauterivian		Knurr		Rifting
			Valanginian		Klippfisk		
			Berriasian				
	Jurassic	Late	Tithonian		Hekkingen		Rifting
			Kimmeridgian				
			Oxfordian		Fuglen		
		Middle	Callovian	Kapp Toscana			
			Bathonian				
			Bajocian		Stø		
			Aalenian				
		Early	Toarcian		Nordmela		
			Pliensbachian				
			Sinemurian		Tubåen		
			Hettangian				
	Triassic	Late	Rhaetian		Fruholmen		Regional subsidence
			Norian				
			Carnian		Snadd		
		Middle	Ladinian	Sassendalen	Kobbe		
			Anisian				
		Early	Olenekian		Klappmyss / Havert		
			Induan				
Paleozoic	Permian	Lopingian	Changhsingian	Tempel-fjorden	Ørret		Ural mountain chain in the east, rifting in the west
			Wuchiapingian				
		Guadalupian	Capitanian		Røye		
			Wordian				
			Roadian				
		Cisuralian	Kungurian	Bjarme-land	Isbjørn		
			Artinskian				
			Sakmarian		Polarrev		
			Asselian		Ørn		
	Carboniferous	Late Pen.	Gzhelian	Gipsdalen			
			Kasimovian				
		Middle Pen.	Moscovian		Falk		
		Early Pen.	Bashkirian		Ugle		
		Late Mis.	Serpukhovian	Billefjorden	Blærerot		Rifting
		Middle Mis.	Visean		Tettegras		
					Soldugg		
		Early Mis.	Tournaisian				
	Devonian	Late	Famennian				

Figure 5: Lithostratigraphy and main tectonic events of the western Barents Sea. Modified from Glørstad-Clark et al. (2010).

Thick Cretaceous strata are recognized within several basins. They are the result of subsidence during this period, together with sediment infill from the uplifted northeastern Barents Shelf (Smelror et al., 2009; Henriksen et al., 2011b). Further west, thicker Cenozoic strata are observed. These strata were deposited during Cenozoic subsidence and considerable sediment transport from the uplifted shelf to the north and east (Smelror et al., 2009). However, on structural platforms (e.g. the Bjarmeland Platform), the Cenozoic strata underlying the Quaternary strata are completely eroded (Gabrielsen et al., 1990).

In the study area, the base of the Quaternary glacial deposits uncomfortably overlies the Lower Cretaceous strata (Figure 6). This unconformity is called the Upper Regional Unconformity (URU) and is recognized in the western Barents Shelf (Henriksen et al., 2011b; Faleide et al., 2019). It was caused by Paleogene to recent uplift and erosion of the shelf east of the western margin (Riis & Fjeldskaar, 1992; Riis, 1996; Henriksen et al., 2011a; Henriksen et al., 2011b). The erosion during the late Pliocene and Pleistocene glaciations shaped the URU and had large impact on the geology of the Barents Sea (Gabrielsen et al., 1990; Smelror et al., 2009; Bellwald et al., 2019). The erosion products from the glaciations were mainly deposited in the western margin during the Late Pliocene – Pleistocene (Worsley, 2008; Smelror et al., 2009).

A high exploration risk in the Barents Sea is related to the integrity of reservoirs and cap rocks (top seals) due to the tectonic history of the area, specially the uplift and erosion events (Paulsen et al., 2019). However, hydrocarbon discoveries are found at the Wisting field where the reservoirs are at shallow depth, less than 500 m below the seabed (Stueland, 2016), and they are highly compartmentalized by faults.

2.1.1 Bjarmeland Platform

The Bjarmeland platform is a widespread area, which is believed to have been relatively stable since the Late Paleozoic (Gabrielsen et al., 1990). Other structural elements are located within the platform, e.g., the Maud Basin and part of the Hoop Fault Complex.
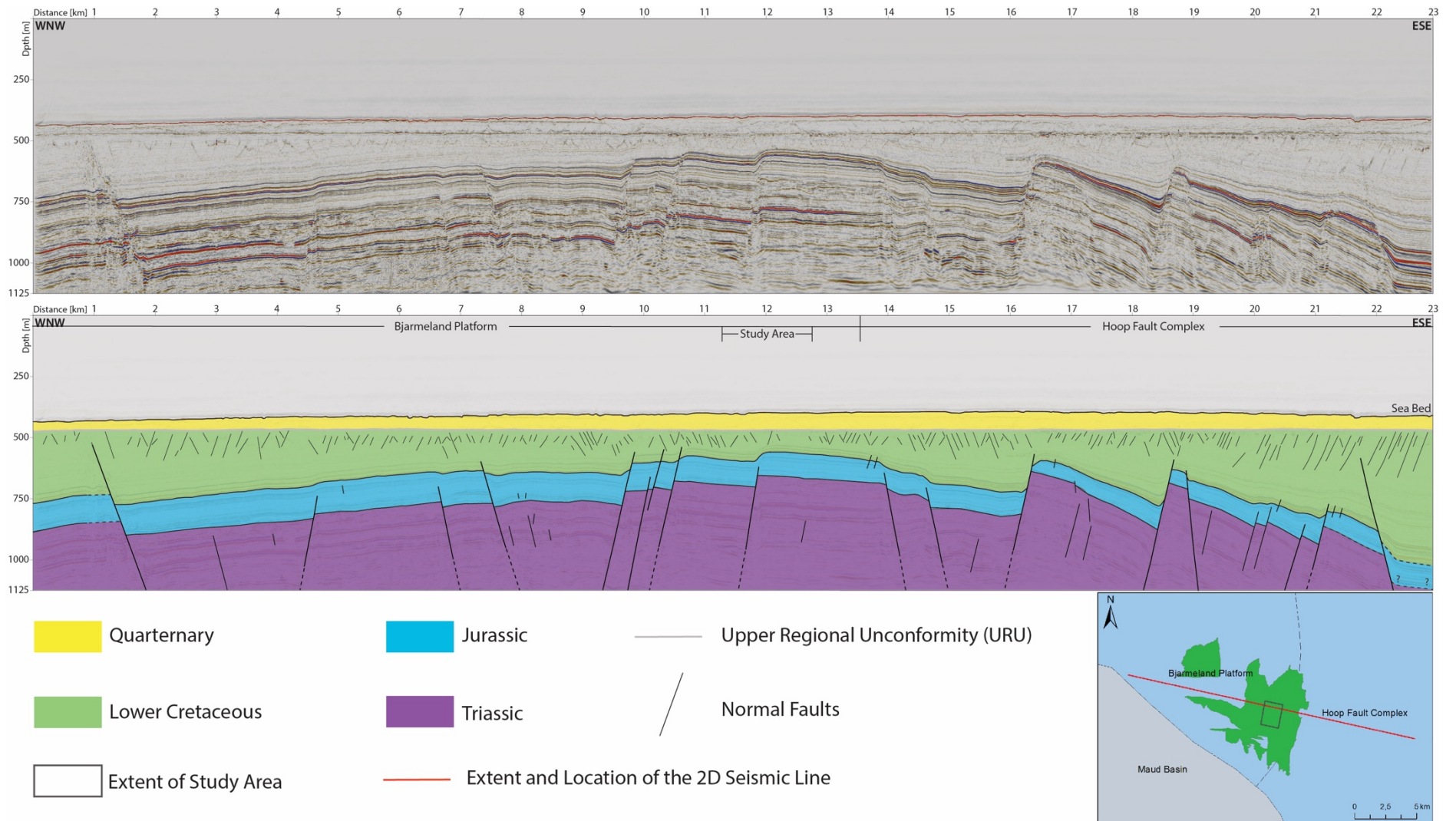
Figure 6: Seismic line covering the study area and nearby regions. Note that the Tertiary and Upper Cretaceous successions are missing in the study area. The seabed is located at approximately 400 m depth. VE = 4.0.

2.1.2 Hoop Fault Complex

The NE – SW trending Hoop Fault Complex is one of the principal fault complexes on the SW Barents Shelf and is considered an older zone of weakness (Gabrielsen et al., 1990; Collanega et al., 2017). Tectonic movement in the central part of the complex is believed to have affected the Late Paleozoic depositional pattern (Gabrielsen et al., 1990). The Hoop Fault Complex is dominated by normal faulting, and it is believed to have been reactivated in the Middle Triassic, Late Jurassic – Early Cretaceous and Tertiary (Gabrielsen et al., 1990).

Collanega et al. (2017) discuss the orthorhombic style of the Hoop Fault Complex and they recognize four fault systems of different orientations: NE–SW, N–S, NNE–SSW and WNW-ESE (Figure 7). These fault systems formed during the late Mesozoic–Cenozoic, influenced by both the Atlantic and Arctic rift events (Collanega et al., 2017). A study of the area centered around the Hoop Fault Complex by Faleide et al. (2019) suggests a likely Aptian–early Albian age for the main Early Cretaceous faulting in the Hoop area.
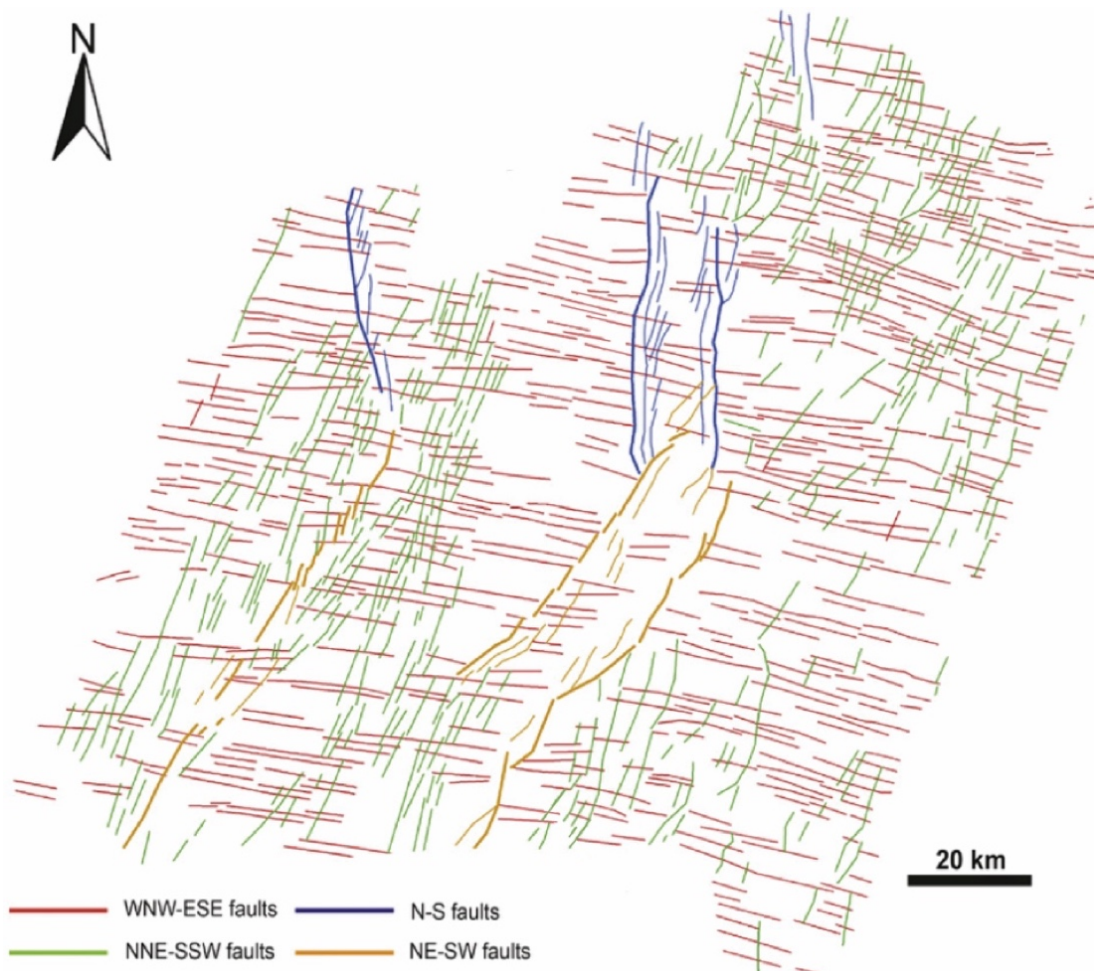
Figure 7: Four main fault systems in the Hoop Fault Complex identified by Collanega et al. (2017). Modified from Collanega et al. (2017).

2.2   Stratigraphic framework

2.2.1   *Realgrunnen Subgroup*

The Upper Triassic to Middle Jurassic stratigraphic succession in the Barents Sea is represented by the Realgrunnen Subgroup within the Kapp Toscana Group, and from oldest to youngest this Subgroup consists of the following formations: Fruholmen, Nordmela, Tubåen and Stø (Figure 8; Dallmann, 1999). The Realgrunnen Subgroup contains the main reservoirs in the Wisting field (Granli et al., 2017). The following sections describe the formations belonging to the Realgrunnen Subgroup and which are present in the study area.

2.2.1.1   *Fruholmen Formation*

The Fruholmen Formation is of Norian to Rhaetian age (Triassic/Jurassic boundary). It consists mainly of shale at the base of the formation, whereas interbedded sandstones, shales and coals are more common up-section (Worsley et al., 1988). The depositional environment is open marine to fluvial and fluviodeltaic (Dallmann, 1999).

2.2.1.2   *Stø Formation*

The Stø Formation is of late Pliensbachian to Bajocian age. It consists of sandstone, shale and siltstone, where mineralogically mature and moderate to well-sorted sandstones dominate (Worsley et al., 1988). The sandstones were deposited in a prograding coastal regime where siltstone and shale intervals indicate transgressive episodes during the late Toarcian and late Aalenian (Dallmann, 1999). The Stø Formation has excellent reservoir qualities and is the most important reservoir in the Wisting field (Granli et al., 2017).
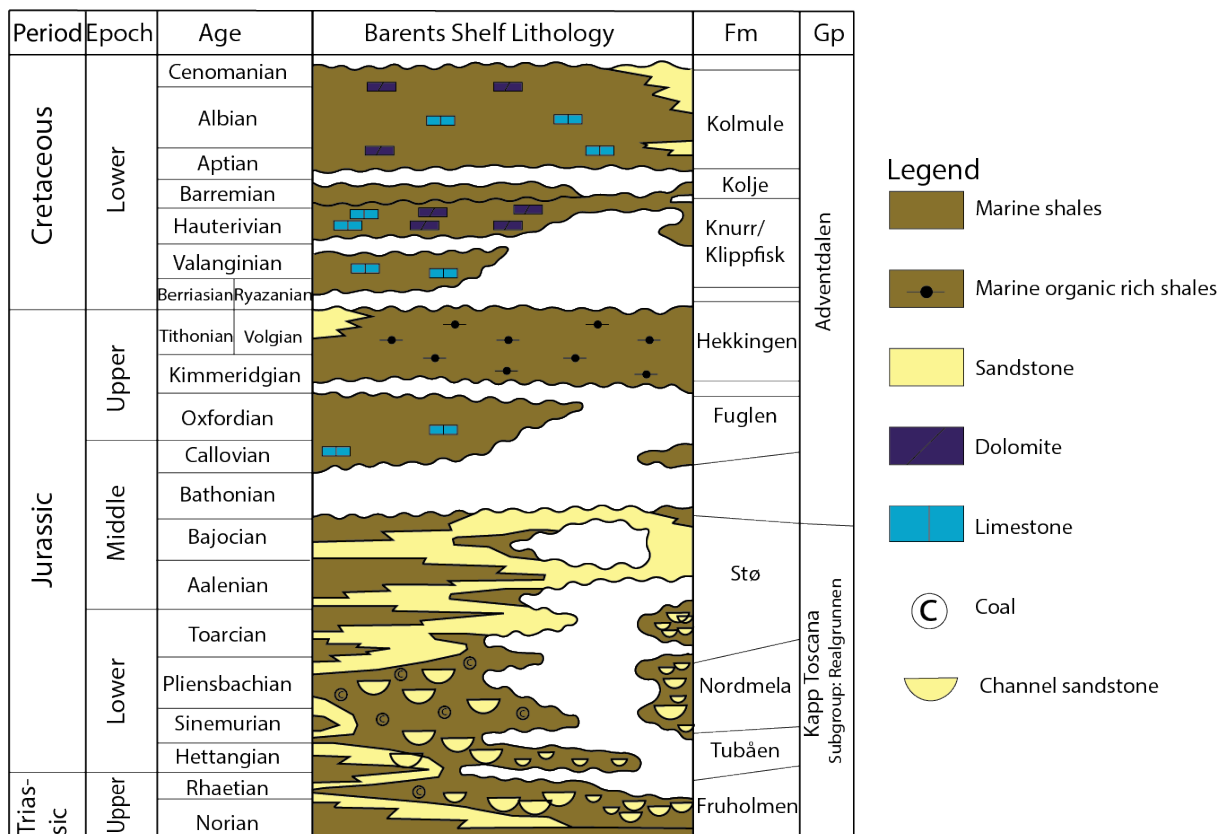
Figure 8: *Stratigraphic framework of the main Upper Triassic, Jurassic and Lower Cretaceous successions in the western Barents Sea. Modified from Nøttvedt et al. (1993).*

2.2.2   Adventdalen Group

The Upper Jurassic – Lower Cretaceous succession on the Barents Shelf is represented by the Adventdalen Group, which from oldest to youngest is subdivided into the following formations: Fuglen, Hekkingen, Knurr, Klippfisk, Kolje and Kolmule (Dallmann, 1999). The Klippfisk and Knurr formations are time equivalent, but the Klippfisk Formation is more present on platform areas and changes laterally into the more basinal Knurr Formation (Smelror et al., 1998).

Marine shales or mudstones dominate in the Adventdalen Group, but deltaic/shelf sandstones and thin carbonate beds are also present (Figure 8; Dallmann, 1999). The Adventdalen group is essential for the petroleum system of the Barents Sea as the Hekkingen Formation is an important hydrocarbon source rock, and the Fuglen Formation acts as a cap rock (Dallmann, 1999; Klausen et al., 2019). The following sections describe the formations belonging to the Adventdalen Group and which are present in the study area.

12

2.2.2.1 Fuglen Formation

The Fuglen Formation is of late Bathonian to middle Oxfordian age. It consists mainly of mudstone with thin limestone interbeds deposited in a marine shelf setting (Dallmann, 1999). The Fuglen Formation is immediately above the reservoir interval of the Realgrunnen Subgroup in the Wisting Field (Moskvil et al., 2018; Klausen et al., 2019).

2.2.2.2 Hekkingen Formation

The Hekkingen Formation is of late Oxfordian to Volgian age. It consists mainly of mudstones and shale, sometimes interbedded with thin limestone, dolomite, siltstone and sandstone beds (Dallmann, 1999). The claystones have a high organic content and are a very important hydrocarbon source rock in the area (Stueland, 2016; Paulsen et al., 2019). The formation is deposited in a deep marine setting with anoxic conditions (Dallmann, 1999).

2.2.2.3 Klippfisk Formation

The Klippfisk Formation is of late Berriasian to Hauterivian age. It is mainly present in platform areas (e.g., Bjarmeland Platform) and consists of condensed carbonate (limestones and marls) successions (Dallmann, 1999). The Klippfisk Formation was deposited in a transgressive sequence in a shallow marine setting (Smelror et al., 1998).

2.2.2.4 Kolje Formation

The Kolje Formation is of Barremian to early Aptian age. It consists of shales and mudstones with minor limestone and dolomite beds (Dallmann, 1999). It was deposited in a distal open marine setting (Smelror et al., 1998).

2.2.2.5 Kolmule Formation

The Kolmule Formation is of Aptian – middle Cenomanian age. It consists of mudstone and shale with thin interbedded siltstones and carbonate stringers deposited mainly in an open marine environment (Dallmann, 1999). In the study area, the top of the Kolmule Formation represents a regional unconformity, URU, which separates the Kolmule Formation from the overlying Quaternary deposits (Faleide et al., 2019).

3 Data and Methodology

3.1 Database

All data in this study are retrieved from Diskos, which is Norway's petroleum data repository coordinated and managed by the Norwegian Petroleum Directorate (NPD). An overview of the available data in this study is displayed on Figure 9.
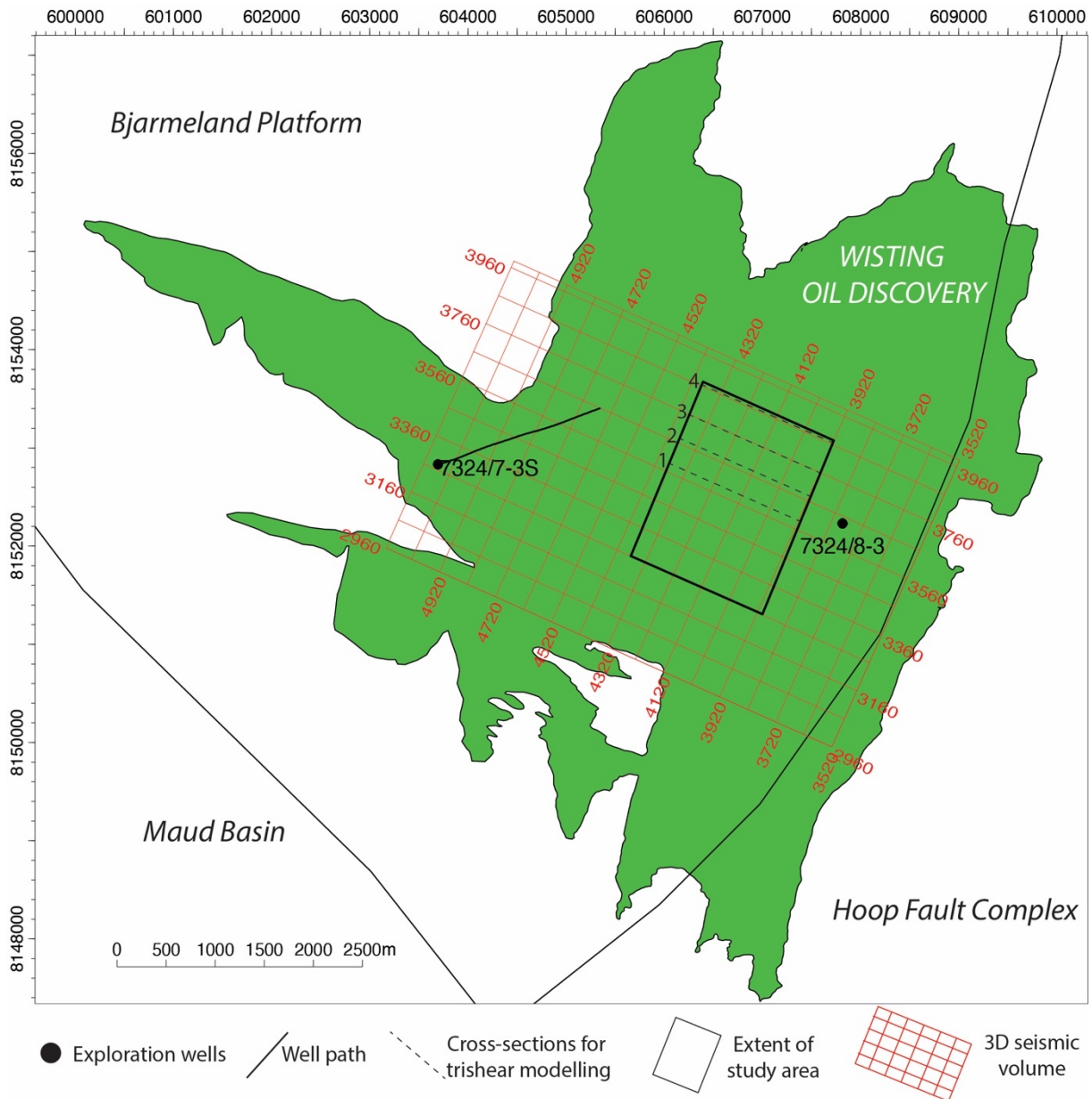
Figure 9: Overview of study area and data available.

Well data from two exploration wells (7324/7-3S and 7324/8-3) located approximately 4.2 km apart were integrated to determine lithology and shale volume in the stratigraphic formations. The formation tops present in the wells were imported from NPD FactPages (NPD, 2018, 2019).

The seismic data were acquired in 2016 by the operator OMV and they comprise a 3D high-resolution P-Cable seismic cube covering the Wisting field (Moskvil et al., 2018). These data are in the depth domain and have a 3.125 x 3.125 m bin size. A seismic reflection event that indicates an increase in acoustic impedance is represented by a seismic wavelet polarity that displays a positive amplitude (Figure 10).
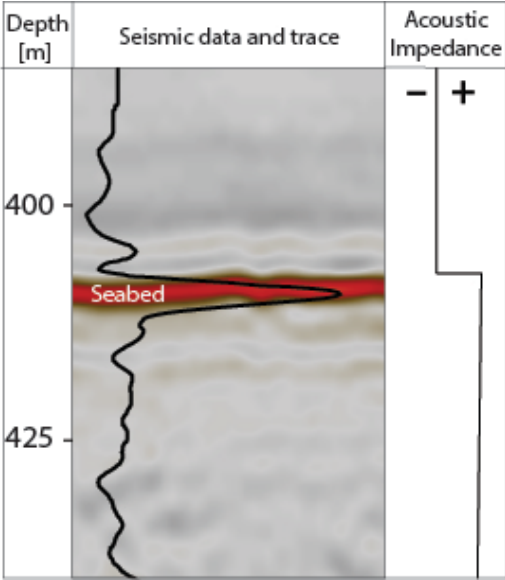
Figure 10: Seismic polarity. An increase in acoustic impedance represents a peak or a positive amplitude response.

The 3D seismic cube area is 362 km^2. However, the study area of the monocline covers only 3 km^2, and therefore the seismic cube was cropped to 16km^2 to focus on the area of interest.

3.2 Methods

Interpretation of the subsurface well and seismic data, as well as construction of the structural model was performed in the software Petrel (Schlumberger). Then this model was exported to the software Move (Petroleum Experts) to perform more detailed geometrical analyses of the interpreted horizons and faults (section 3.2.3).

3.2.1 Well data

The available well data (e.g, gamma ray, neutron, density, resistivity and sonic logs) were used for a basic lithology determination and seismic-well ties. Generally, low gamma ray values are associated with sandstones and/or carbonates, whereas high gamma ray values are interpreted as shales (Figure 11; Mondol, 2015). A combination of the density and reversed neutron log were also utilized to identify different lithologies (Figure 11; Mondol, 2015): (1) Shaly intervals are represented by higher neutron values and thus a larger positive separation between the log readings, (2) lower values of neutron and density and a crossover of the two logs (negative separation), are observed in the sandy intervals, (3) a sequence represented by switching positive and negative separations between the density and neutron logs are interpreted as sandstone/carbonate and shale interbeds.
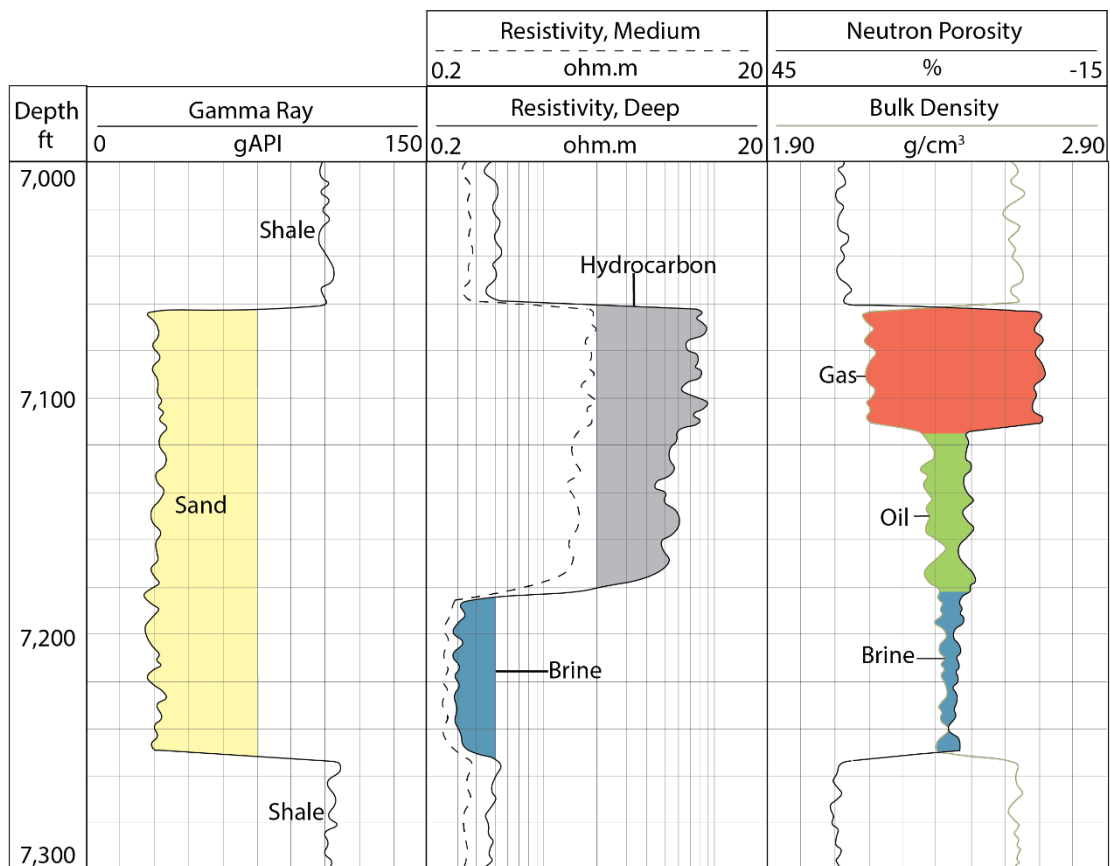
Figure 11: *A basic well log interpretation based on gamma ray, medium and deep resistivity, neutron porosity and bulk density. Modified from Andersen (2016).*

The resistivity log was utilized to indicate fluid content within the lithologies (Figure 11). Water-saturated sediments have a high conductivity and thus a low resistivity, while hydrocarbons are nonconductive and have higher resistivity values (Andersen, 2016). The available sonic log represents the transit time, which is the reciprocal of velocity (Andersen, 2016). The velocity varies in shales and sandstones depending on the mineralogy, but generally dense and compacted rock will have a higher velocity compared to unconsolidated sediments (Mondol, 2015).

Based on the gamma ray, the volume of shale in the respective formations was calculated. First, the gamma ray index (I_{GR}) was calculated, and then the shale volume (V_{sh}). The formulae of Larionov (1969) for older rocks was used in this thesis (Mondol, 2015) :

$$I_{GR} = \frac{GR_{log} - GR_{min}}{GR_{max} - GR_{min}} \qquad (1)$$

$$V_{sh} = 0.33 \times (2^{2 \times I_{GR}} - 1) \qquad (2)$$

where GR_{log} is the gamma ray reading, GR_{min} and GR_{max} are the minimum and maximum gamma ray values, respectively.

3.2.2 Seismic data

The high-resolution 3D seismic data were used for detailed interpretation and mapping of key horizons and faults. A synthetic seismogram was generated prior to the seismic interpretation (Figure 12). The calculated acoustic impedance (from the sonic and density logs) was converted to the time-domain and used for the reflectivity calculation. The wavelet for the synthetic generation was extracted in the time-domain, and since the seismic data utilized in this thesis are in the depth-domain, the resulting synthetic trace was converted back to the depth-domain (Schlumberger, 2020). The synthetic trace was compared with the seismic response at the well location (Figure 12). In this way, the formation tops in the wells were correlated to their respective seismic reflections, making possible to identify (via the formation tops) the seismic horizons that were picked (Figure 12; Mondol, 2015).

Nine horizons were interpreted and mapped in this study (Figure 13). Each interpretation was conducted at the well locations where the stratigraphic tops are known. The horizons were then interpreted throughout the seismic using mainly the seeded 2D auto tracking tool. However, manual interpretation was also performed mainly at the vicinity of faults to achieve a detailed interpretation of the horizons and fault relationships. Generally, all seismic horizons have good lateral continuity throughout the seismic cube.

One fundamental problem with the seismic cube are fault shadows, which are visualized as footwall sags in the vicinity of large normal faults (Figure 14; Hardwick & Rajesh, 2013). Hardwick and Rajesh (2013) explain that these footwall sags are seismic artefacts caused by rapid velocity variations and high velocities in the overburden, resulting in distorted ray paths. Moskvil et al. (2018) discuss these fault shadows and mention that they can result from a combination of reflections and refractions, but this is speculative and has not been confirmed. Thus, careful manual interpretation in these areas was performed to avoid these artifacts.
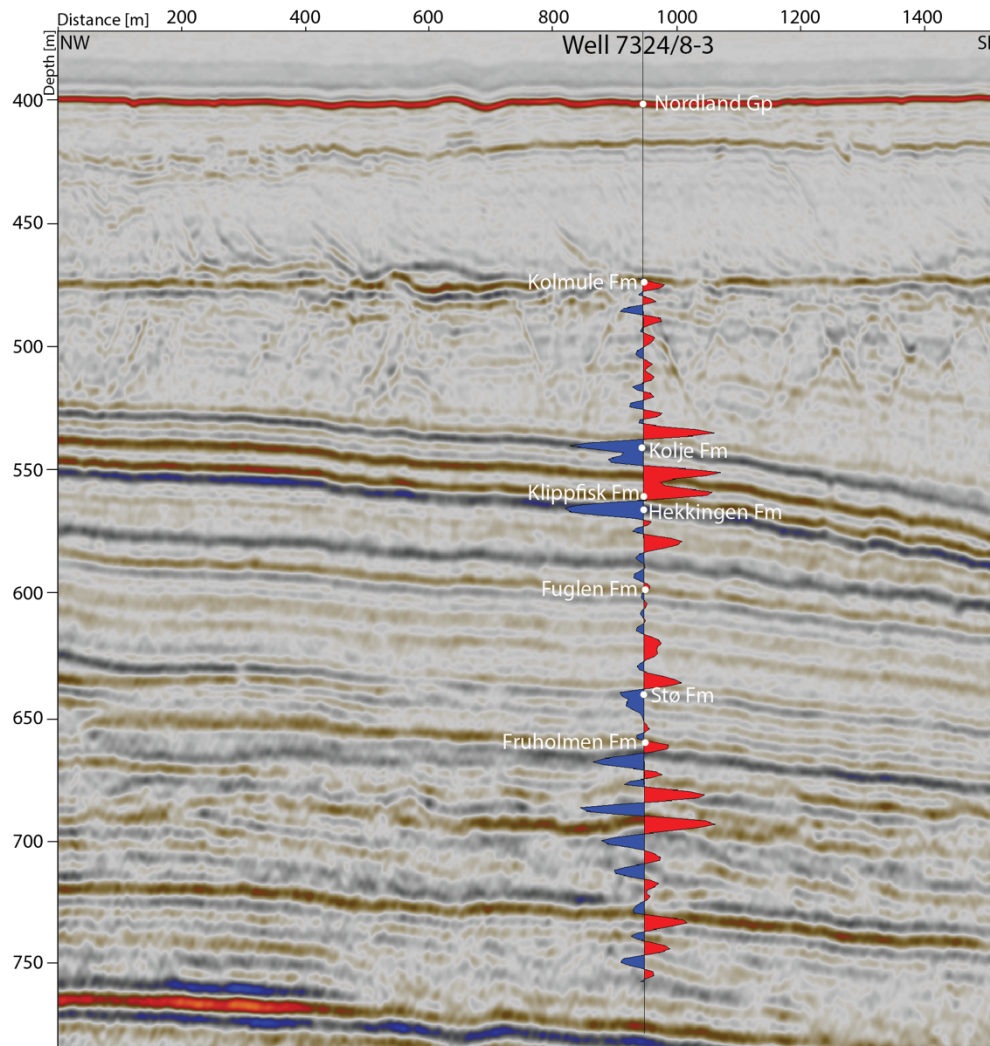
Figure 12: *The synthetic trace created from the seismic-well tie. Formation tops and seismic horizons were correlated at the location of well 7324/8-3. VE = 4.0.*

The seismic inlines were interpreted first. On average, every 5th inline was interpreted in the model area to accomplish a detailed interpretation. Sometimes a smaller increment was used in more complex areas close to the faults. Finally, the crosslines were interpreted carefully at the vicinity of the faults, before the 3D auto track tool was used to fill in the gaps between the interpreted lines. The fault interpretation was facilitated by applying the variance attribute to

the depth slices. Faults can be detected by a continuous and high variance response (Schlumberger, 2015).
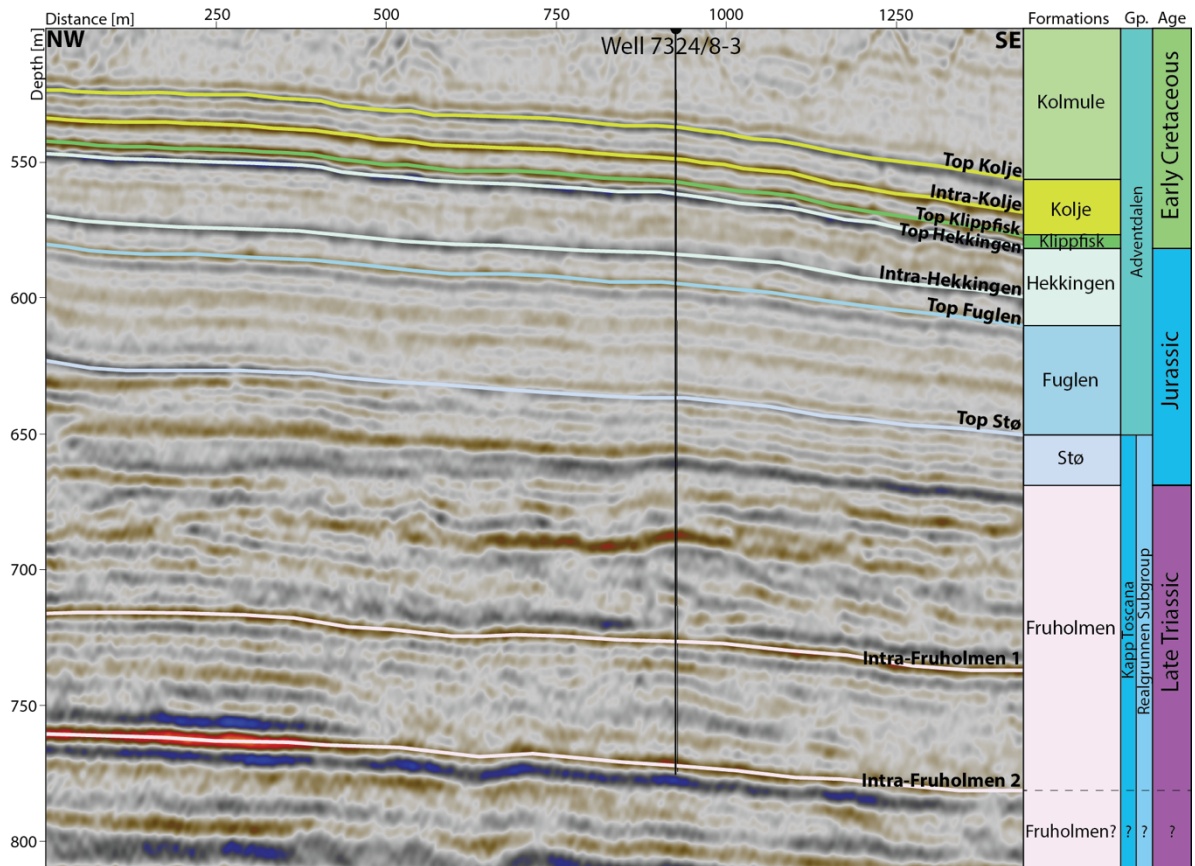
Figure 13: *The interpretations of the nine horizons were conducted at the well locations where the well tops are known. VE=4.0.*
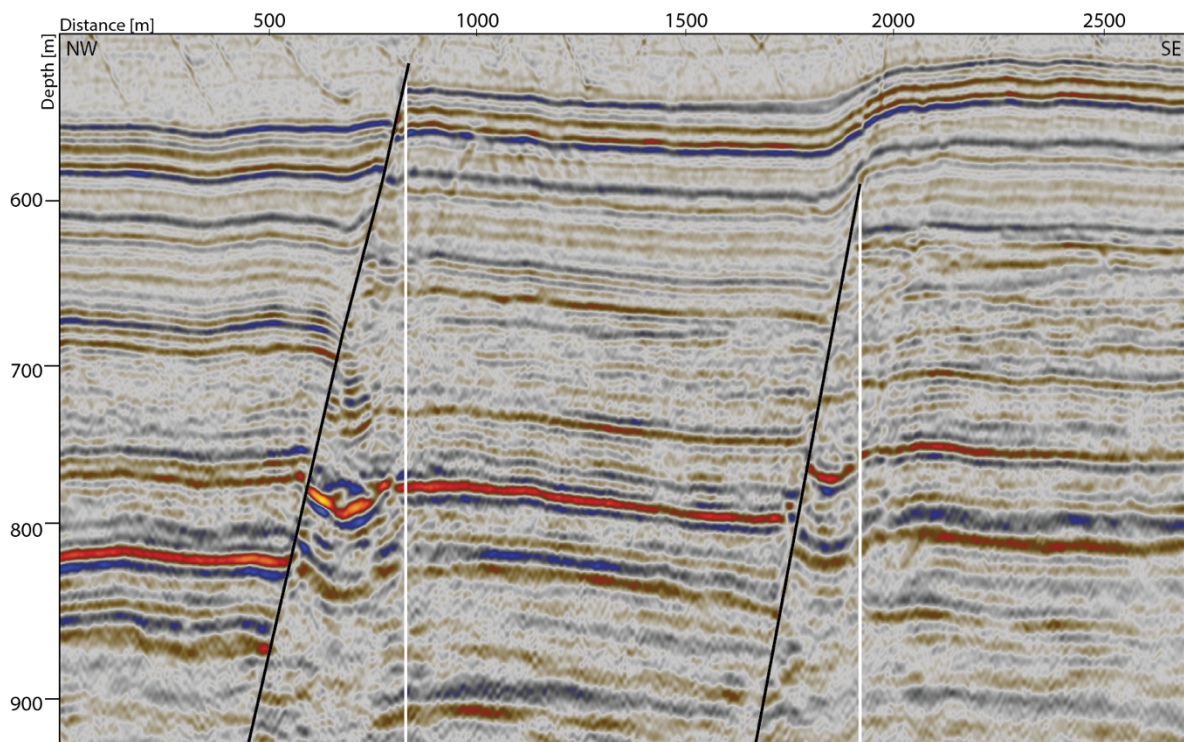
Figure 14: *Seismic section showing fault shadows or artificial footwall sags at the vicinity of faults. VE = 4.0.*

19

3.2.3 Geometrical analysis

Structure- and thickness maps of the interpreted horizons were created to get a better understanding of the geometry of the horizons and faults in the study area. A 3D geological model was constructed based on the detailed interpretation of the model area around the monocline. The model was conditioned as this is an important step for further analysis. This involved smoothing the surfaces to remove noise, and making sure that the horizon-fault intersections were consistent (Petroleum Experts, 2020a).

Attributes associated with the shape of the surface were applied to the resulting model surfaces. Dip and the local strike were extracted from the folded surfaces. These data were plotted on a stereonet to define the fold axis, which is the pole to the cylindrical best-fit plane to the bedding poles (Figure 15; Suppe, 1985). The fold axis is approximately horizontal and trends ~ N20E (Figure 15). The seismic inlines are approximately perpendicular to the fold axis (Figure 9), and therefore they are appropriate to visualize the cross-sectional geometry of the monocline.
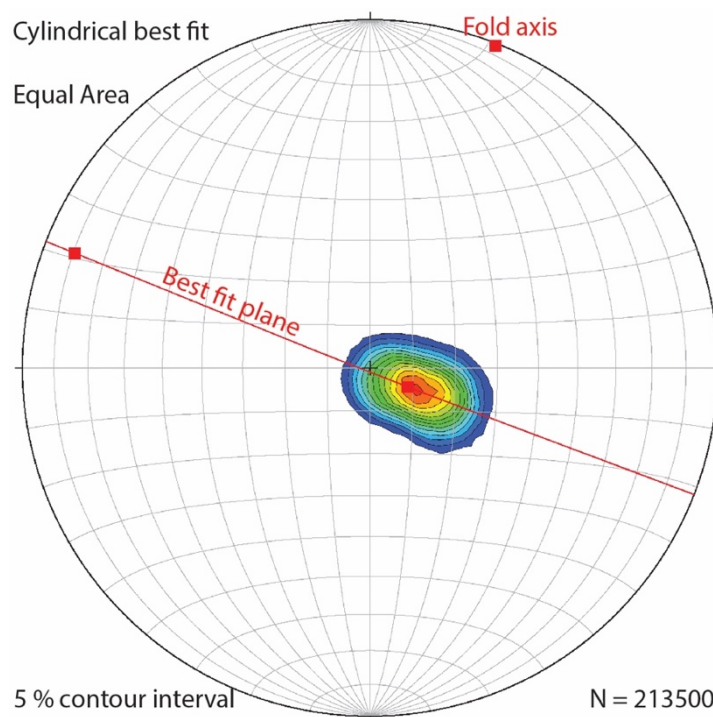
Figure 15: *Lower hemisphere equal area stereonet with 5 % contour interval of poles to bedding for the six folded horizons in the study area. A cylindrical best-fit to the poles indicates a ~horizontal fold axis trending N20E. N is the number of poles. Made with the program Stereonet3D by Nestor Cardozo (Cardozo & Allmendinger, 2013).*

The curvature attribute was applied to the smoothed folded surfaces to describe their geometry. Suppe (1985) explains how the curvature of a folded line is derived (Figure 16A): The curvature of the line at point P_1 can be calculated by tracing normals to the line at P_1 and a nearby point P_2. The distance from the point of intersection of the two normals and P_1 is referred to as R_1. The radius of curvature (R) at point P_1 is the limit value to which R_1 approaches as we choose P_2 closer and closer to P_1. The curvature, k, of a two-dimensional line equals the reciprocal of the radius of curvature (R) (Suppe, 1985):

$$k = \frac{1}{R} \hspace{4cm} (3)$$

Consequently, a horizontal line will have an infinite radius of curvature and zero curvature, while a tight fold will have a short radius of curvature and thus a higher value of curvature. Figure 16B shows the difference between positive, zero, and negative curvature (Roberts, 2001). In the case of a straight line, the vector normals to the line are parallel and thus they
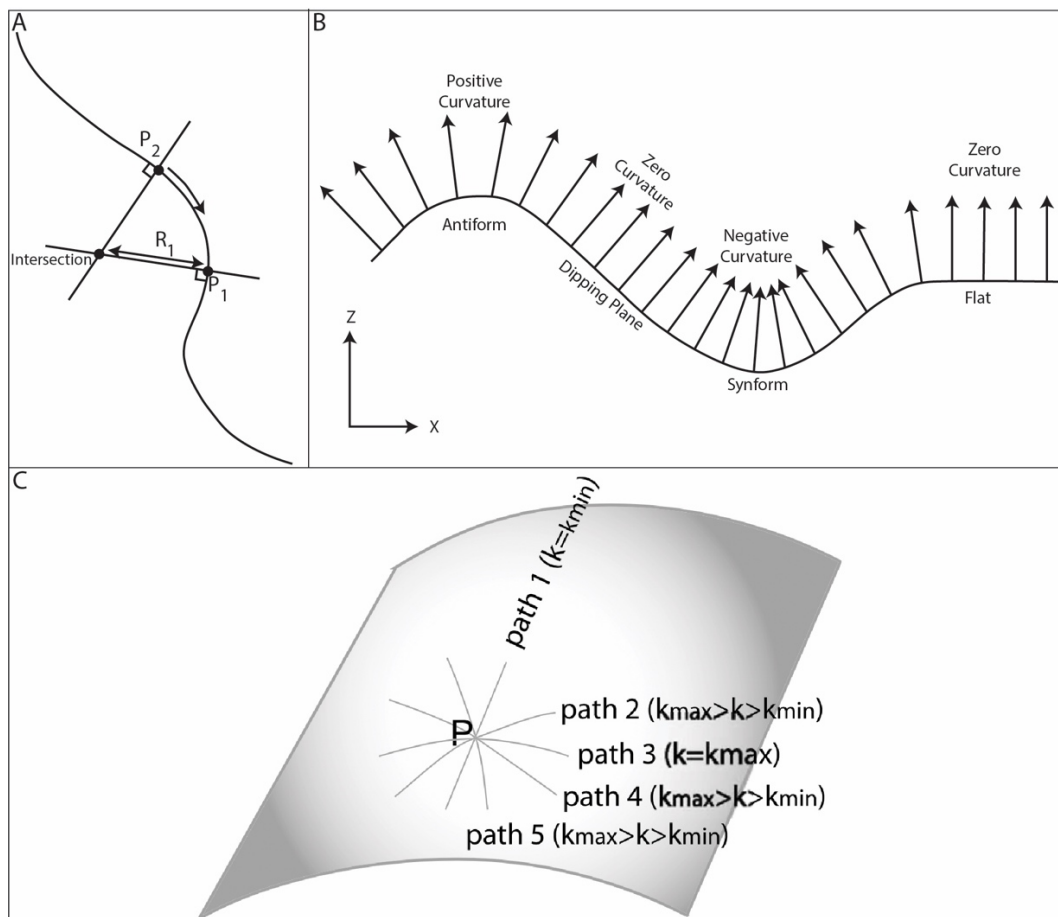
Figure 16: *A) Curvature in two-dimension modified from Suppe (1985). The curvature at point P_1 depends on the radius of curvature (R). B) Positive and negative curvature in two-dimensions from Roberts (2001). C) Curvature in three-dimensions from Bergbauer and Pollard (2003). The curvature of a point depends on the direction it is calculated. The normal curvature will have a minimum and a maximum magnitude in two directions (path 1 and 3) which are perpendicular to each other.*
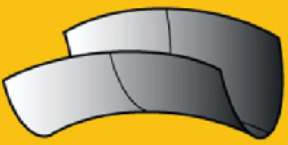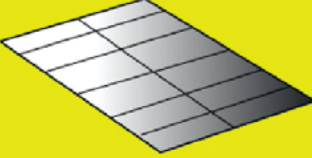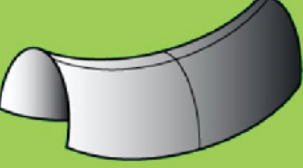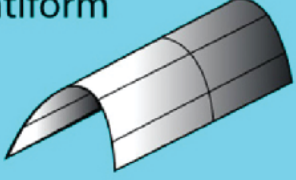
define a local zero curvature. When the line has an antiformal shape, the vector normal diverge and define a positive curvature. Conversely, when the line has a synformal shape, the vector normals converge and define a negative curvature.

In three-dimensions, the curvature of a specific point on a surface can have different values depending on the direction used for the curvature calculation (Figure 16C; Roberts, 2001; Mynatt et al., 2007). However, there will always be two orthogonal directions along which the calculated curvature is maximum (k_{max}) and minimum (k_{min}) (Figure 16C). These directions are known as the principal directions of curvature (Bergbauer & Pollard, 2003). If we consider a point P located on a cylindrical folded surface (Figure 16C), the minimum curvature (k_{min}) will be zero and it will be parallel to the hinge line, whereas the maximum curvature will be perpendicular to the hinge line. The hinge line is the line that connects the points of greatest maximum curvature (Marshak & Mitra, 1988). Gaussian curvature (k_G) and the mean curvature (k_M) are two important surface properties, which are based on the two principal curvatures (Roberts, 2001):

$$k_G = (k_{max})(k_{min}) \tag{4}$$

$$k_M = (k_{min} + k_{max})/2 \tag{5}$$

Notice that the Gaussian curvature (k_G) of a cylindrical folded surface at any point is zero (since k_{min} or k_{max} is zero; Suppe, 1985). The Gaussian- and the mean curvature alone are not useful to visualize or differentiate local shapes and orientations of the folded surface (Roberts, 2001). However, a combination of these two curvatures can be used to describe the geometry of a surface (Figure 17; Bergbauer and Pollard, 2003; Bergbauer, 2007; and Mynatt et al., 2007, among others). If both principal curvatures are zero, k_G and $k_M = 0$ and the surface is planar. If one of the principal curvatures is zero, $k_G = 0$ and it indicates a cylindrical surface that is either a synform or an antiform. If $k_G < 0$, the principal curvatures have opposite signs and indicate a saddle. If $k_G > 0$, the principal curvatures have the same sign and indicate either a basin or a dome (Figure 17). To determine whether the surface is a synform or an antiform, a basin or a dome, one can use the k_M curvature (Figure 17; Roberts, 2001). $k_M < 0$ indicates a synform or a basin, while $k_M > 0$ indicates an antiform or a dome (Figure 17).

Figure 17: Local shapes and orientations of a folded surface can be identified by combining the gaussian- and mean curvatures (k_G and k_M respectively). From Mynatt et al. (2007).

To achieve an idealized cylindrical shape in nature, the principal curvatures which are oriented parallel to the anticlinal and synclinal hinge lines must equal 0 at each point (Figure 17; Bergbauer, 2007; Mynatt et al., 2007). This does not occur in natural folds, e.g. due to the irregularity of geological surfaces (Mynatt et al., 2007). However, approximating the folded surface to an idealized cylindrical form can be useful to describe the structure (Figure 15). Additionally, one can estimate how much the structure deviates from the idealized cylindrical form by calculating the curvature magnitudes that depart from the perfectly cylindrical fold shape (Bergbauer, 2007). This can be accomplished by using a curvature filter for which curvature values below an absolute threshold value for k_{min} and k_{max}, are set to 0 (Mynatt et al., 2007). By doing so, smaller and more local geometries in the surface are filtered out, and larger structural geometries/trends are visualized (Petroleum Experts, 2020b).

3.2.4 Kinematic modelling

Kinematic modelling of four key seismic sections in the study area was performed. Each of the cross sections is perpendicular to the fold axis and represents differences in folding and/or fault propagation along the monocline. From SW to NE, these cross sections are referred to as 1, 2, 3 and 4 (Figure 9).

The kinematic model used to simulate the monocline is called trishear. In this model, the slip along the fault is accommodated by folding of the overlying beds in a triangular zone focused on the propagating fault tip (Erslev, 1991; Allmendinger, 1998). The geometry of key horizons across the fold was interpreted on the four cross sections. Based on this interpretation, 2D trishear modelling was performed. Specifically, I used the simplest trishear model for a symmetric trishear zone and linear velocity (incremental fault slip) across the trishear zone (Eq. 4 of Zehnder & Allmendinger, 2000, with $s = 1$). Six parameters are associated with this model, and they allow to characterize the fold geometry and fault propagation evolution (Allmendinger, 1998; Zehnder & Allmendinger, 2000). These parameters are (Figure 18): 1. The horizontal (x) and 2. vertical (y) coordinates of the current fault tip, 3. the fault dip or ramp angle, 4. the fault propagation to slip ratio (P/S), 5. the apical angle of the triangular zone or trishear angle, and 6. the fault slip.
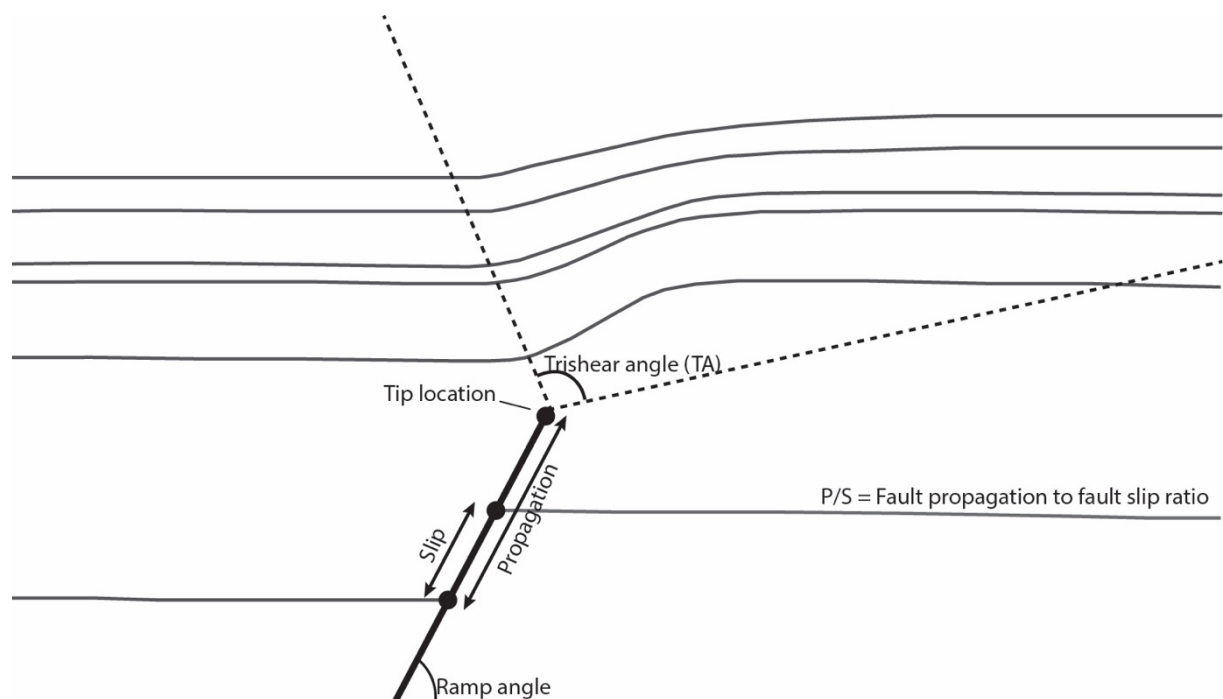
Figure 18: Parameters of the trishear model in two-dimensions.

The values of the trishear parameters that best fit the structure are not known, and as I discussed before, they cannot be determined directly from the geometry of the fold. Therefore, in order to estimate the values of these parameters, I used a trishear inversion methodology. Basically, one defines possible ranges for each one of these parameters, and searches for the combination of parameter values that best restores the folded bed to a straight line (Allmendinger, 1998). There are several ways of doing this: using brute force in a regular grid encompassing the parameter space and sampling interval (Allmendinger, 1998), using local (Cardozo & Aanonsen, 2009) or global (Cardozo et al., 2011) optimization methods, or using Markov-chain Monte Carlo methods (Oakley & Fisher, 2015). Cardozo and Oakley (2019) discuss these different methods and their implications.

In this study, I used the Markov chain Monte Carlo (MCMC) method of Oakley and Fisher (2015), although the results were also corroborated by applying the global optimization method of Cardozo et al. (2011). The MCMC method is implemented (by David Oakley) as a computer program (InvertTrishear) that executes the inversion, and Matlab scripts that allow visualizing the results. Using the MCMC algorithm, one can run the trishear inversion and determine the probability distributions for the six model parameters, and in this way the uncertainty and range of the parameter values that best fit the structure (Oakley & Fisher, 2015).

The parameters of the best fit model were used to plot the strain ellipses and lines of no finite elongation throughout the structure (Matlab script by Nestor Cardozo). The lines of no finite elongation are defined by the points where the circle representing the initial state and the finite strain ellipse intersect, meaning that the length of these lines has not changed. These lines have shear along them, and as discussed by Allmendinger (1998) and Allmendinger et al. (2004), they can be used as proxies for fracture orientations. Thus, the magnitude of strain together with the lines of no finite elongation, can be used to infer the density and orientation of possible fractures associated to the monocline.

4 Results

4.1 Lithology description

Figure 19 displays a basic lithology description based on the well log responses. The Kolmule Formation below 518 m SSTVD is represented by gamma ray (GR) values around 100 gAPI. However, at the base of the succession, a slight decrease in GR and shale volume (Vsh) is observed. The resistivities are constant, and there is an increase in density and decrease in neutron values at the base. The velocities and acoustic impedance increase towards the base. The Kolmule succession below 518 m SSTVD is interpreted to mainly consist of shale. However, at the base of this formation, the log responses could indicate a ~2 m carbonate bed.
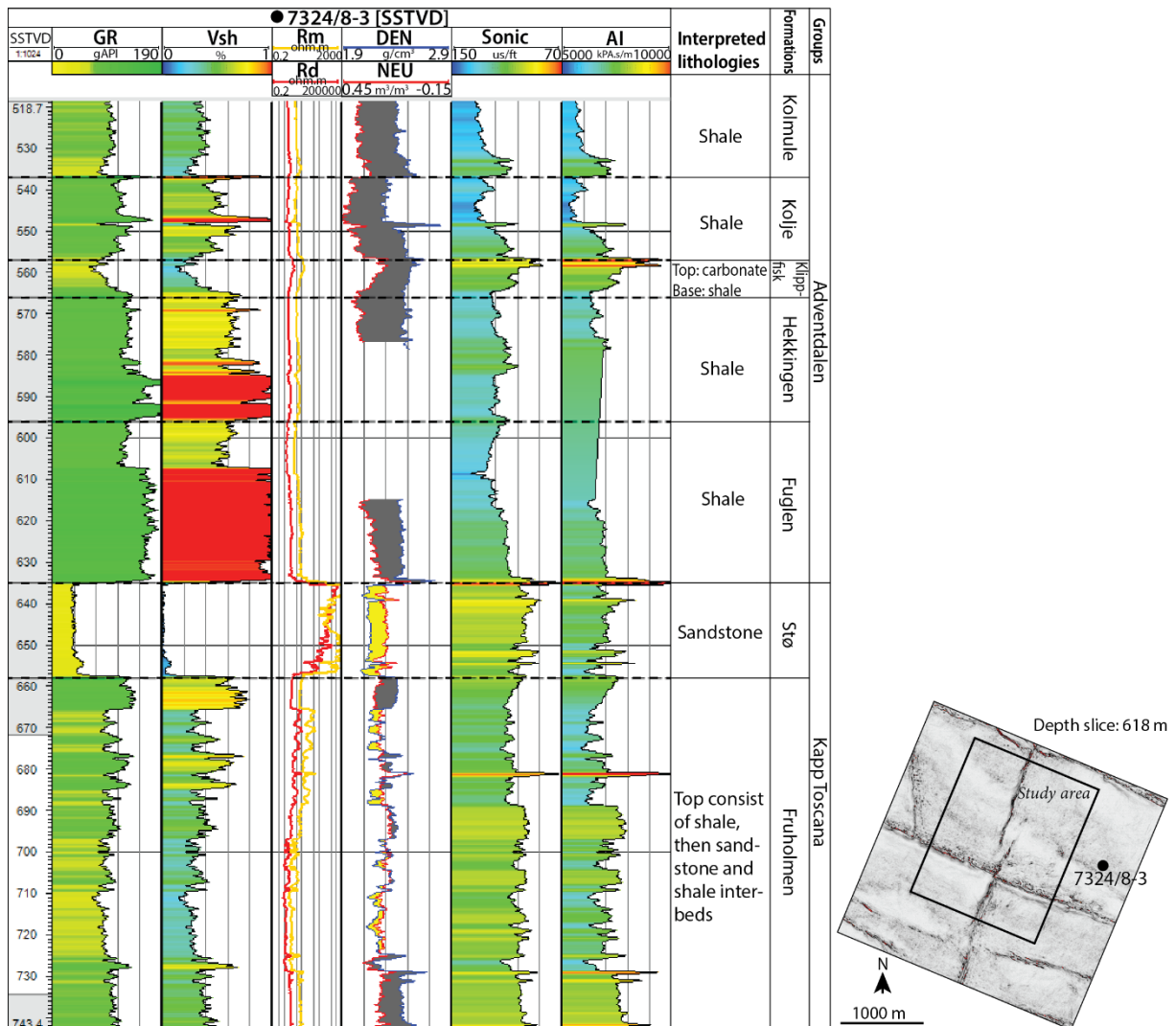
Figure 19: Basic lithology description based on gamma ray (GR), volume of shale (Vsh), medium and deep resistivity (Rm and Rd, respectively), density (DEN) and neutron (NEU) relationship, sonic (transit time) and acoustic impedance (AI). The well location is shown on the variance depth slice to the right. Notice that the NEU and sonic logs are reversed.

Generally high GR values (110–120 gAPI) are observed in the Kolje Formation. Lower GR (76 gAPI) and Vsh (0.19) are noticeable in the middle part of this succession. This thin zone of ~1 m has a prominent increase in density and decrease in neutron. Higher velocity (faster/shorter transit time) and AI are observed, while the resistivity readings remain constant. This could indicate some carbonate stringers/layers in the middle of the succession. The rest of the succession is interpreted as shale.

Lower GR (~65 gAPI) and Vsh (~0.18) values, higher density (~2.55 g/cm³) and lower neutron magnitudes (~0.2), as well as a velocity and AI increase are observed at the top and middle of the Klippfisk Formation. The GR values increase towards the base, and the other logs follow the general trend of the Kolmule and Kolje formations. The resistivity logs remain constant in this succession. Carbonates are interpreted at the top and middle of the Klippfisk Formation, while shales are more dominant at the base.

The GR (~130 gAPI) and Vsh (~0.65) values in the Hekkingen Formation are generally high, with the highest values at the lower part of the succession (160–240 gAPI and 0.95-1, respectively). The resistivity is constant, and the density and neutron logs are missing in large parts of the formation. The velocity and AI do not show any major variations, except for some increased values in the middle of the section corresponding to a decrease in GR and Vsh values. The AI log is interpolated in the zone where the density log is missing. Generally, this formation is interpreted to consist of shale.

The Fuglen Formation is represented by generally high GR (~130 gAPI) and Vsh (~0.60) values, with higher values (~165 gAPI and 0.95-1, respectively) in the middle and towards the base (similar trend as in the Hekkingen Formation). The resistivity logs are constant in this succession as well. The separation between the density and neutron logs decreases towards the base of the succession. There are no major variations in velocities and AI, except for an abrupt decrease in velocity a depth of approximately 610 m SSTVD. The Fuglen Formation is interpreted to consist mainly of shale.

At the transition between the Fuglen and Stø formations a prominent decrease in GR and Vsh is observed, corresponding to an increase in density and decrease in neutron, and an abrupt increase in velocity and AI. Thin carbonate beds or stringers could explain these log responses.

In the Stø Formation generally low GR (35-40 gAPI) and very low (or 0) Vsh values are observed. The resistivity log, in contrast to the above successions, is very high in this formation. A negative separation between the density and neutron logs is observed throughout this

formation. The Stø Formation is interpreted to mainly consist of sandstone, and the continuously low GR values imply a generally homogenous succession. The negative separation between the density and neutron logs, in addition to the high resistivity values indicate that there is hydrocarbon present in the sandstones of this formation.

The Fruholmen Formation is represented by a varying response in the well logs. The top of the formation down to 666 m SSTVD has generally high GR (~135 gAPI) and Vsh (~0.7) values. The resistivity logs show the same constant and low values as for the Kolmule, Kolje, Klippfisk and Fuglen formations. There is a positive separation in the density and neutron logs. Between 666 m and 730 m SSTVD the logs show larger variance. The GR values vary from 69 to 140 gAPI. Locally, the resistivity is higher while the density and neutron logs have negative separation. Below the depth of 730 m SSTVD, the GR and Vsh readings are again generally high ~100 gAPI, the resistivities are the same as the above shaly formations, and the density and neutron show a positive separation, like at the top of the formation.

The Fruholmen Formation is interpreted to consist mainly of shale at the very top of the formation down to 666 m SSTVD. Below the logs indicate shale and sand interbeds to a depth of approximately 730 m SSTVD, followed again by a shalier package. The local negative separation between the density and neutron logs and the corresponding increase in resistivity values, suggest that the sandstone layers/interbeds are hydrocarbon bearing.

The other well (7324/7-3S) which was available in this study did not have sufficient data to complete a lithology description throughout the entire well. It only contained GR of the Fruholmen Formation. However, the neutron and density logs were available and indicated that the Stø and Fruholmen formations are hydrocarbon bearing.

4.2   Geometrical description

4.2.1   Seismic sections

Nine seismic sections in the study area are displayed in Figure 20. The location of these sections is shown on a variance depth slice. On the depth slice, three main faults are observed in the study area (Figure 20A). Faults 1 and 2 are NNE–SSW and dip towards the W (Figure 20A–G). Fault 3 is almost perpendicular to faults 1 and 2 and dips towards the S (Figure 20H & I). Notice the fault shadow effect in the footwalls of these faults.

Fault 2 cuts all interpreted horizons and terminate in the Kolmule succession below the Upper Regional Unconformity (URU, Figure 20A & B). The fault is observed to lose displacement and eventually terminate towards the NE (Figure 20C & D). Fault 1 begins where the throw of fault 2 approaches zero, and its displacement increases towards the NE (Figure 20B–G). The structure between faults 1 and 2 is a relay ramp (Figure 20B & C).

Fault 1 underlies the studied monocline. The Kolje, Klippfisk, Hekkingen and Fuglen tops are folded above fault 1, while the Stø and intra-Fruholmen formations are faulted. The folded horizons have a steeper forelimb in the NE part of the study area, and in the northernmost section all horizons are offset by fault 1 (Figure 20G). This fault terminates in the Kolmule succession below the URU.

Figure 20H & I display fault 3 and some other faults outside the study area with the same ESE-WNW orientation. Fault 3 breaches the interpreted horizons and terminates in the Kolmule succession.

Polygonal faults are observed in the Kolmule succession on all the seismic sections. The majority of these faults terminate below the URU. However, in some sections, the URU reflector is chaotic, and it is not clear if some of the polygonal faults offset this unconformity (Figure 20). Also, fault 3 terminates very close to the URU in Figure 20H.
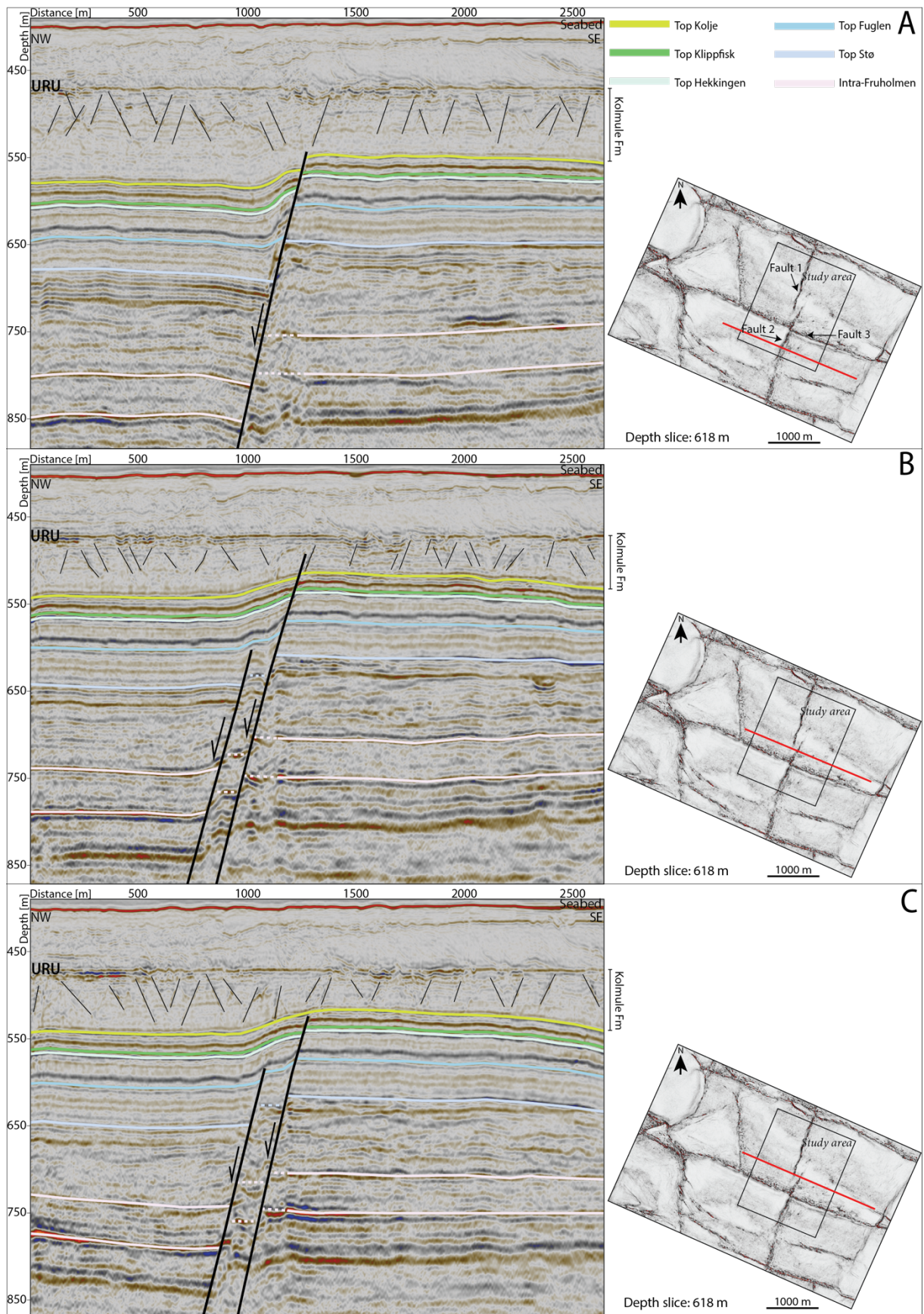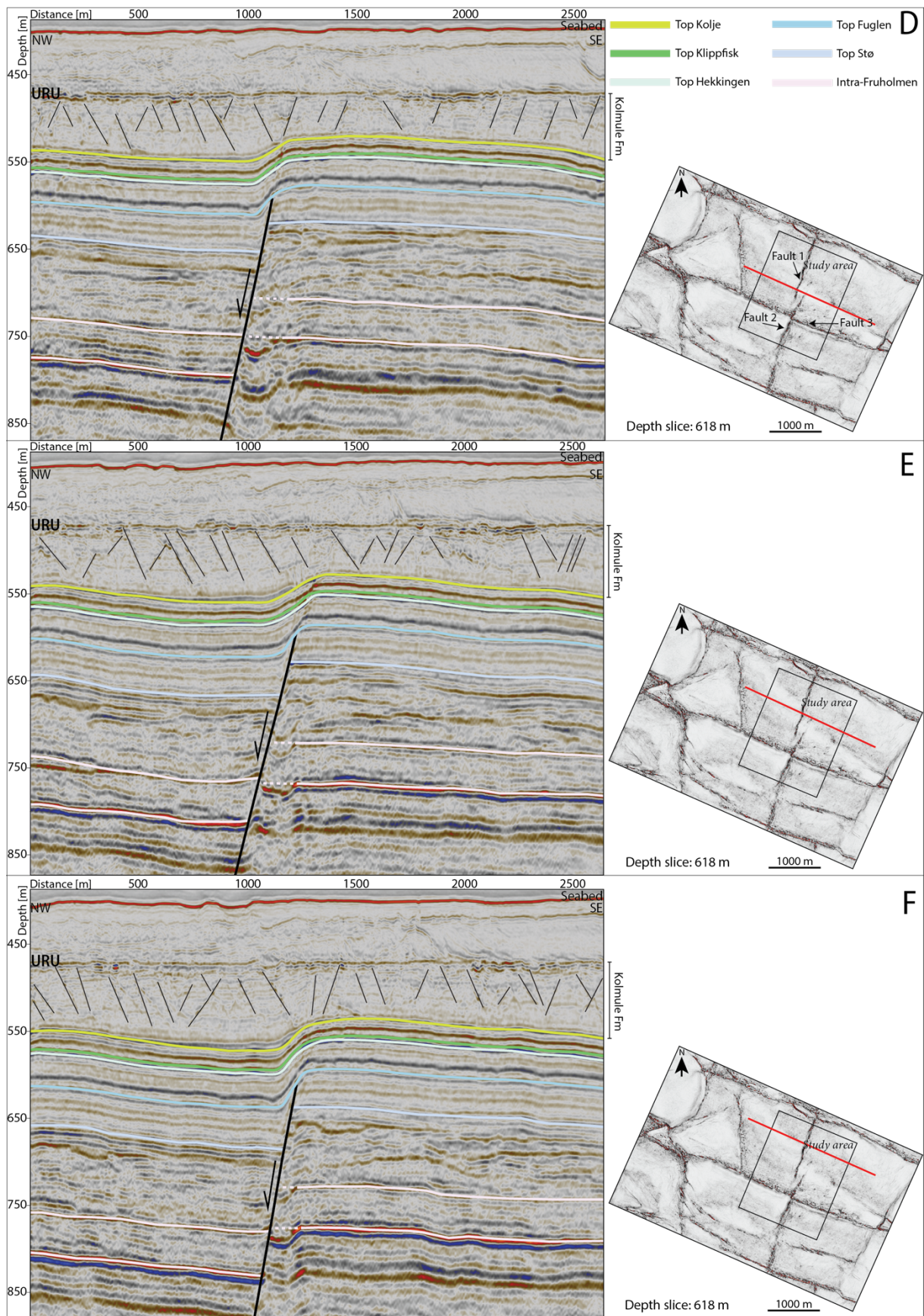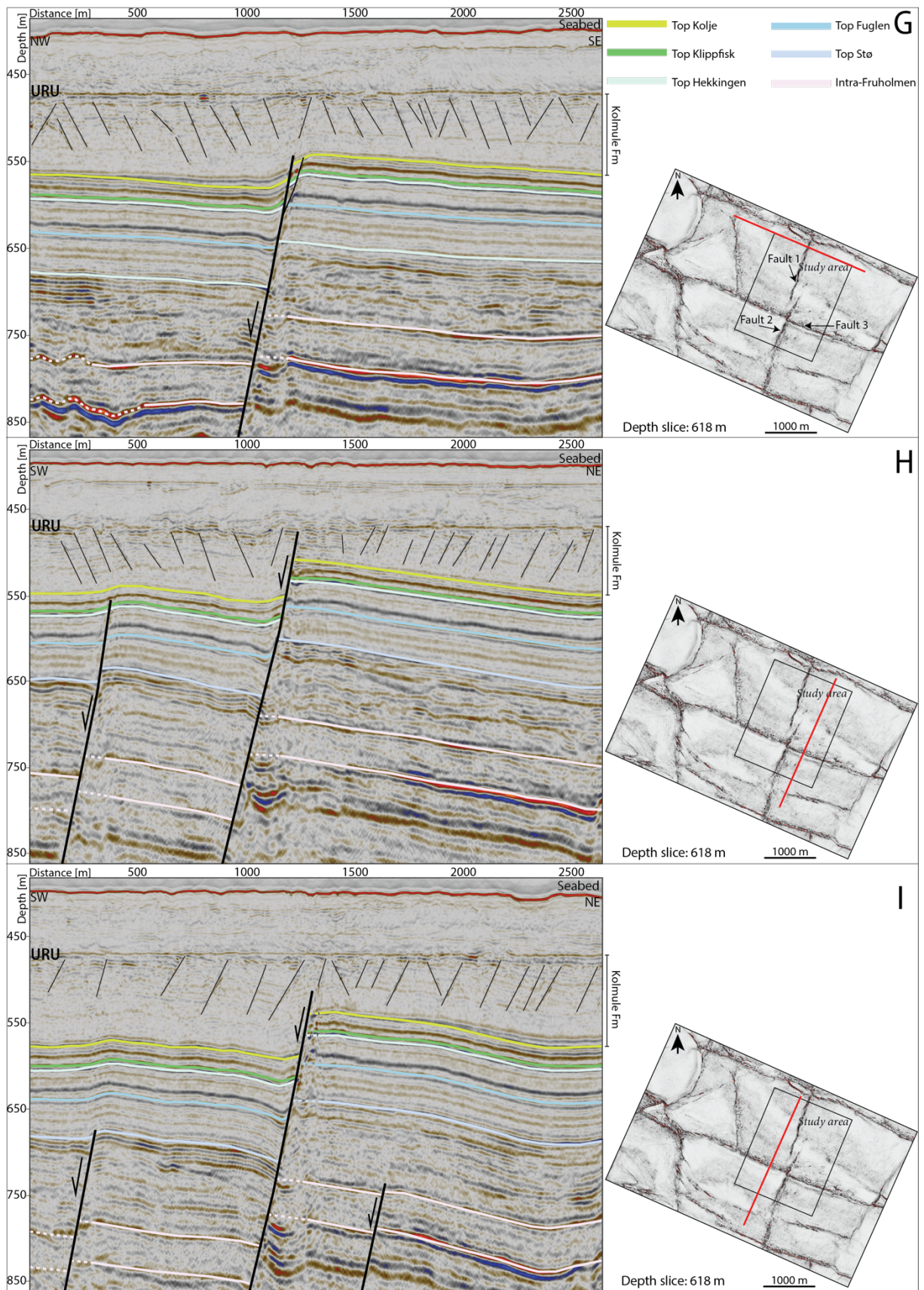
Figure 20: *(A)–(I) Seismic sections at different locations in the study area. The variance depth slice indicates the location of the sections. The faults are labeled 1, 2 and 3 (see slices in A, D & G). Fault 1 is below the studied monocline. Dashed lines are uncertain yet reasonable interpretations in low signal to noise areas (e.g., fault shadows). VE = 4.0.*

In general, there are no significant thickness variations across the faults in the interpreted successions. However, a minor increase in thickness is observed in the Hekkingen Formation, in the hanging wall close to fault 3 (Figure 20H & I). Nonetheless, the most significant thickness variations are in the Kolmule Formation, where faults 1, 2 and 3 terminate.

4.2.2 Structure maps

Structure maps of the top Kolje, Klippfisk, Fuglen and Stø horizons are displayed on Figure 21. The observations on the seismic sections in Figure 20 are confirmed by the structure maps: (1) the displacement of fault 1 increases towards the NE where it offsets the Kolje, Klippfisk and Fuglen tops (Figure 21A–C), and (2) the displacement of fault 2 decreases towards the NE and is transferred to fault 1 in the relay area. These observations are especially clear on the structure map of the top Stø, where one can observe the relay zone (Figure 21D).

The structure maps also show that the upper horizons are folded (top Kolje, Klippfisk and Fuglen surfaces), while the lower horizons (below top Stø surface) are faulted. The folded surfaces display a monoclinal structure. The contours on the folded surfaces indicate a steeper forelimb of the monocline towards the NE.
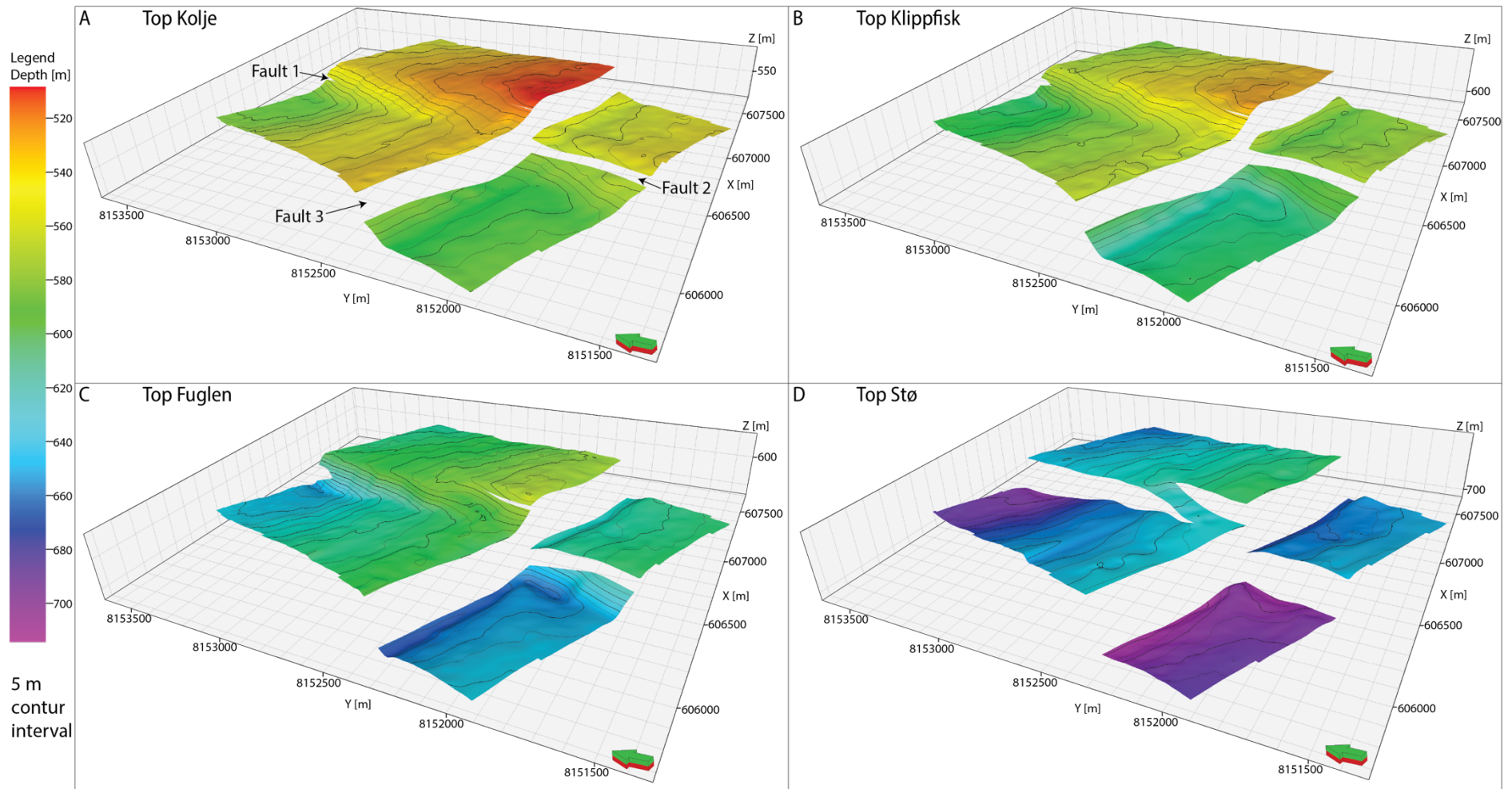
Figure 21: *Structure maps of the Kolje, Klippfisk, Fuglen and Stø tops. Green arrow indicates north. VE = 3.0.*

4.2.3 Fault throw distribution

Figure 22A displays the hanging wall (HW) and footwall (FW) intersections (cutoffs) of the horizons with fault 1. Based on these cutoffs, the throw of fault 1 varies from 0 m to ~62 m (Figure 22B). In the southernmost part of the fault, the HW and FW cutoffs from the top Kolje to the intra-Fruholmen 2 horizons merge. This is the 0 m throw or southern tipline of the fault. Towards the NE, the separation of the HW and FW cutoffs and throw increases in the lower three horizons: top Stø, intra-Fruholmen 1 and intra-Fruholmen 2. However, the upper three horizons, which are folded, do not show a separation of the HW and FW cutoffs until the northernmost part of the fault, where the fault breaches the monocline (Fig. 21A). Generally, the throw on fault 1 increases from SW to NE and with depth.
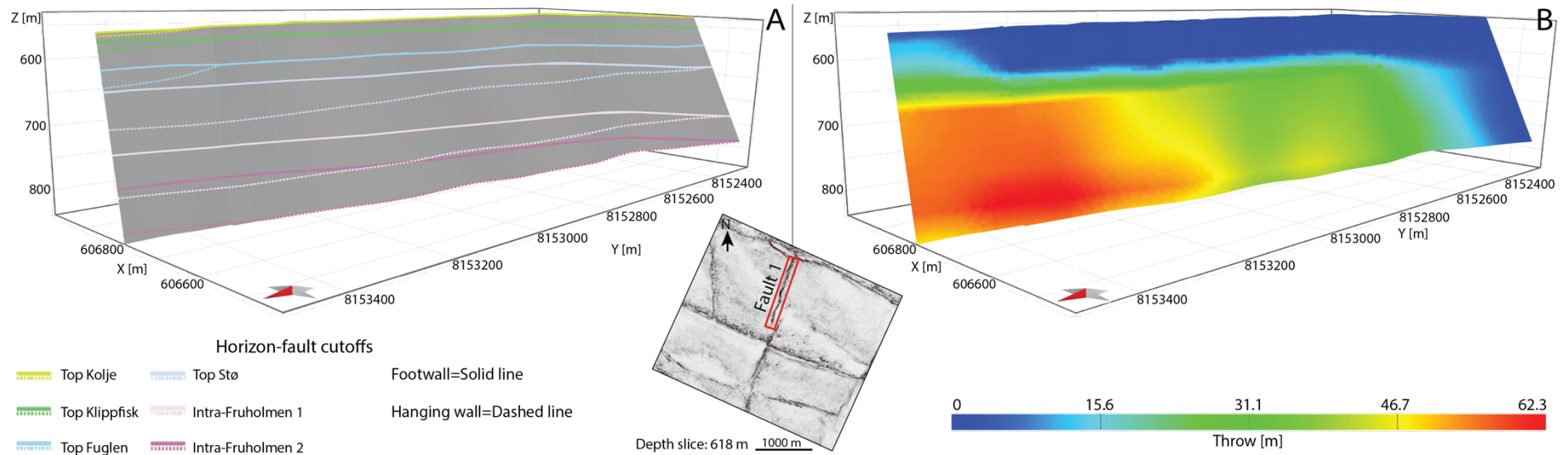
Figure 22: (A) Hanging wall (dashed) and footwall (continuous) cutoffs along fault 1. (B) Colored fault throw computed from the cutoffs. Red arrow in A and B indicates north. Red rectangle in variance depth slice shows the area of analysis.

The HW and FW cutoffs along faults 1 and 2 are displayed on Figure 23A. The throw of these faults varies from 0 m to ~67 m (Figure 23B). Fault 2 decreases in throw towards the NE, while fault 1 decreases in throw towards the SW. In the NE part of fault 2, the HW and FW cutoffs from the top Kolje to the intra-Fruholmen 2 horizons merge. This implies 0 m throw and the northern tipline of fault 2. Towards the SW, the separation of the HW and FW cutoffs along fault 2 increases. This occurs first in the lower three horizons: top Stø, intra-Fruholmen 1 and intra-Fruholmen 2; and farther south in the upper three horizons: top Kolje, Klippfisk and Fuglen. The highest throw of fault 2 (~67m) is in the SW. The throw of fault 2 also increases with depth. The area of overlap of faults 1 and 2 is a relay structure.
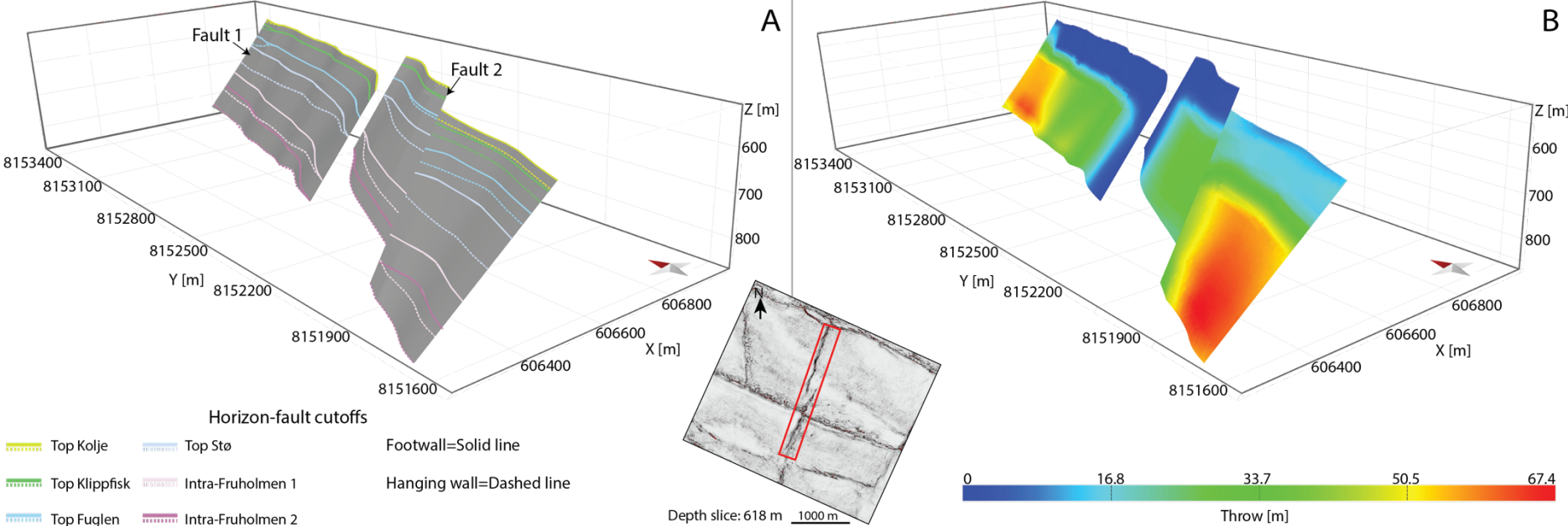
Figure 23: (A) Hanging wall (dashed) and footwall (continuous) cutoffs along faults 1 and 2. (B) Colored fault throw computed from the cutoffs. Red arrow in A and B indicates north. Red rectangle in variance depth slice shows the area of analysis.

The throw distribution of the three main faults in the study area is displayed on Figure 24. The throw magnitudes vary from 0 to 87 m. The largest throw is observed in the westernmost part of fault 3. The throw along fault 3 decreases from W to E. From the analysis, it is also clear that fault 3 offsets fault 2.
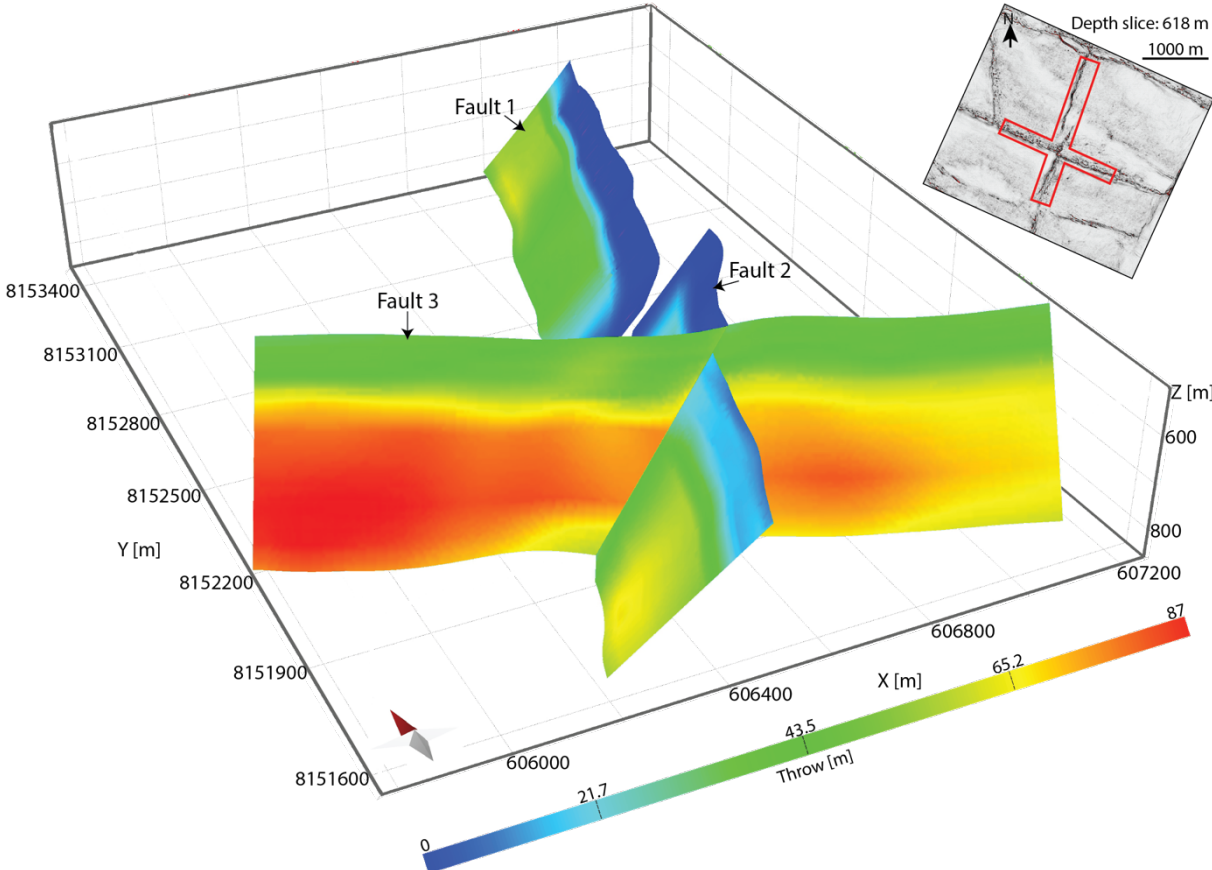
Figure 24: Colored fault throw of the three main faults in the study area. Throw values are based on the HW and FW cutoffs on these faults (not showed). Red arrow indicates north. Red polygon in variance depth slice shows the area of analysis.

4.2.4 Curvature of the folded horizons

4.2.4.1 Fold hinge and crest

Figure 25 displays the maximum curvature of the folded top Fuglen surface, with the anticlinal hinge- and crest line drawn. The hinge line represents the line of maximum curvature, while the crest line represents the structural high of the fold. These two lines are sub-parallel, but they do not coincide. Thus, the fold is non-symmetrical. The deviation between the lines is greatest in the southern part, while the two lines approach each other towards the north. Thus, the asymmetry of monocline is larger in the southern part.
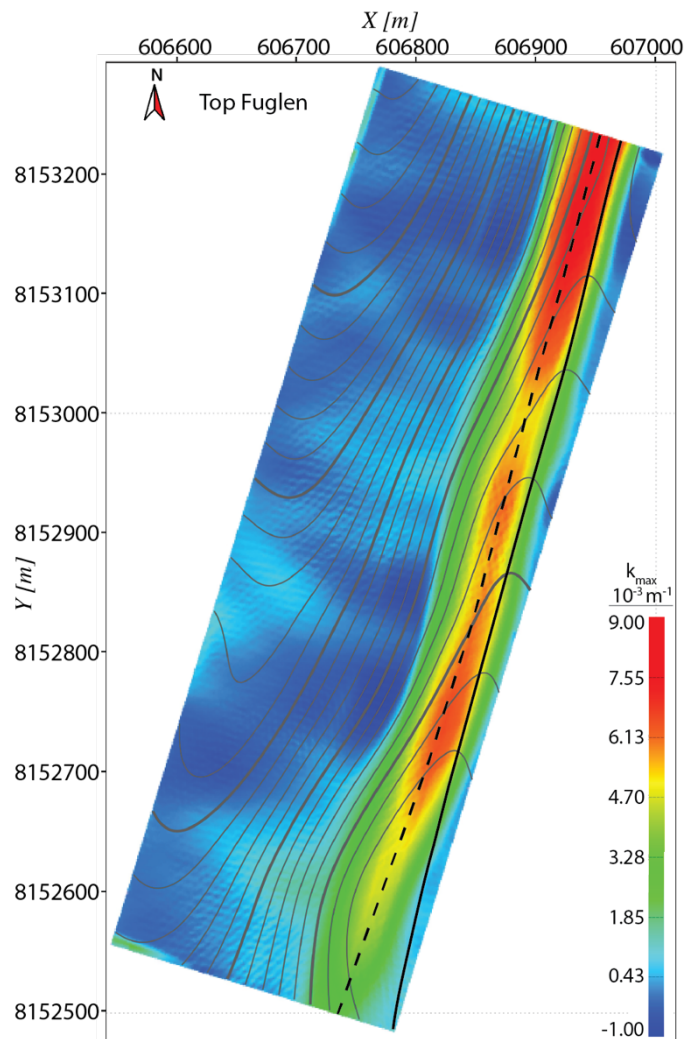
Figure 25: *Maximum curvature of the folded top Fuglen surface. Dashed line is the fold hinge, while solid line is the fold crest. Contours are elevation, CI = 2.5 m.*

4.2.4.2 Top Fuglen surface

Figure 26A displays the maximum curvature value (colors) and directions (black tics) of the monocline on the top Fuglen surface. High values of k_{max} (red) are located along the anticlinal hinge area. The k_{max} directions in this area are oriented approximately perpendicular to the hinge line. In the forelimb, the k_{max} values are positive and negative. In these areas, the orientation of k_{max} also varies. These variations are due to local undulations in the surface. In the synclinal area, negative or low k_{max} parallel to the fold hinge is observed.

The k_{min} values and directions on the top Fuglen surface are displayed on Figure 26B. High values of negative curvature (blue) are present in the synclinal area. The k_{min} direction in this area is approximately perpendicular to the hinge line, which is the line connecting points of maximum negative k_{min}. In the anticlinal area, the orientations of k_{min} are sub-parallel to the hinge line.

4.2.4.3 Top Klippfisk surface

Figure 27A displays the k_{max} values and directions on the folded top Klippfisk surface. High positive values are observed in the anticlinal area, particularly in the NE-part. In the forelimb, the k_{max} values and directions vary. This is due to local undulations, like those observed in the top Fuglen surface. Negative and low values of k_{max} are observed at the base of the forelimb and in the synclinal area. The directions of k_{max} in the anticlinal area are perpendicular to the hinge line, while they are parallel to the hinge line in the forelimb and synclinal areas.

The values and directions of k_{min} on the top Klippfisk surface are displayed on Figure 27B. The most negative k_{min} values are in the synclinal area, particularly in the NE-part. The k_{min} directions are parallel to the hinge line in the anticlinal area, and they are perpendicular to the hinge line in the synclinal area.
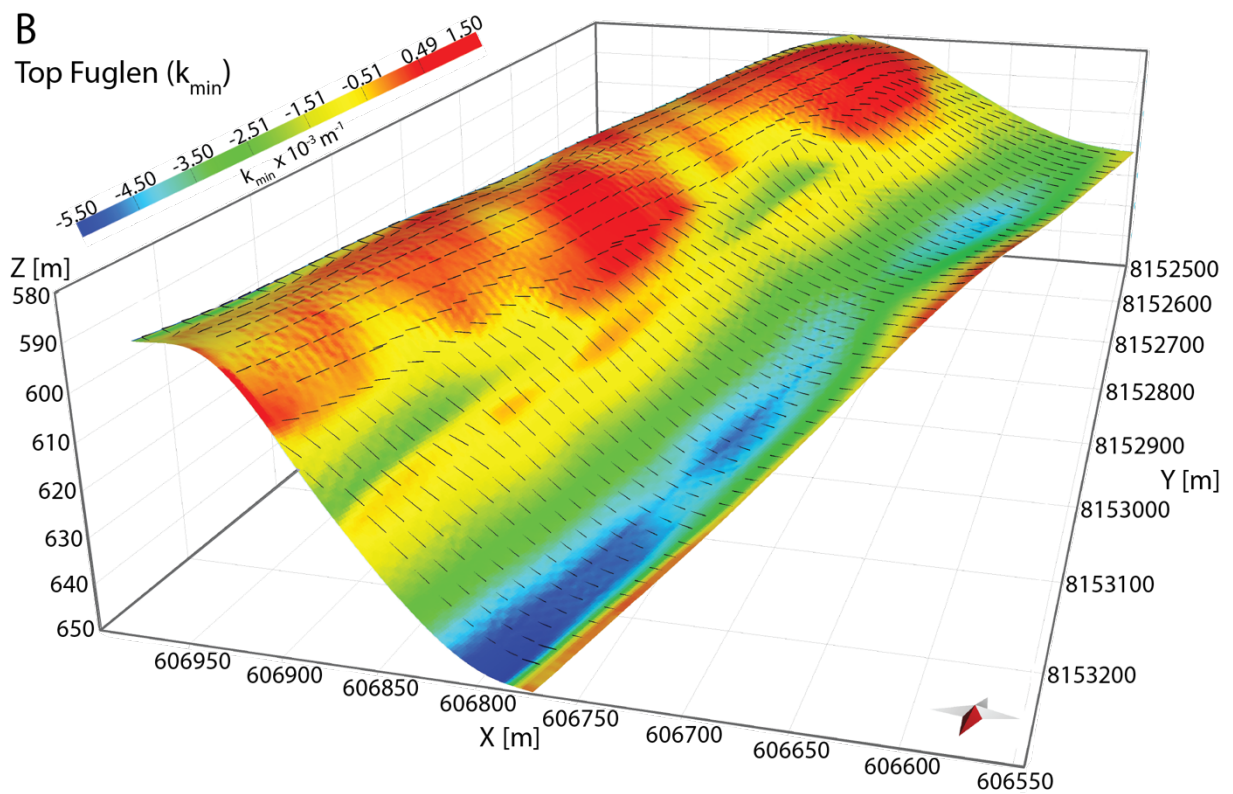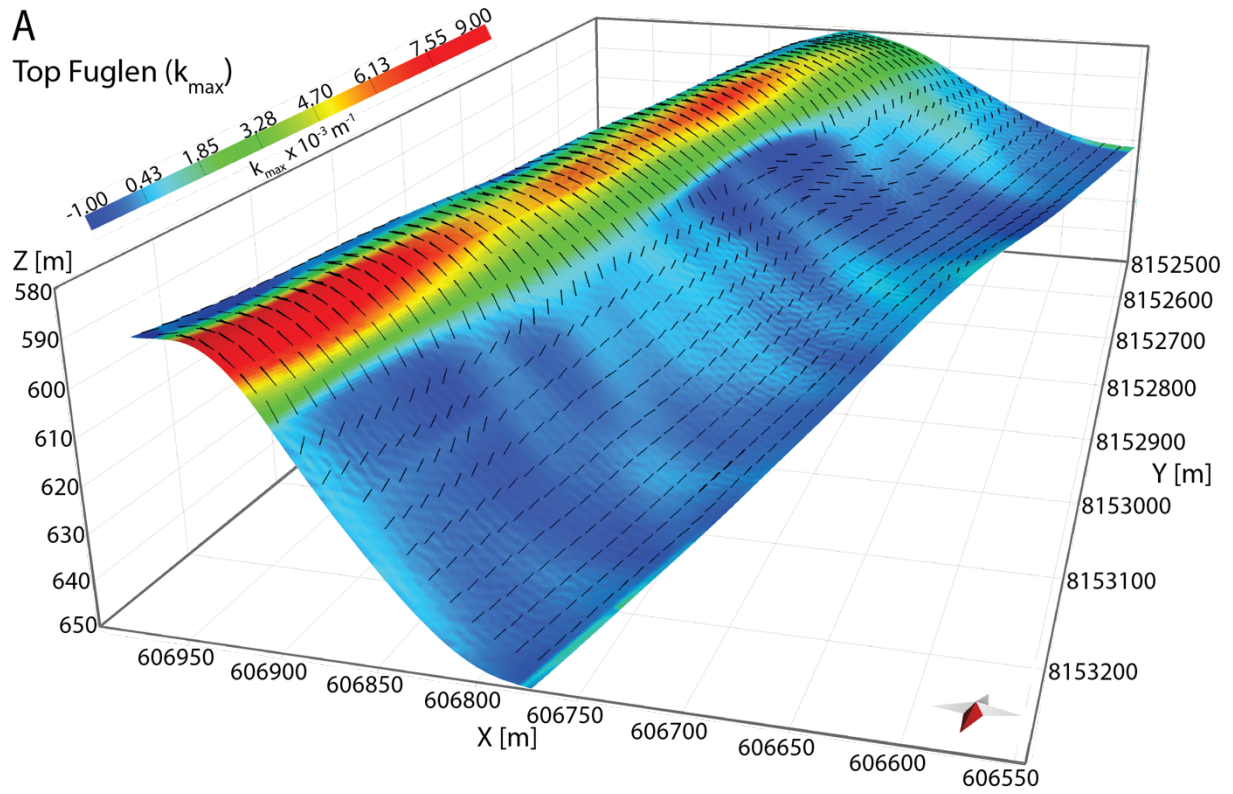
Figure 26: *Principal curvature values (colors) and directions (black tics) of the monocline on the top Fuglen surface. A) k_{max}, B) k_{min}. Red arrow indicates north.*
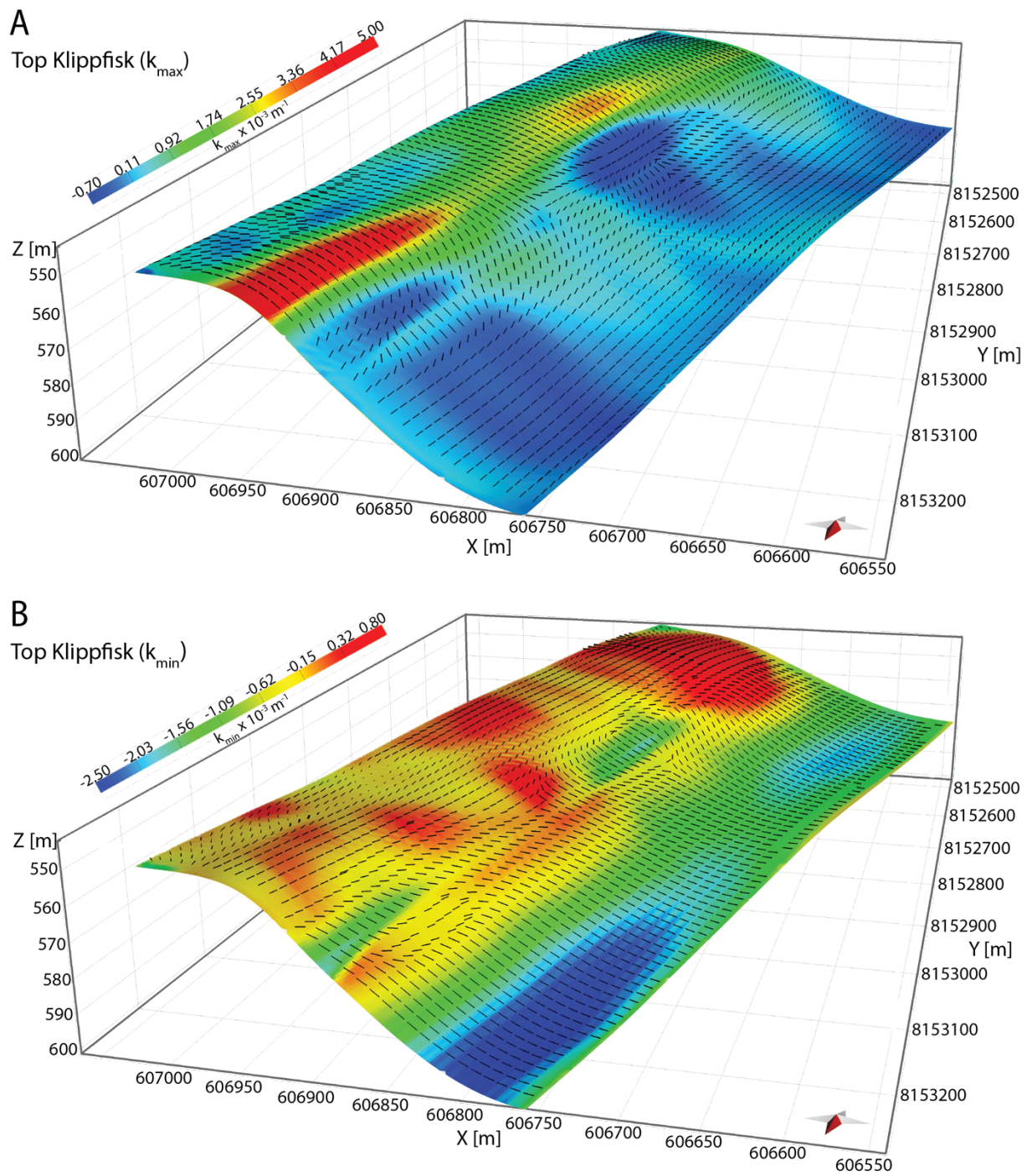
Figure 27: Principal curvature values (colors) and directions (black tics) of the monocline on the top Klippfisk surface. A) k_{max}, B) k_{min}. Red arrow indicates north.

4.2.4.4 Top Kolje surface

Figure 28A display the k_{max} values and directions on the folded top Kolje surface, which is the uppermost interpreted horizon. The previous observations for k_{max} on the top Fuglen and top Klippfisk surfaces are also applicable in this case: higher values of positive curvature in the anticlinal hinge, and the k_{max} directions in this area sub-perpendicular to the hinge line. Also, the k_{max} directions in the forelimb and in the synclinal area are sub-parallel to the hinge line. However, there are some variations in the k_{max} directions and values in the forelimb and in the synclinal area, which are believed to represent undulations in the surface.

Likewise, the observations for k_{min} on the top Fuglen and top Klippfisk are also valid on the top Kolje surface (Figure 28B). The most negative values of k_{min} are mainly located in the synclinal area where the k_{min} directions are perpendicular to the hinge line. In the anticlinal area, the orientations of k_{min} are approximately parallel to the hinge line.

In summary, in the Fuglen, Klippfisk and Kolje tops, the k_{max} directions in the anticlinal (positive curvature) area are approximately perpendicular to the hinge line, while the k_{min} directions are parallel. Contrarily in the synclinal (negative curvature) area, k_{max} directions are parallel while k_{min} directions are perpendicular to the hinge line. These observations suggest that the anticlinal and synclinal areas, and the monocline in general is approximately cylindrical. However, the principal curvatures with orientations parallel to the anticlinal and synclinal hinge lines are not zero, and overall the curvature of the monocline increases to the NE. These observations together with the presence of local surface undulations suggest that the monocline is not completely cylindrical.
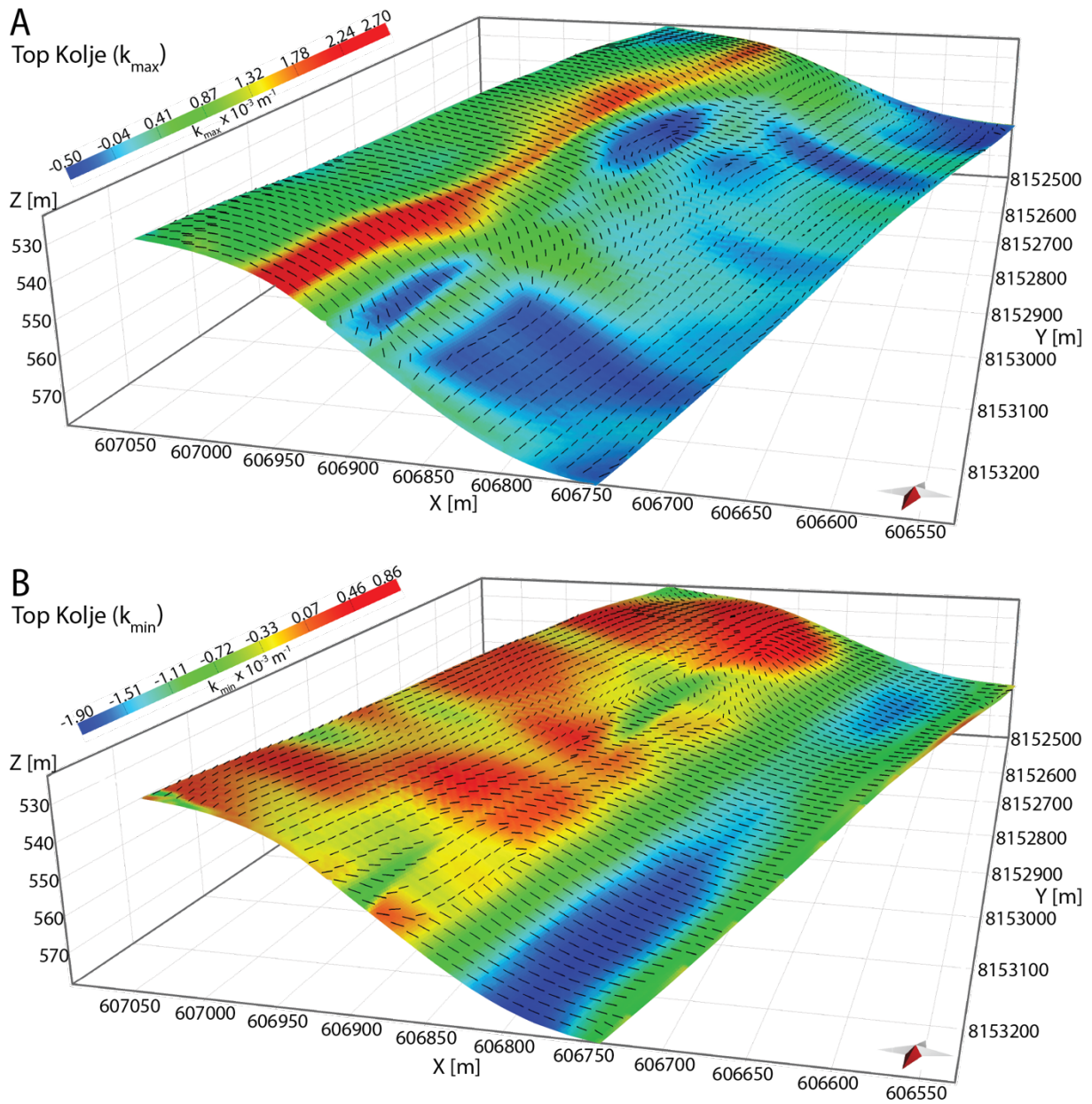
Figure 28: Principal curvature values (colors) and directions (black tics) of the monocline on the top Kolje surface. A) k_{max}, B) k_{min}. Red arrow indicates north.

4.2.4.5 Curvature filter

Gaussian curvature (k_G) and mean curvature (k_M) are based on the two principal curvatures (Eqs. 4 and 5). A combination of k_G and k_M on the surfaces can highlight local geometries (Figure 17). This makes possible to determine whether the fold has a cylindrical shape or how far it deviates from this idealized shape. Figure 29A–D display the combined k_G and k_M on the top Fuglen surface. The surface is represented by colors which define specific local shapes (Figure 29E). Notice that for a surface to be characterized as cylindrical, $k_G = 0$, and $k_M \neq 0$.

The unfiltered k_G-k_M curvature on the top Fuglen surface is displayed on Figure 29A. The anticlinal area consists mainly of antiformal saddles and domes, with some cylindrical antiformal shapes in between. The synclinal area mainly contains synformal saddles and basins, with some cylindrical synformal shapes in between. Additionally, in the transition between the synformal- and antiformal saddle shapes, small planar areas are observed. Based on these observations, the combined k_G and k_M indicate that the surface is not cylindrical. Thus, in general, none of the principal curvatures equals 0.

By defining an absolute threshold value, k_t, and removing principal curvatures below this value, one can determine how large the threshold value needs to be for the fold to display a cylindrical shape. When principal curvatures magnitudes lower than 1.0×10^{-4} m^{-1} (k_t) are set to 0, the non-cylindrical areas in the anticline and syncline are reduced, and more areas of cylindrical shape emerge (Figure 29B). Some of the planar areas, which were in the transition between the synformal and antiformal saddles, are replaced by perfect saddle areas.

By increasing k_t to 5.0×10^{-4} m^{-1}, the dominant shape in both the anticlinal and synclinal areas is cylindrical antiform and synform, respectively (Figure 29C). Additionally, more areas are classified as planar between the cylindrical shapes. Thus, most areas on the filtered top Fuglen surface have one of the principal curvatures equal to 0. Where the planar shapes are present, both principal curvatures equal 0. Still, smaller local areas are observed as non-cylindrical, but generally the filtered geometry of the surface is cylindrical.

The smaller non-cylindrical areas are removed by using a k_t of 9.0×10^{-4} m^{-1}, although in the SW part of the monocline there are still some non-cylindrical dome areas (Figure 29D). The surface consists of a continuous antiformal shape in the anticlinal area and a continuous synformal shape in the synclinal area, separated by larger planar areas. In the SW and NE parts of the forelimb, two synformal areas surrounded by planar areas are observed. Interestingly, the SW and NE areas are separated by a simpler transition from synform to planar to antiform areas in the central part of the monocline. This may indicate that the monocline is divided into three different domains along strike, a SW, central and NE domain.
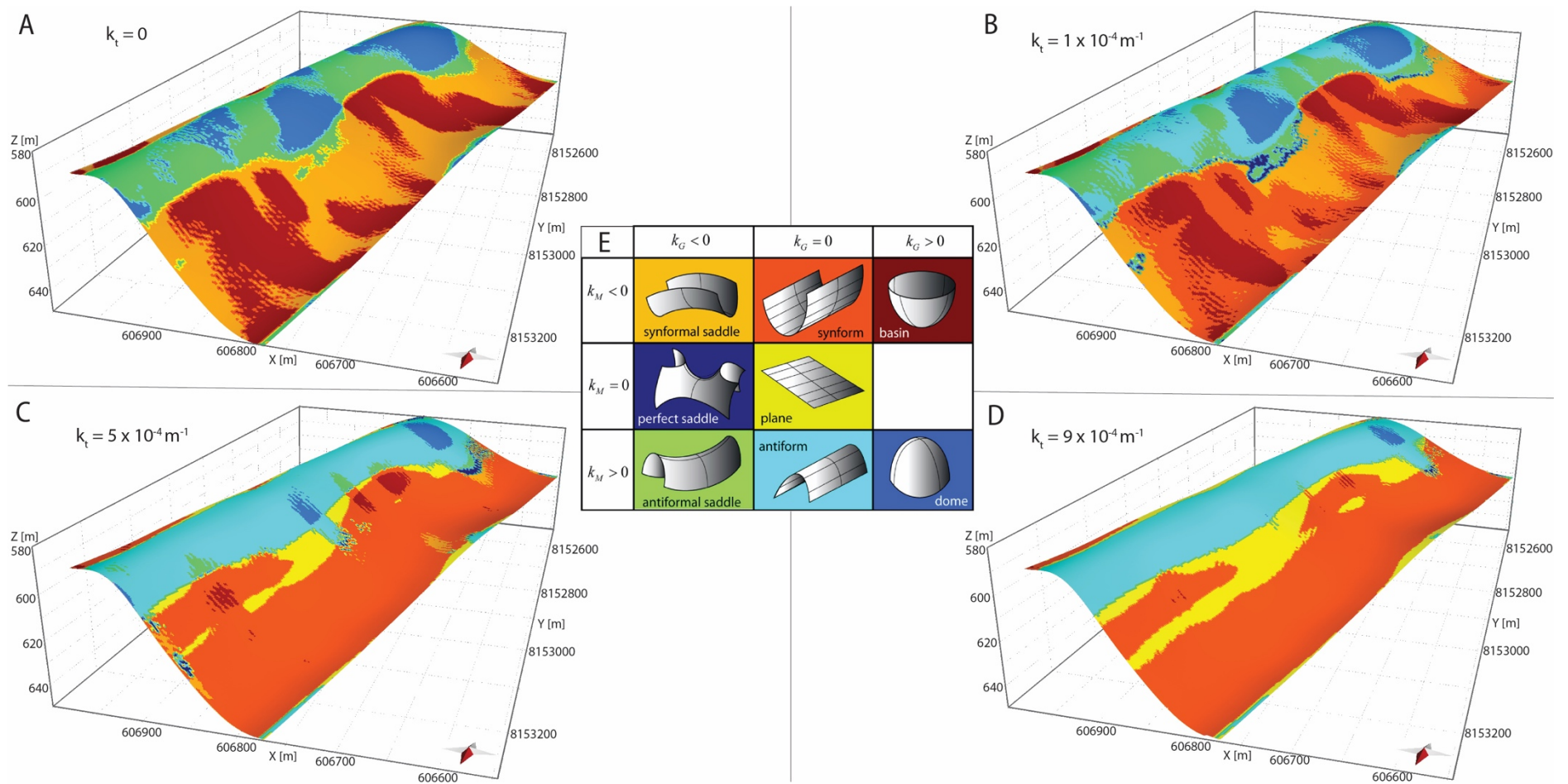
Figure 29: *k_G-k_M curvature of the top Fuglen surface. A)–D) are surfaces filtered with increasing threshold value k_t. Colors correspond to surface shapes as illustrated in E) (from Mynatt et al., 2007). Red arrow indicates north.*

4.3 Trishear modelling

4.3.1 Inversion

Sections D, E, F and G in Figure 20 were modelled using the InvertTrishear program (by David Oakley). These sections are perpendicular to the fold axis and are to the north of the relay structure. For practical purposes, these sections are renamed as 1 (D), 2 (E), 3 (F) and 4 (G). Section 1 is closest to the relay structure to the south, and section 4 is the northernmost one (Figure 20). The interpretation of section 4 is simplified to only cover the main fault (Figure 20G).

The minimum and maximum values of the six trishear parameters in the seismic sections are included in Table 1. These values are specified by the user according to the interpretation and knowledge of the section. The uncertainty or error of the data (σ) is also included as a model parameter, which is updated along with the trishear parameters to find the value that best fits the data. The program searches within the specified parameter ranges for the models with high probability. At each step of the Markov chain modelling, the chain moves from one set of parameter values to a new set of parameter values. The distance the chain moves for each parameter is randomly chosen from a normal distribution. The third entry in each range in Table 1 called "step" is the standard deviation of this normal distribution, and it controls the step size taken by the Markov chain. However, the program modifies the step sizes for each parameter to get a high acceptance rate of the proposed moves.

The allowed parameter ranges are constrained by the input minimum and maximum values. Some parameters are more constrained by the seismic interpretation, especially the fault dip, location of the current fault tip, and fault slip, which is well constrained by the interpretation of the lower non-folded horizons. The fault propagation to fault slip ratio (P/S), trishear angle (TA), and the initial depth of the fault tip are less well known, and they can be determined by the trishear inversion. All the interpreted, top Kolje to intra-Fruholmen 2, horizons were used in the inversion. In other words, the program search for the models that best fit all the interpreted horizons in the section.

Table 1: Parameter ranges for the horizontal (x) and vertical (y) coordinates of the current fault tip, fault slip, fault dip, trishear angle (TA) and fault propagation to slip ratio (P/S). The data uncertainty (σ) is also included.

	Parameters [min value, max value, step]						
	x (m)	y (m)	Fault slip (m)	Fault dip (°)	TA (°)	P/S	σ (m)
1	[699.4, 719.4, 2]	[385.3, 405.3, 2]	[24, 64, 10]	[46, 56, 1]	[30, 100, 10]	[2, 3, 0.5]	[0, 10, 2]
2	[671.3, 691.3, 2]	[308.7, 328.7, 2]	[29, 69, 10]	[46, 56, 1]	[30, 100, 10]	[2, 3, 0.5]	[0, 10, 2]
3	[636.9, 656.9, 2]	[398.8, 418.8, 2]	[44, 84, 10]	[53, 63, 1]	[30, 100, 10]	[2, 3, 0.5]	[0, 10, 2]
4	[646.3, 666.3, 2]	[350.5, 370.5, 2]	[49, 89, 10]	[52, 62, 1]	[30, 100, 10]	[2, 3, 0.5]	[0, 10, 2]

A total of 100,000 iterations were used in the search, but only every 10th iteration was saved. The MCMC algorithm starts exploring the parameter space from a random value within the specified parameter ranges. Convergence of the search is reached within the first 10,000 iterations (Figure 30). These first 10,000 iterations or models are not considered in the output, but just the next 90,000.
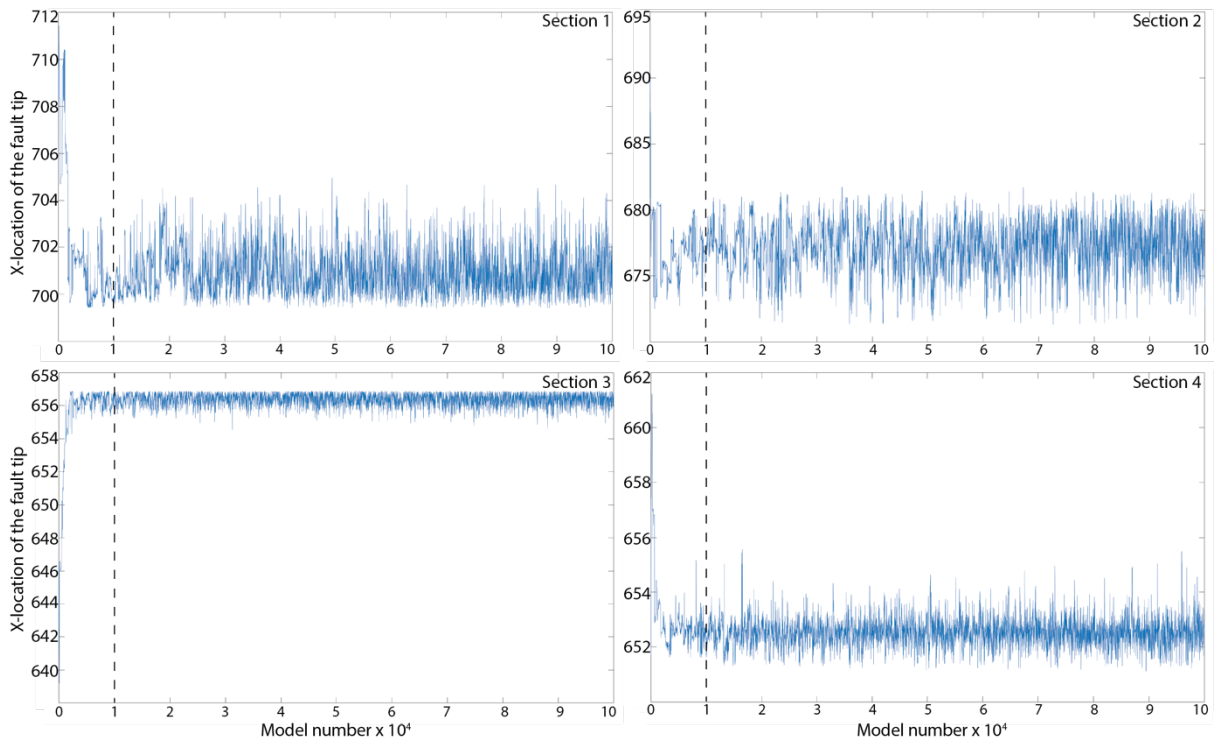
Figure 30: Path taken by the MCMC algorithm for the x-location of the fault tip. The search converges within the first 10,000 iterations (dashed line). These first 10,000 iterations are not considered in the output.

The best-fit model, and histograms of model parameters for each section are included in Figure 31. The parameter values that define the best-fit model are indicated by the highest frequencies of the histograms. These values are displayed on Figure 31, and in Table 2. In the southernmost section 1, the best trishear model (blue) fits the interpretation (red) well (Figure 31A). The model captures the folding of the upper horizons. One clear deviation, however, is that the model displays folding of the top Stø horizon in the hanging wall, when this horizon is clearly not folded in the seismic section. The initial location of the fault tip is right above the intra-Fruholmen 1 footwall cutoff, while the current fault tip is just below the top Fuglen horizon. The best-fit model predicts fault slip ~48 m, fault dip ~55°, TA ~87° and P/S ~2.7. The uncertainty (σ) between the best-fit model and the interpretation is ~1.4 m (Figure 31A).

In section 2, the best trishear model also fits the interpretation well and captures the folding of the upper horizons (Figure 31B). However, the model fit is not as good as in section 1. There are misfits in the forelimb area, especially at the intra-Hekkingen level, and in the synclinal area, especially in the uppermost three horizons top Klippfisk to top Kolje. In addition, folding of the top Stø in the hanging wall, which is not observed in the seismic section, is displayed in the model. Broad synclinal folding of the intra-Fruholmen 1 and 2 horizons in the hanging wall, which is observed in the section, is not captured by the model. The histograms for fault dip and P/S in section 2 are narrow, and the maximum frequency is located at the maximum value defined in the range, which is not ideal (Figure 31B). The initial location of the fault tip is right below the intra-Fruholmen 1 footwall cutoff, while the current fault tip is just above the top Fuglen horizon. This is still consistent with the trishear model for section 1. The best-fit model has fault slip ~53 m, fault dip ~56°, TA ~74° and P/S ~2.99. The σ is ~2.2 m.
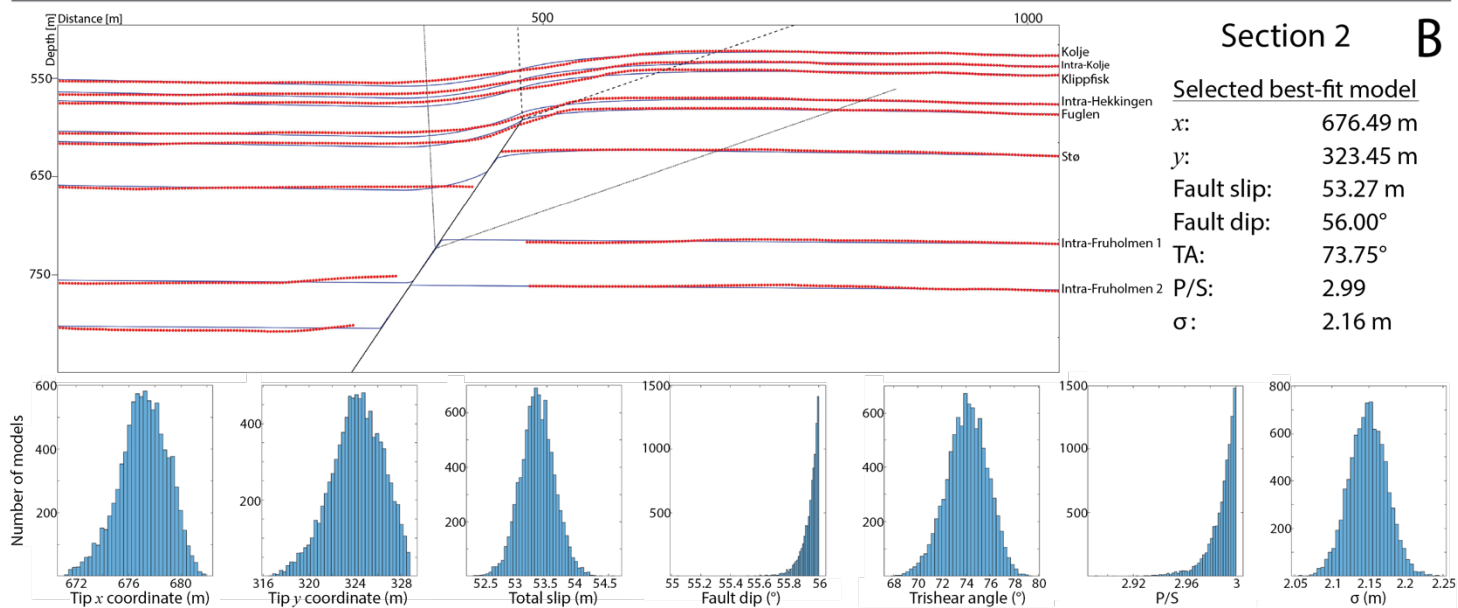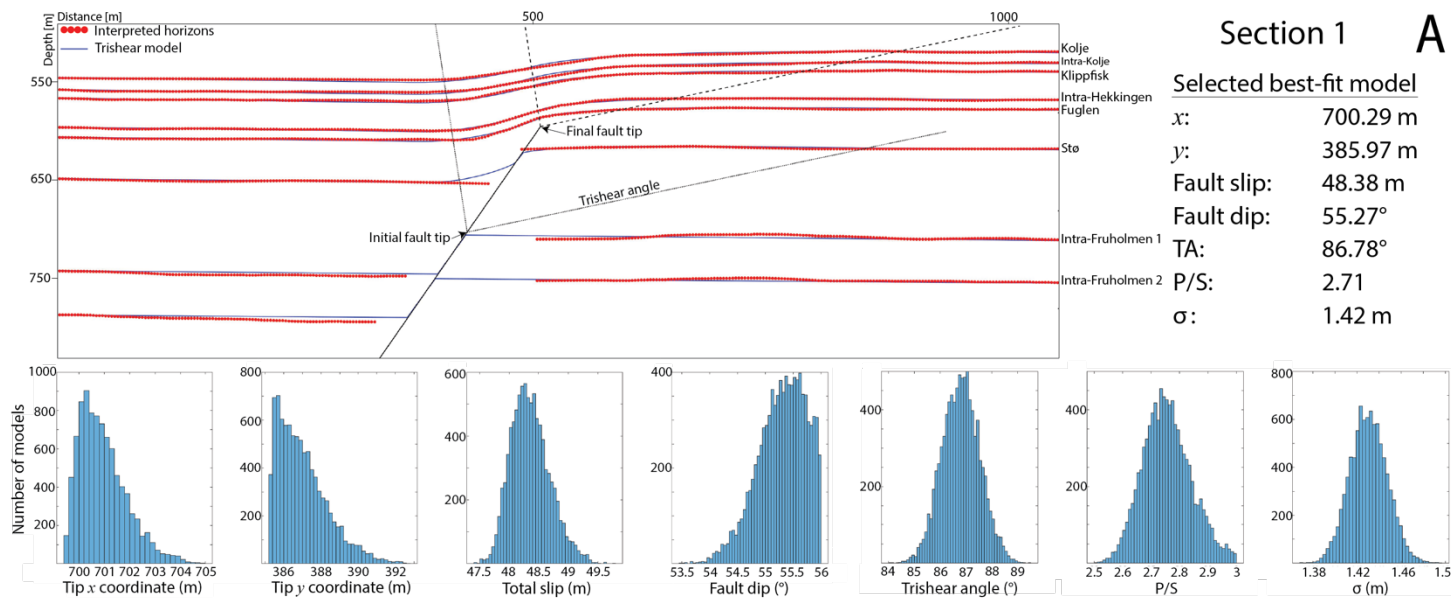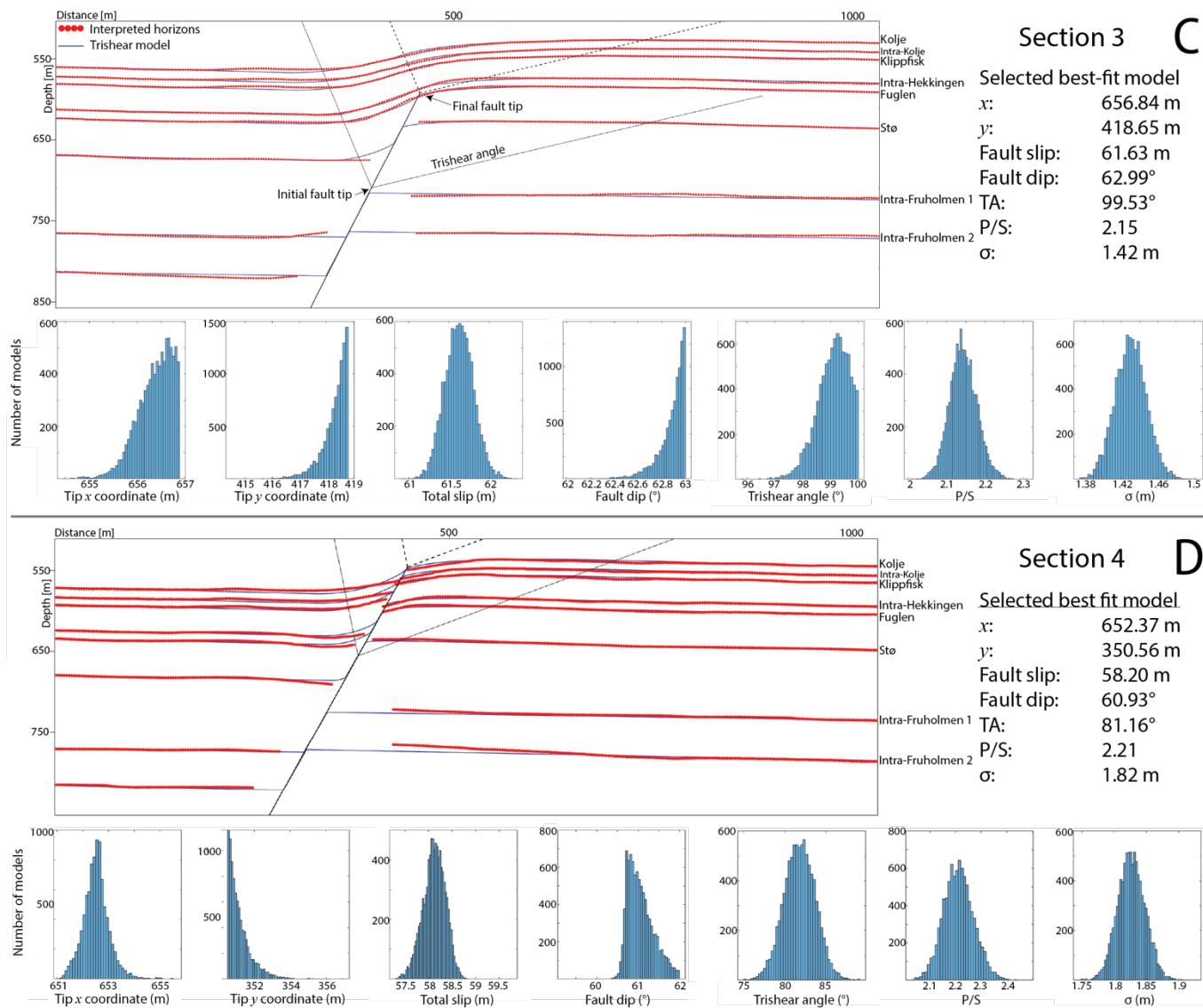
Figure 31: *Trishear modeling results for sections 1 to 4. For each section, the interpretation (red), best-fit model (blue), and parameters histograms are included.*

	Best-fit model parameters						
	x (m)	*y* (m)	Fault slip (m)	Fault dip (°)	TA (°)	P/S	σ (m)
1	700.29	385.97	48.38	55.27	86.78	2.71	1.42
2	676.49	323.45	53.27	56.00	73.75	2.99	2.16
3	656.84	418.65	61.63	62.99	99.53	2.15	1.42
4	652.37	350.56	58.20	60.93	81.16	2.21	1.82

The best trishear model for section 3, fits the section well (Figure 31C). However, it still shows too much folding of the top Stø in the hanging wall. Another deviation is observed in the uppermost three horizons, west of the monocline, which in the section display a broad, low amplitude anticline. Also, gentle synclinal folding of the intra-Fruholmen 1 and 2 horizons in the hanging wall is not reproduced by the model. The histograms for fault tip *y*-location and fault dip are narrow and located at the maximum specified value in the parameter range (Figure 31C). The initial location of the fault tip is right above the intra-Fruholmen 1 footwall cutoff, and the current fault tip is at the top Fuglen horizon. The best-fit model has fault slip ~62 m, fault dip ~63°, TA ~100°, and P/S ~2.15. The σ is ~1.4 m.

In section 4, the best-fit model produces more hanging wall folding of the 5 upper horizons than what is observed in the section (Figure 31D). A deviation between the interpretation and the model is also observed in the footwall for the 2 lowermost horizons intra-Fruholmen 1 and 2. The histogram for fault tip *y*-location has a peak at the lowest specified limit. The initial location of the fault tip is below the top Stø, approximately at 650 m depth. This is the location of the top Fruholmen footwall cutoff, which is not included in the section. The final fault tip is above the top Kolje horizon, which is the uppermost interpreted horizon. The model predicts that the fault breaches all the interpreted horizons in the section. The model has fault slip ~58 m, fault dip ~61°, TA ~81° and P/S ~2.2. The σ is ~1.8 m.

Generally, the best trishear models fit the sections well. There are of course some deviations, for example folding of the top Stø in the hanging wall in all models, which is not observed in the seismic sections. Also, there are misfits in the two lowermost horizons, intra-Fruholmen 1 and 2, in the hanging wall on sections 2 and 3, and in the footwall on section 4. The model for section 2 is the one that exhibits the poorest fit to the monocline, and the model for section 4

shows too much folding of the hanging wall syncline. The sections above were also modelled using the trishear global optimization methods of Cardozo et al. (2011), with similar results.

4.3.2 Strain ellipses

Figure 32 shows the strain ellipses with the lines of no finite elongation (LNFE) superimposed on the best-fit trishear models for each section. The ellipses are colored by the maximum stretch (S_1), and red represents high values. The blue lines inside the ellipses are the LNFE.

In all the sections, a narrower zone of finite strain (strain ellipses) is observed in the hanging wall compared to the footwall. The zone of strain associated to the monocline is the narrowest in section 4. The highest strains are present in the hanging wall close to the fault. The area in front of the fault tip also has large strain. The strain decreases away from the fault. The radius of influence of the strain in the footwall is about 600, 400, 600 and 300 m in sections 1, 2, 3 and 4, respectively (Figure 32).

The LNFE have varying orientation. However, as they approach the fault in the hanging wall and in the monocline forelimb area, there is one set of LNFE that is sub-parallel to the fault, and another set that is sub-horizonal and at low angle to bedding. In the footwall close to the fault and in the monocline backlimb area, the LNFE are gentler than the fault but at high angle to bedding. This reflects the orientation of S_1 (long axis of the ellipses) across the monocline. In the hanging wall, the maximum stretching is along the fault, while in the footwall, the maximum stretching is at low angle to bedding. Thus, the models predict fractures sub-parallel to the fault and at low angle to bedding in the hanging wall (including the forelimb area), and fractures at high angle to bedding but less steep than the fault in the footwall (including the backlimb area).
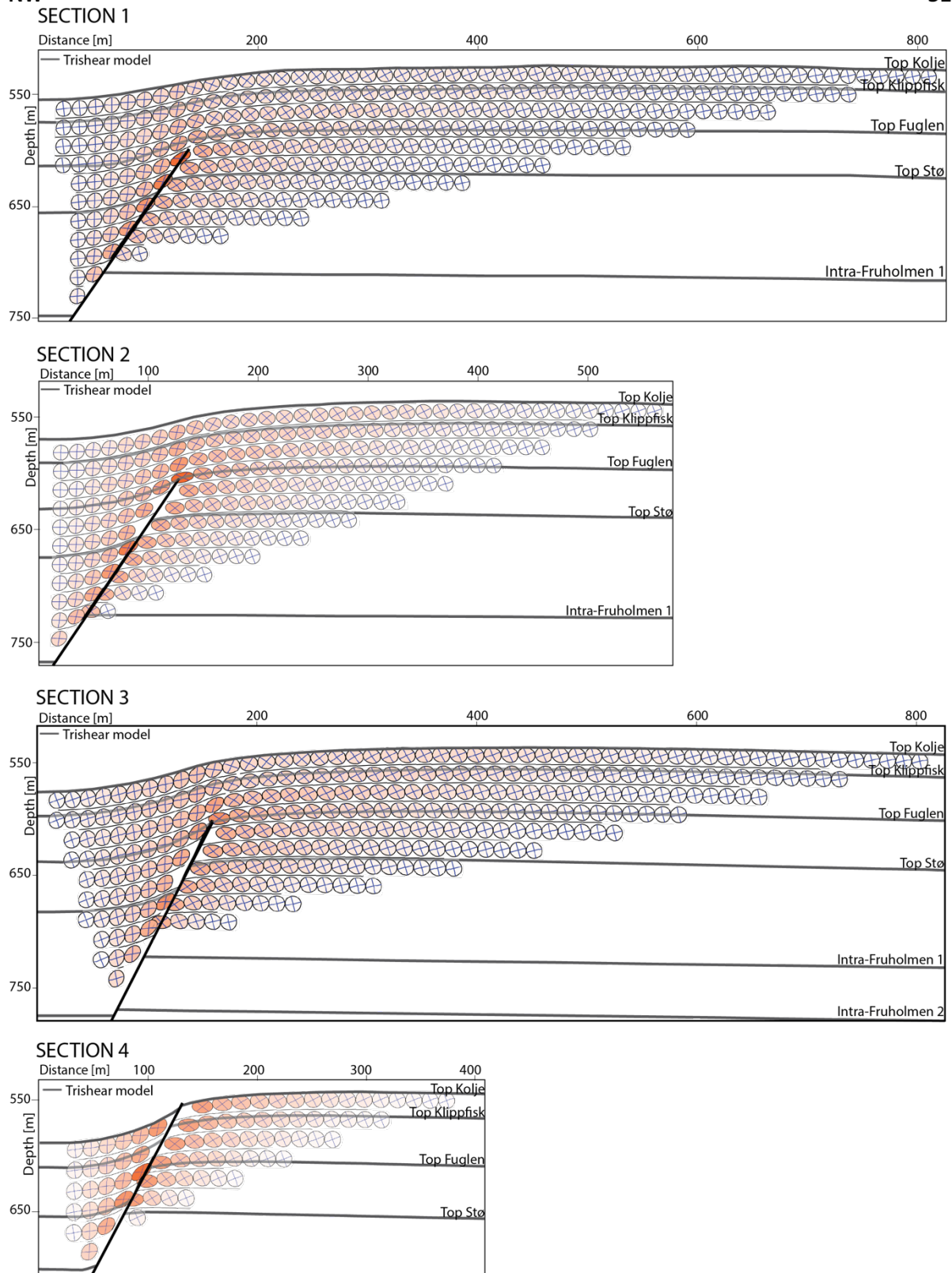
Figure 32: Strain ellipses and LNFE superimposed on the best-fit trishear models for sections 1 to 4. The magnitude of S_1 is indicated by colors and red represents the more strained areas. The blue lines within the ellipses are the LNFE.

5 Discussion

5.1 Geometrical description

The fold is characterized as non-symmetrical, as there is a separation between the fold hinge and fold crest. This separation is larger to the SW, indicating that the fold asymmetry is larger there. The geometry of a folded surface can be described by the two principal curvatures, k_{max} and k_{min}. The Fuglen, Klippfisk and Kolje tops have the highest k_{max} in the anticlinal area, and most negative k_{min} in the synclinal area. All three surfaces display greater curvature values towards the NE, this is also where the largest forelimb dips are observed on the structure maps of the surfaces.

The k_{max} directions are sub-parallel to the synclinal hinge line and sub-perpendicular to the anticlinal hinge line, while the k_{min} directions are the other way around. Based on these observations, it appears that the anticlinal and synclinal hinges approach the idealized cylindrical geometry. However, the k_{max} and k_{min} magnitudes on the surfaces indicate that the fold is not cylindrical as the principal curvatures with orientations parallel to the hinge lines are not equal to zero. In addition, if the monocline were cylindrical, it would have the same geometry in all the seismic sections, which is not the case (Figure 20). Thus, the Fuglen, Klippfisk and Kolje tops depart from the cylindrical shape.

By defining an absolute threshold value (k_t) and filtering out the lowest k_{max} and k_{min} values, one can estimate how far the structure deviates from a cylindrical shape. By applying an increasingly larger threshold value, one can distinguish between areas that slightly depart from the cylindrical geometry, from the more significant non-cylindrical areas. Applying this filter smooths out the surface until the idealized cylindrical shape is attained. Filtering out the absolute curvature values below 5×10^{-4} m^{-1} (2000 m curvature radius) on the top Fuglen surface, produces a geometry that approaches a cylindrical shape, which is represented by an antiform and synform separated by planar areas. By increasing k_t to 9×10^{-4} m^{-1} (1111 m curvature radius), the local non-cylindrical shapes are removed. In addition, this seems to suggest that the monocline is divided into SW, central and NW domains.
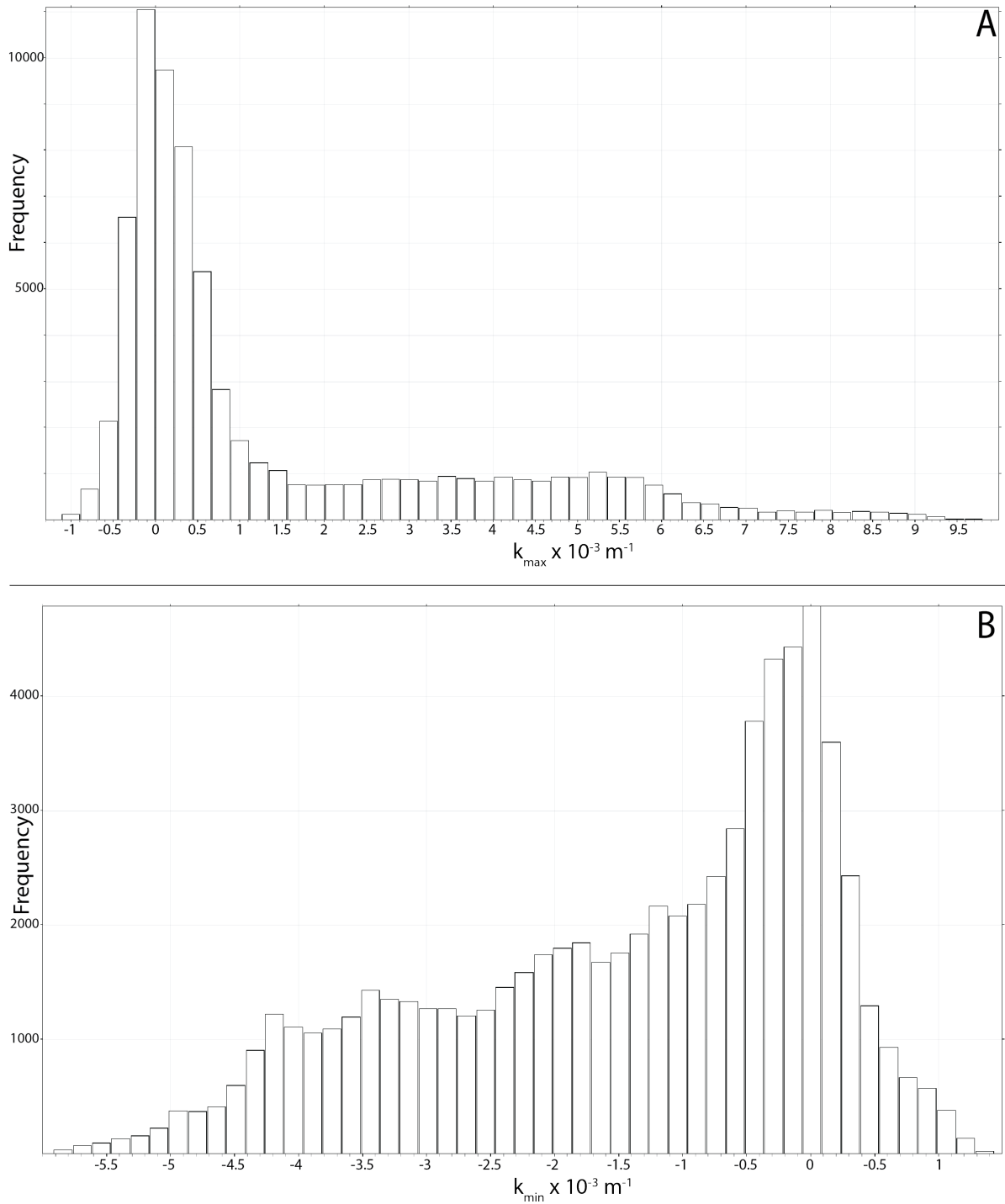
Figure 33: *(A) Histograms of k_{max} and (B) k_{min} on the top Fuglen surface*

Figure 33 displays the k_{max} and k_{min} distributions on the top Fuglen surface. The surface consists originally of ~70,800 points. By applying the first filter with a $k_t = 1 \times 10^{-4}$ m^{-1}, ~10,000 points are removed in the k_{max} distribution, and ~6,200 points are removed from the k_{min} distribution. For $k_t = 5 \times 10^{-4}$ m^{-1}, the number of points removed increases to ~37,900 and ~24,100 points in the k_{max} and k_{min} distributions, respectively. Applying the maximum filter of $k_t = 9 \times 10^{-4}$

m^{-1}, removes ~46 400 (k$_{max}$) and ~33 100 (k$_{min}$) points. This is perhaps removing too much of the actual detail of the surface.

The lowest absolute principal curvature value of the top Fuglen surface is 1.1 x 10^{-8} m^{-1} (90,909,091 m curvature radius). The surface approaches a cylindrical geometry by applying the filter of k$_t$ = 5 x 10^{-4} m^{-1}, as discussed above. Thus, the top Fuglen surface consists of areas with approximately four orders of magnitude in principal curvature (from 1.1 x 10^{-8} m^{-1} to 5 x 10^{-4} m^{-1}) that deviates from the idealized cylindrical surface geometry. Smoothing was applied to the modelled surface prior to the curvature calculations to remove noise. If less smoothing was applied to the surface, the lowest absolute curvature value would have been less than the value reported here. However, the threshold value at which the top Fuglen surface approaches a cylindrical geometry would have been unchanged.

5.2   Kinematic modelling

The trishear kinematic model matches well the interpreted horizons (Figure 31). Section 4, however, produces more hanging wall folding than observed on the seismic image. A possibility is that the symmetric trishear model used here is not appropriate for this section. An asymmetric trishear model with less deformation in the hanging wall (Zehnder & Allmendinger, 2000) may replicate better this section. On the other hand, the smaller deviations observed in the modelled sections could be related to secondary processes that could not be explained by the trishear model. Although, P/S and TA are assumed constant during fault propagation and fold growth, they may have not been constant during the actual evolution of the structure.

It is important to note that the kinematic model is based on seismic interpretations, and errors in the interpretations or artefacts in the seismic image are possible. For example, the interpretation close to the fault plane can be challenged because of a distorted seismic image and fault shadows (footwall sags). This could be an explanation for the misfit between the model and interpretations in the lower three horizons, where the interpretations dip towards or away from the fault plane in sections 2, 3 and 4, but in the models, they are flat (Figure 31B, C & D).

The sigma (σ) parameter represents the uncertainty of the data which is not known ahead of time. The lowest uncertainty, 1.42 m, is found in sections 1 and 3 (Figure 31A & C), which display the best match between the model and the interpretations. Sections 2 (σ = 2.16 m) and section 4 (σ = 1.82 m) show higher misfits (Figure 31B & D). The interpretation was completed

on depth sampled seismic. Of course, there is an unknown uncertainty in the depth conversion from the time domain. In the way these models were done, this depth conversion uncertainty is not included in the σ parameter. However, this uncertainty should be included in the value of σ and incorporated in the search (Cardozo and Oakley, 2019). Finally, some of the parameter histograms show the highest frequencies close to the minimum or maximum defined range boundaries. However, the parameter ranges were not increased because of this, as the parameters were well constrained based on the interpretations of the seismic data.

5.3 Evolution of the monocline

5.3.1 Mechanical stratigraphy

The basic lithology description indicates that the Kolmule, Kolje, Hekkingen and Fuglen formations mainly consist of shale. Thin carbonate interbeds or stringers are interpreted in these shaly successions (Figure 19), which is consistent with the lithology descriptions of Worsley et al. (1988). The Klippfisk Formation is interpreted as carbonates based on the well logs response, and this is also confirmed by Dallmann (1999). The carbonate succession in the Klippfisk Formation is less than 10 m in the well 7324/8-3, and it is underlain and overlain by thick shale deposits (Figure 19). The lower two formations, Stø and Fruholmen, consist of sandy successions. The well logs record a homogeneous sandstone package in the Stø Formation, while the Fruholmen Formation consist of interbeds of sand and shale. The shaly upper successions are folded in the monocline, while the stratigraphically lower sandy successions are faulted. The displacement along the fault resulted in folding of the shalier incompetent rocks, while the competent brittle rocks deform by faulting. This suggests that rock mechanical properties and mechanical stratigraphy contribute to the formation of the monocline.

Several authors have discussed if the P/S parameter could be related to rock mechanical properties and mechanical stratigraphy. Allmendinger et al. (2004) suggest that out of the six trishear parameters, the P/S is the most important in defining the fold geometry. Hardy and Allmendinger (2011) and Cardozo et al. (2011) indicate that although trishear is a kinematic model, the P/S could be related to the mechanical properties of the rock across which the fault propagates.

The P/S value in section 1 and 2 (2.71 and 2.99, respectively) is higher than in sections 3 and 4 (2.15 and 2.21, respectively) (Figure 31 and Table 2). This indicates that the fault propagated more than it slipped in the southern sections 1 and 2 compared to the northern sections 3 and 4.

With lower P/S, the rate of fault propagation is lower, meaning that the successions will stay longer within the trishear zone, and possibly deform more. Section 3 has the lowest P/S, and this is also the section where the folding of the monocline is best defined. Section 4 has the second lowest P/S value. However, the initial fault tip in this section is the shallowest (~ 10 m below top Stø in the footwall) and the fault breaches the monocline. The trishear model for section 4 also predicts more folding in the hanging wall than what is observed in the seismic image. Therefore, the P/S for this section could be higher.

The trishear angle (TA) is the parameter that varies most. This is not surprising, since the significance of the TA parameter is elusive as discussed by Allmendinger et al. (2004) & Hardy and Allmendinger (2011). The variation in TA could imply that this parameter is less related to the rock mechanical properties. This is also suggested by Cardozo et al. (2011).

In summary, from SW to NE, the P/S varies from 2.7 to 2.2, the fault slip from 50 to 60 m, the fault propagation is ~130-140 m, the initial fault tip is ~50 m below the footwall top Stø cutoff in sections 1-3 (at the footwall intra-Fruholmen 1 horizon), but in section 4 it is just ~10m below the same top and the fault breaches the monocline.

5.3.2   Faulting

The monocline was formed by displacement and propagation of fault 1 (Figure 20). The maximum throw of faults 1 and 2 is displayed on Figure 34. Clearly, there is a transfer of displacement between the two faults in the relay structure, which is shown on the structure map of the top Stø Formation (Figure 21D). However, the displacements of faults 1 and 2 in the relay don't add up to the maximum displacement of either fault 1 or 2, to the NE or SW, respectively. This suggests that faults 1 and 2, besides propagating upwards, propagated laterally towards the relay. This explains why the monocline is more developed and breached to the north, and less developed in the relay zone (Figure 20). The trishear model also predicts a 7-8º variation in fault dip, with the highest fault dip towards the NE.
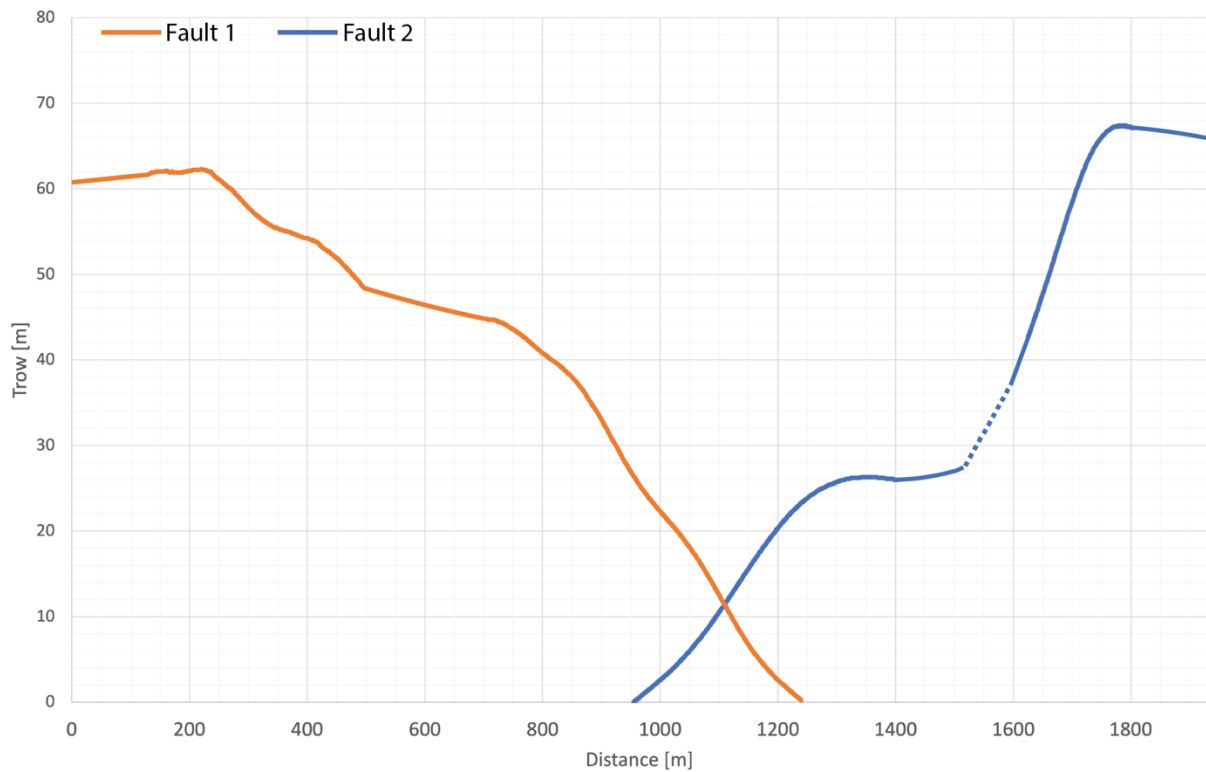
Figure 34: *Throw of faults 1 and 2 based on the cutoffs in Figure 23A. The stippled line on fault 2 represents the area affected by fault 3.*

Thickness variations can suggest when the faults were active in the area. The interpreted units do not display large thickness variations, indicating that they were deposited before faulting (Figure 20). However, as mentioned before, a thickness increase in the Hekkingen Formation is observed in the hanging wall of fault 3. This is most prominent in Figure 20I, and on the thickness map of the Hekkingen Formation (Figure 35A). The increase in thickness of the Hekkingen Formation in the hanging wall of fault 3, particularly towards the west (Figure 35A), could indicate that fault 3 was active during the deposition of this unit, in the late Oxfordian – Volgian. However, these are minor thickness variations in comparison to the most significant variations observed in the Kolmule Formation (Figure 35B), which was deposited in the Aptian – middle Cenomanian. Faults 1, 2 and 3 terminate in this formation. Therefore, the Kolmule Formation is a syntectonic unit, and faults 1-3 were formed in the Aptian-early Albian. This is consistent with Faleide et al. (2019).
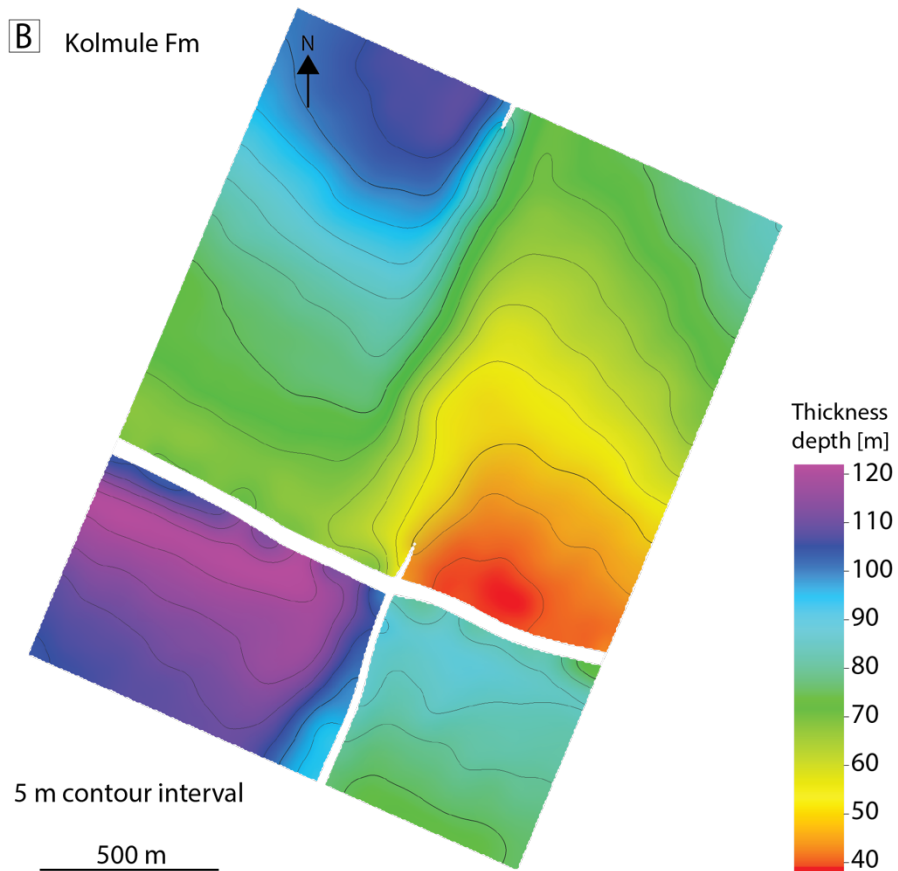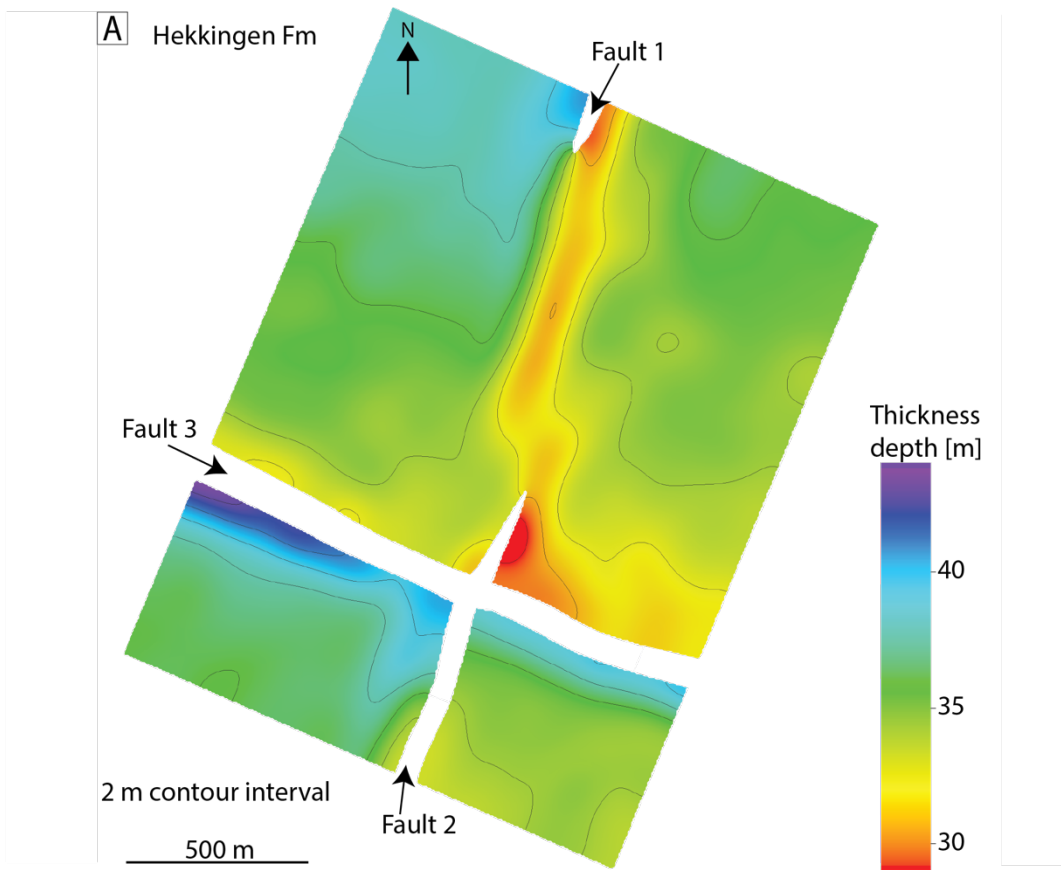
Figure 35: *Thickness map of (A) the Hekkingen Formation and (B) the Kolmule Formation. Fault polygons in B are from the horizon immediately below, top Kolje (Figure 21A).*

5.4 Fluid flow

The monocline is located at the crest of a ~20 km wide structure, which has a maximum relief of ~200 m (Figure 6). The structure contains hydrocarbons, and it is interesting with respect to fluid migration, particularly during the future development of the field. The relay ramp structure could play an important role for the upward migration of fluids, as these structures can be lateral and vertical pathways for fluid flow (Fossen & Rotevatn, 2016). However, the upper shaly successions in the monocline act as top seals and could prevent the fluids to migrate further upwards.

Most faults that offset the folded Upper Jurassic and Lower Cretaceous sediments terminate below the URU, which separates the fine-grained Kolmule Formation from the overlying Quaternary glacial deposits. However, on the seismic sections in Figure 20, the URU reflector is quite chaotic. It is not clear if some of the polygonal faults in the Kolmule succession offset the URU. Additionally, on the seismic section in Figure 20H, fault 3 terminates very close to the URU, but it is difficult to determine if the fault breaches the unconformity. If there is fluid flow along fault 3, and the fault offsets the URU, there is risk for fluids leaking up to the surface. However, the top Stø-top Kolmule sequence is quite shaly, and most probably there is a thick shale smear along fault 3 that prevents fluid flow. It is also important to consider possible migration pathways in the shallow polygonal faults. As the reservoirs are located at very shallow depth, there are no buffer zones to trap the fluids if they leak through the top seal via the polygonal faults.

For the monocline in the top Stø-top Kolje succession, the largest strain magnitudes based on the trishear models are in the hanging wall, close to the fault, and in front of the fault in the forelimb area (Figure 32). In these areas, there can be fractures sub-parallel to the fault that, if they are open, can easily link to the fault and connect fluids to the surface (Figure 36). In the footwall and backlimb area, the strain is lower, and the predicted fractures have lower angle than the fault and may not be as effective in conducting fluids to the surface. However, areas of higher strain are not necessarily fractured, but could also accommodate the strain by other mechanisms than fracturing. This depends on the mechanical properties of the rocks (mainly shales) and their history of deformation.

Makurat et al. (1992) concluded that there is an increased risk of fluids leaking through the top seal in areas where Cenozoic uplift exceeds 1.6 – 1.7 km. However, Hansen et al. (2020) describe gas accumulations in areas which have experienced ~2.0 km uplift. They propose that

shales which have experienced large uplift could still maintain their sealing capacities (i.e. they are not fractured) depending on their brittleness. The brittleness depends on several factors (e.g maximum burial depth, extent of cementation and consolidation), and not the uplift itself (Hansen et al., 2020). Thus, uplifted poorly consolidated shales are more likely to have a ductile behavior. Contrarily, uplifted well consolidated and cemented shales with similar composition are more prone to brittle fracturing. However, recent studies in the Barents Sea suggest that the greater risk of fluids leaking out of structural traps is related to reactivation of faults (Edmundson et al., 2020) and/or fault intersections at the top reservoir level (Hermanrud et al., 2014), than the integrity of the top seal. Additionally, in the study area, the Upper Jurassic to Lower Cretaceous sequence (top Stø to URU) is quite shaly (Figure 19) and therefore, the top seal is strong. The seismic data does not show any seismic anomalies indicating leakage through the faults or the top seal. Nonetheless, it is important to recognize that there is a higher risk for fractured areas in the forelimb of the monocline. Optimally, one should verify these hypotheses using actual fracture indicators from well or seismic data.
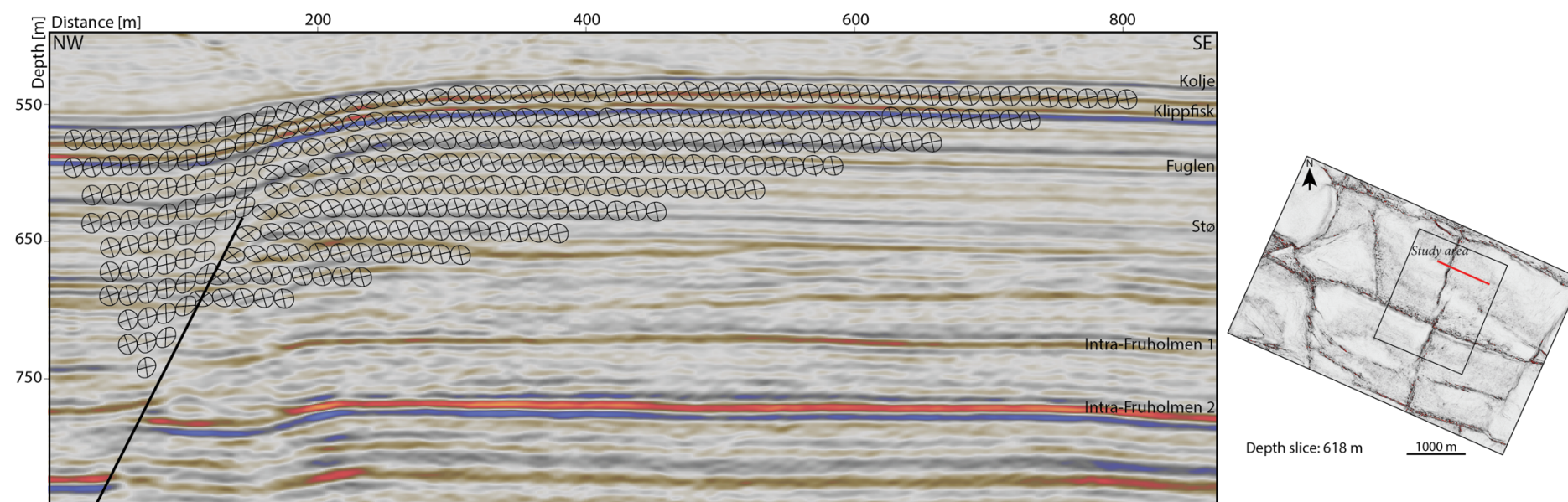

Figure 36: Zoom in of section 3 displaying the strain ellipses and LNFE from the best-fit trishear model. VE = 1.0.

6 Conclusions

- A monocline in the Wisting field, Norwegian Barents Sea, was analyzed. This fold is developed in shaly Upper Jurassic–Lower Cretaceous sediments (Fuglen to Kolje formations) which are close (~150-200 m) to the seabed.

- The fold is characterized as asymmetrical and non-cylindrical based on the principal curvatures. However, by filtering out the curvatures below a threshold value of 5×10^{-4} m^{-1} (2000 m curvature radius), the fold can be classified as approximately cylindrical.

- The monocline is underlain by a NNE-SSW normal fault (fault 1) that towards the south links to another fault (fault 2) on a relay structure. From the relay structure, the fault displacement increases towards the NE on fault 1, and towards the SW on fault 2.

- The monocline is continuous in sections 1 (SW) to 3 and is breached by the fault in the northernmost section 4.

- The trishear model fits the geometry of the monocline. It predicts a fault nucleation depth in the Upper Triassic intra-Fruholmen succession in sections 1-3, and a shallower nucleation depth close to the top Fruholmen Formation in section 4. The model suggests that the P/S decreases from the south (P/S = ~2.8) to the north (P/S = ~2.2).

- The fold was developed as result of displacement and propagation of the underlying fault, which was controlled by the mechanical stratigraphy. The fault offset the lower brittle sandstone successions, while it folded the upper shaly ductile successions.

- The fault was mainly active during the Early Cretaceous (Aptian–Albian), during the deposition of the Kolmule Formation.

- The strain predicted by the trishear models is maximum in the hanging wall areas close to the fault and in the forelimb of the monocline. There, two fracture sets are predicted, one sub-parallel to the fault and the other to bedding.

- Although the top seal is strong and high strain in the monocline can be accommodated by mechanisms other than fracturing, it is important to recognize the risk fractures may present for fluids escaping to the surface through the monocline.

7   References

Allmendinger, R. W. (1998). Inverse and forward numerical modeling of trishear fault-propagation folds. *Tectonics, 17*(4), 640-656. doi:https://doi.org/10.1029/98TC01907

Allmendinger, R. W., Zapata, T., Manceda, R., & Dzelalija, F. (2004). Trishear Kinematic Modeling of Structures, with Examples from the Neuquén Basin, Argentina. In K. R. McClay (Ed.), *Thrust tectonics and hydrocarbon systems* (Vol. 82, pp. 356-371): AAPG Memoir.

Andersen, M. A. (2016). The Defining Series: Basic Well Log Interpretation. *Schlumberger Oilfield Review*. Retrieved from https://www.slb.com/resource-library/oilfield-review/defining-series/defining-log-interpretation. (Read May 20th 2021)

Bellwald, B., Planke, S., Lebedeva-Ivanova, N., Piasecka, E. D., & Andreassen, K. (2019). High-resolution landform assemblage along a buried glacio-erosive surface in the SW Barents Sea revealed by P-Cable 3D seismic data. *Geomorphology (Amsterdam, Netherlands), 332*, 33-50. doi:10.1016/j.geomorph.2019.01.019

Bergbauer, S. (2007). Testing the predictive capability of curvature analyses. *Geological Society, London, Special Publications, 292*(1), 185-202. doi:10.1144/sp292.11

Bergbauer, S., & Pollard, D. D. (2003). How to calculate normal curvatures of sampled geological surfaces. *Journal of Structural Geology, 25*(2), 277-289. doi:10.1016/S0191-8141(02)00019-6

Cardozo, N., & Allmendinger, R. W. (2013). Spherical projections with OSXStereonet. *Computers & geosciences, 51*, 193-205. doi:10.1016/j.cageo.2012.07.021

Cardozo, N., Jackson, C. A.-L., & Whipp, P. S. (2011). Determining the uniqueness of best-fit trishear models. *Journal of Structural Geology, 33*(6), 1063-1078.

Cardozo, N., & Oakley, D. (2019). Inverse modeling for possible rather than unique solutions. *Journal of Structural Geology, 125*, 285-295. doi:10.1016/j.jsg.2018.05.026

Cardozo, N., & Aanonsen, S. (2009). Optimized trishear inverse modeling. *Journal of Structural Geology, 31*(6), 546-560. doi:10.1016/j.jsg.2009.03.003

Coleman, A. J., Duffy, O. B., & Jackson, C. A.-L. (2019). Growth folds above propagating normal faults. *Earth-Science Reviews, 196*, 102885.

Collanega, L., Massironi, M., Breda, A., & Kjølhamar, B. E. (2017). Onset of N-Atlantic rifting in the Hoop Fault Complex (SW Barents Sea): An orthorhombic dominated faulting? *Tectonophysics, 706-707*, 59-70. doi:10.1016/j.tecto.2017.04.003

Dallmann, W. K., (ed.). (1999). *Lithostratigraphic lexicon of Svalbard: review and recommendations for nomenclature use : Upper Palaeozoic to Quaternary bedrock.* Tromsø: Norsk polarinstitutt.

Doré, A. G. (1995). Barents Sea geology, petroleum resources and commercial potential. *Arctic, 48*, 207-221.

Edmundson, I., Rotevatn, A., Davies, R., Yielding, G., & Broberg, K. (2020). Key controls on hydrocarbon retention and leakage from structural traps in the Hammerfest Basin, SW Barents Sea: implications for prospect analysis and risk assessment. *Petroleum Geoscience, 26*(4), 589-606. doi:10.1144/petgeo2019-094

Erslev, E. A. (1991). Trishear fault-propagation folding. *Geology, 19*(6), 617-620. doi:10.1130/0091-7613(1991)019<0617:Tfpf>2.3.Co;2

Faleide, J. I., Vågnes, E., & Gudlaugsson, S. T. (1993). Late Mesozoic–Cenozoic evolution of the southwestern Barents Sea. *Geological Society, London, Petroleum Geology Conference series, 4*(1), 933-950. doi:10.1144/0040933

Faleide, T. S., Midtkandal, I., Planke, S., Corseri, R., Faleide, J. I., Serck, C. S., & Nystuen, J. P. (2019). Characterisation and development of Early Cretaceous shelf platform deposition and faulting in the Hoop area, southwestern Barents Sea-constrained by high-resolution seismic data. *Norwegian Journal of Geology, 99*.

Ferrill, D. A., Morris, A. P., & McGinnis, R. N. (2012). Extensional fault-propagation folding in mechanically layered rocks: The case against the frictional drag mechanism. *Tectonophysics, 576-577*, 78-85. doi:10.1016/j.tecto.2012.05.023

Fossen, H., & Rotevatn, A. (2016). Fault linkage and relay structures in extensional settings – A review. *Earth-Science Reviews, 154*, 14-28. doi:https://doi.org/10.1016/j.earscirev.2015.11.014

Gabrielsen, R. H., Færseth, R. B., Jensen, L. N., Kalheim, J. E., & Riis, F. (1990). Structural Elements of the Norwegian Continental Shelf Part 1: The Barents Sea Region. *Norwegian Petroleum Directorate Bulletin, 6*.

Glørstad-Clark, E., Faleide, J. I., Lundschien, B. A., & Nystuen, J. P. (2010). Triassic seismic sequence stratigraphy and paleogeography of the western Barents Sea area. *Marine and Petroleum geology, 27*(7), 1448-1475. doi:10.1016/j.marpetgeo.2010.02.008

Granli, J. R., Veire, H. H., Gabrielsen, P., & Morten, J. P. (2017). *Maturing broadband 3D CSEM for improved reservoir property prediction in the Realgrunnen Group at Wisting, Barents Sea.* Paper presented at the 2017 SEG International Exposition and Annual Meeting.

Gudlaugsson, S., Faleide, J., Johansen, S., & Breivik, A. (1998). Late Palaeozoic structural development of the south-western Barents Sea. *Marine and Petroleum geology, 15*(1), 73-102.

Hansen, J. A., Mondol, N. H., Tsikalas, F., & Faleide, J. I. (2020). Caprock characterization of Upper Jurassic organic-rich shales using acoustic properties, Norwegian Continental Shelf. *Marine and Petroleum geology, 121*, 104603. doi:10.1016/j.marpetgeo.2020.104603

Hardwick, A., & Rajesh, L. (2013). A 3D illumination study to investigate fault shadow effects over the Hoop Fault Complex. In *SEG Technical Program Expanded Abstracts 2013* (pp. 3315-3319).

Hardy, S., & Allmendinger, R. W. (2011). Trishear: A review of kinematics, mechanics, and applications. In K. McClay, J. Shaw, & J. Suppe (Eds.), *Thrust Fault-Related Folding* (Vol. 94, pp. 95-119). AAPG Memoir.

Henriksen, E., Bjørnseth, H. M., Hals, T. K., Heide, T., Kiryukhina, T., Kløvjan, O. S., . . . Stoupakova, A. (2011a). Chapter 17 Uplift and erosion of the greater Barents Sea: impact on prospectivity and petroleum systems. *Geological Society, London, Memoirs, 35*(1), 271-281. doi:10.1144/m35.17

Henriksen, E., Ryseth, A. E., Larssen, G. B., Heide, T., Rønning, K., Sollid, K., & Stoupakova, A. V. (2011b). Chapter 10 Tectonostratigraphy of the greater Barents Sea: implications for petroleum systems. *Geological Society, London, Memoirs, 35*(1), 163-195. doi:10.1144/m35.10

Hermanrud, C., Halkjelsvik, M. E., Kristiansen, K., Bernal, A., & Strömbäck, A. C. (2014). Petroleum column-height controls in the western Hammerfest Basin, Barents Sea. *Petroleum Geoscience, 20*(3), 227-240. doi:10.1144/petgeo2013-041

Kjølhamar, B. (2015). The Hoop Area: New Testing Ground for Geophysical Technologies. *GEO ExPro, 12(3)*.

Klausen, T. G., Müller, R., Poyatos-Moré, M., Olaussen, S., & Stueland, E. (2019). Tectonic, provenance and sedimentological controls on reservoir characteristics in the Upper Triassic–Middle Jurassic Realgrunnen Subgroup, SW Barents Sea. *Geological Society, London, Special Publications, 495*, SP495-2018-2165. doi:10.1144/sp495-2018-165

Larionov, V. V. (1969). *Borehole Radiometry* Moscow: Nedra.

Lasabuda, A. P. E., Johansen, N. S., Laberg, J. S., Faleide, J. I., Senger, K., Rydningen, T. A., . . . Hanssen, A. (2021). Cenozoic uplift and erosion of the Norwegian Barents Shelf – A review. *Earth-Science Reviews, 217*, 103609. doi:10.1016/j.earscirev.2021.103609

Lewis, M. M., Jackson, C. A. L., Gawthorpe, R. L., & Whipp, P. S. (2015). Early synrift reservoir development on the flanks of extensional forced folds; a seismic-scale outcrop analog from the Hadahid fault system, Suez Rift, Egypt. *AAPG bulletin, 99*(6), 985-1012. doi:10.1306/12011414036

Makurat, A., Torudbakken, B., Monsen, K., & Rawlings, C. (1992). *Cenezoic Uplift and Caprock Seal in the Barents Sea: Fracture Modelling and Seal Risk Evaluation.* Paper presented at the SPE Annual Technical Conference and Exhibition, Washington, DC.

Marshak, S., & Mitra, G. (1988). *Basic Methods of Structural Geology*: Prentice Hall, Englewood Cliffs, NJ.

Mondol, N. H. (2015). Well Logging: Principles, Applications and Uncertainties. In K. Bjørlykke (Ed.), *Petroleum Geoscience: From Sedimentary Environments to Rock Physics* (pp. 385-425). Berlin, Heidelberg: Springer Berlin Heidelberg.

Moskvil, L. M., Veire, H. H., Stueland, E., Granli, J. R., Krathus-Larsen, K., Michot, O., . . . Dyrendahl, M. (2018). *High resolution seismic interpretation at Wisting: A breakthrough for shallow reservoir development*. Paper presented at the NPF biennial geophysical seminar, Oslo.

Mynatt, I., Bergbauer, S., & Pollard, D. D. (2007). Using differential geometry to describe 3-D folds. *Journal of Structural Geology, 29*(7), 1256-1266. doi:10.1016/j.jsg.2007.02.006

Norwegian Polar Institute. (2020). Barentsportal (www.barentsportal.com) (WMS). Retrieved from https://geodata.npolar.no/arcgis/rest/services/Barentsportal. (10.8). Retrieved 29. March 2021, from Norwegian Polar Institute, https://geodata.npolar.no/arcgis/rest/services/Barentsportal

NPD. (2018). FactPages Well 7324/7-3 S. *Norwegian Petroleum Directorate FactPages.* Retrieved from https://factpages.npd.no/en/wellbore/PageView/Exploration/All/7875. (Read March 9th 2021)

NPD. (2019). FactPages Well 7324/8-3. *Norwegian Petroleum Directorate FactPages.* Retrieved from https://factpages.npd.no/en/wellbore/PageView/Exploration/All/8239. (Read March 9th 2021)

NPD. (2021). NPD Factmaps (Factmaps). Retrieved from https://factmaps.npd.no/factmaps/3_0/. Retrieved April 11th 2021, from Norwegian Petroleum Directorate https://factmaps.npd.no/factmaps/3_0/

Nøttvedt, A., Cecchi, M., Gjelberg, J., Kristensen, S., Lønøy, A., Rasmussen, A., . . . Van Veen, P. (1993). Svalbard-Barents Sea correlation: a short review. *Norwegian Petroleum Society Special Publications, 2*, 363-375.

Oakley, D. O. S., & Fisher, D. M. (2015). Inverse trishear modeling of bedding dip data using Markov chain Monte Carlo methods. *Journal of Structural Geology, 80*, 157-172. doi:10.1016/j.jsg.2015.09.005

Paulsen, R., Grundvåg, S., Senger, K., & Stueland, E. (2019). Seal Integrity in the Uplifted Basins in the Greater Hoop Area on the Northern Barents Shelf. *2019*(1), 1-5. doi:https://doi.org/10.3997/2214-4609.201902355

Petroleum Experts. (2020a). MOVE Tutorial 10: Model Conditioning [Software Tutorial]. MOVE Software: Petroleum Experts,. Accessed March 23rd 2021

Petroleum Experts. (2020b). Surface Geometry Analysis: Curvature Analysis (Version 2020). MOVE 2020 Knowledge Base: Petroleum Experts. Accessed April 30th 2021

Petrov, O. V., Sobolev, N. N., Koren, T. N., Vasiliev, V. E., Petrov, E. O., Larssen, G. B., & Smelror, M. (2008). Palaeozoic and early Mesozoic evolution of the East Barents and Kara seas sedimentary basins. *Norsk Geologisk Tidsskrift, 88*(4), 227-234.

Riis, F. (1996). Quantification of Cenozoic vertical movements of Scandinavia by correlation of morphological surfaces with offshore data. *Global and planetary change, 12*(1), 331-357. doi:10.1016/0921-8181(95)00027-5

Riis, F., & Fjeldskaar, W. (1992). On the magnitude of the Late Tertiary and Quaternary erosion and its significance for the uplift of Scandinavia and the Barents Sea. In *Structural and Tectonic Modelling and its Application to Petroleum Geology* (pp. 163-185): Elsevier.

Roberts, A. (2001). Curvature attributes and their application to 3D interpreted horizons. *First Break, 19*(2), 85-100. doi:https://doi.org/10.1046/j.0263-5046.2001.00142.x

Rojo, L. A., Cardozo, N., Escalona, A., & Koyi, H. (2019). Structural style and evolution of the Nordkapp Basin, Norwegian Barents Sea. *AAPG bulletin, 103*(9), 2177-2217. doi:10.1306/01301918028

Schlumberger. (2015). Recommended Seismic Volume Attributes Petrel 2015 (Poster). Retrieved from www.software.slb.com/-/media/software-media-items/software/documents/external/product-sheets/petrel_recommended_seismic_volume_attributes_2015_poster.pdf. (Read March 23rd 2021)

Schlumberger. (2020). Petrel 2020 Guru - Seismic Well Tie Studies - Depth Seismic Calibration [Help Pages]. Petrel 2020 Guru: Schlumberger. Accessed March 23rd 2021

Smelror, M., Mørk, A., Monteil, E., Rutledge, D., & Leereveld, H. (1998). The Klippfist Formation—a new lithostratigraphic unit of Lower Cretaceous platform carbonates on the Western Barents Shelf. *Polar Research, 17*(2), 181-202.

Smelror, M., Petrov, O., Larssen, G. B., & Werner, S. (2009). Atlas. Geological history of the Barents Sea. *Norges Geol. undersøkelse*, 1-135.

Stueland, E. (2016). *Wisting - shallow reservoir. Possibilities and challenges*. Paper presented at the FORCE Underexplored Plays II, Stavanger.

Suppe, J. (1985). *Principles of structural geology*. Englewood Cliffs, New Jersey: Prentice-Hall.

Worsley, D. (2008). The post-Caledonian development of Svalbard and the western Barents Sea. *Polar Research, 27*(3), 298-317. doi:10.3402/polar.v27i3.6197

Worsley, D., Johansen, R., & Kristensen, S. E. (1988). The Mesozoic and Cenozoic succession of Tromsøflaket. In A. Dalland, D. Worsley, & K. Ofstad (Eds.), *A lithostratigraphic scheme for the Mesozoic and Cenozoic succession offshore mid-and northern Norway. Norwegian Petroleum Directorate Bulletin* (Vol. 4, pp. 42-65). NPD Bulletin No 4: Oljedirektoratet.

Zehnder, A. T., & Allmendinger, R. W. (2000). Velocity field for the trishear model. *Journal of Structural Geology, 22*(8), 1009-1014. doi:10.1016/S0191-8141(00)00037-7